12-2017

Experimental Demonstration of Engineered Dipole-Dipole Interactions in Nanophotonic Environments

Ward D. Newman
Purdue University

EXPERIMENTAL DEMONSTRATION OF ENGINEERED DIPOLE-DIPOLE INTERACTIONS IN NANOPHOTONIC ENVIRONMENTS

A Dissertation

Submitted to the Faculty

of

Purdue University

by

Ward D. Newman

In Partial Fulfillment of the

Requirements for the Degree

of

Doctor of Philosophy

December 2017

Purdue University

West Lafayette, Indiana

THE PURDUE UNIVERSITY GRADUATE SCHOOL
STATEMENT OF DISSERTATION APPROVAL

Dr. Zubin Jacob

School of Electrical and Computer Engineering at Purdue University

Dr. Andrew Weiner

School of Electrical and Computer Engineering at Purdue University

Dr. Minghao Qi

School of Electrical and Computer Engineering at Purdue University

Dr. Robert Fedosejevs

Department of Electrical and Computer Engineering at University of Alberta

Approved by:

Dr. Venkataramanan Balakrishnan

Head of Electrical and Computer Engineering

To my wife Jenna, thank you for all your love and support; to my parents Bill and Jane, thank you for encouraging my curiosity in science and engineering; to my Grandparents William and Florence Newman, and Doug and Coleen Wilson, thank you for showing me that hard work, sacrifice and intelligence are what make you successful and that these things are typically all that are in your control.

ACKNOWLEDGMENTS

I acknowledge the support and brilliance of Zubin Jacob. This extraordinary man took me into his tutelage in 2010, the first day of his professorship at the University of Alberta. In those early years of my studies and his professorship, I benefited from his desire to uncover the unknown and his unwavering drive and interest in all things science and interesting; I was shielded from the time wasting academic politics and focused solely on science. Together we founded a first class experimental quantum nanophotonics laboratory and my career is indebted to Zubin's guidance and unwavering trust in my skills as an experimentalist.

I would also like to acknowledge the invaluable contributions that my colleague and dear friend Cristian Cortes has had on my career as a scientist. His approach as a theorist and mine as an experimentalist often clashed, each of us thinking the answer was obvious – my understanding of the natural world is much deeper and more solid from these often after hours and off the record quantum optics discussions.

I am sincerely grateful to the critical guidance and counsel of Prof. Robert Fedosejevs. My thoroughness and breadth of skills as an Engineering Physicist is due to (1) Bob opening up his entire ultrafast physics lab to me for metamaterial experimentation and (2) Bob's insistence that I question the certainty and physical origin of every measurement. For it not for Bob, our experiments would never have gotten off the ground and Zubin would not have put his trust in me to build our new quantum nanophotonics lab.

The outstanding nanofabrication technical staff and engineers at both the University of Alberta's nanoFab and Purdue's Birck Nanotechnology center have been first class, the whole way. For helping me perfect all my nanofabrication process flow, I give praise in particular to Les Schowalter (U of A), Keith Franklin (U of A),

Jeffery Kuhn (Purdue), Jerry Shephard (Purdue), David Lubelski (Purdue), Kennth Schwartz (Purdue), and Nithin Raghunathan (Purdue).

There are numerous teachers and professors along the way that have helped me immeasurably. Prof. Carsten Krauss granted me my first foray into formal exploratory science by inviting me to work help with the dark-matter search, the PICASSO project at the Sudbury Neutrino Observatory. Prof. Raymond DeCorby hired me as an undergraduate nanophotonics fabrication engineer and from my contributions, I was listed on a co-author my first publication! This essentially launched my career as a research engineer. Other engineering and science professors that over the years shaped my creative thought are as follows: John Vogt (UNBC Chemistry), Edward Dobrowolski (UNBC Mathematics), Frank Hegmann (U of A Physics), Chris Backhouse (U of A Engineering-Physics), Vien Van (U of A Engineering-Physics), and Michael Brett (U of A Engineering-Physics)

TABLE OF CONTENTS

Page

Page

Page

LIST OF TABLES

LIST OF FIGURES

Figure Page

Figure Page

Figure Page

Figure Page

Figure Page

Figure Page

Figure Page

Figure Page

Figure Page

Figure Page

Figure Page

Figure Page

Figure Page

Figure Page

SYMBOLS

$\vec{k}$	wavevector of electromagnetic plane wave
$\bar{\bar{\epsilon}}$	Dielectric permitivitty tensor
β	linear factor by which excited state lifetime decreases
η	Quantum efficiency
Γ	Radiation rate / Relaxation rate of excited state
k_x	transverse wavevector of plane wave
F_p	Far-field Purcell Factor

ABBREVIATIONS

HMM	Hyperbolic Metamaterial
RDDI	Resonant Dipole Dipole Interactions
ENZ	Epsilon-Near-Zero
FRET	Förster Resonance Energy Transfer
NP	Nanoparticle
LSP	Localized Surface Plasmon
SPP	Surface plasmon polariton
SPAD	Single Photon Avalanche Diode
TCSPC	Time-Correlated-Single-Photon-Counting

ABSTRACT

Newman, Ward D. PhD, Purdue University, December 2017. Experimental Demonstration of Engineered Dipole-Dipole Interactions in Nanophotonic Environments. Major Professor: Zubin Jacob.

Zero point fluctuations of the electromagnetic radiation field have profound effects on the electronic states of atoms and molecules. For example, vacuum fluctuations of the photonic radiation field stimulate the spontaneous decay of excited states of atoms (spontaneous emission), shift atomic energy levels (Lamb Shift), and allow nearby atoms and molecules to couple via dipole-dipole interactions (van der Waals interactions, Casimir effect, super radiance, Förster resonance energy transfer). The control and modification of vacuum fluctuations has been a long-standing theme in quantum engineering as one can then truly control single photon emission and alter dipole-dipole interactions spatial scaling with distance. The ability to do so would have far reaching impacts in physics (quantum computing and cryptography), engineering (harnessing van der Waals forces), and bio-imaging. In this thesis we leverage the emerging new technology of metamaterials to design and fabricate devices that facilitate strong light matter interactions and allow for long-range dipole-dipole interactions among quantum emitters.

Our approach utilizes the unique photonic modes and intrinsically broadband nature of hyperbolic metamaterials, uniaxial media with extreme anisotropy. We show experimentally that hyperbolic media fundamentally extend the non-radiative near-fields of dipole-dipole interactions. In conventional media, these non-radiative near-fields decay dramatically with distance curtailing interactions to only a few nanometers. This first experimental demonstration was achieved through synergistic advances in theory, ultrafast optics, low-light level detection and nanofabrication. We find that

dipole-dipole interactions are not directly related to the photonic density of states, but instead are quantified by the *two-point spectral density function*, a physical quantity distinct from the photonic density of states. We engineer this quantity and construct a metamaterial device that displays dipole-dipole interactions far beyond the range of the conventional Coulombic near-field, achieving *Super-Coulombic Dipole Interactions*. Our approach is distinct from existing techniques which generally rely on narrow band resonant cavities or band edge photonic crystals to engineer the radiative far-field interactions.

We also design a hyperbolic metamaterial device to enhance and direct the spontaneous emission from isolated fluorescent emitters. Stimulating experimental evidence demonstrates that hyperbolic metamaterials are viable candidates for enhancing single photon emission into well defined spatial modes.

This thesis also describes rigorous metamaterial fabrication and design principles, and presents experimental isolation of unique Ferrel-Berreman modes in epsilon-near-zero media which are radiative collective charge oscillations in ultrathin films.

Finally, we make advancements in nanofabrication of disordered plasmonic media that achieves localized plasmonic resonances to demonstrate giant enhancement in many-body dipole-dipole interactions. From experiments, we infer that the normally spherically symmetric near-field Coulombic potential is anisotropic above disordered gold nano-particle substrates.

We envision that controlled dipole-dipole interactions can impact deterministic entanglement creation between remote emitters, quantum coherence in metamaterial mediated photosynthetic energy transfer, lead to many-dipole interactive states in metamaterials, increase the range of biomolecular FRET rulers as well as FRET imaging systems, and accelerate progress towards the long-standing goal of strongly coupled quantum systems at room temperature ($V_{dd} > k_{\mathrm{B}}T_{room}$).

1. ENGINEERING THE QUANTUM VACUUM

1.1 Light-Matter Interactions

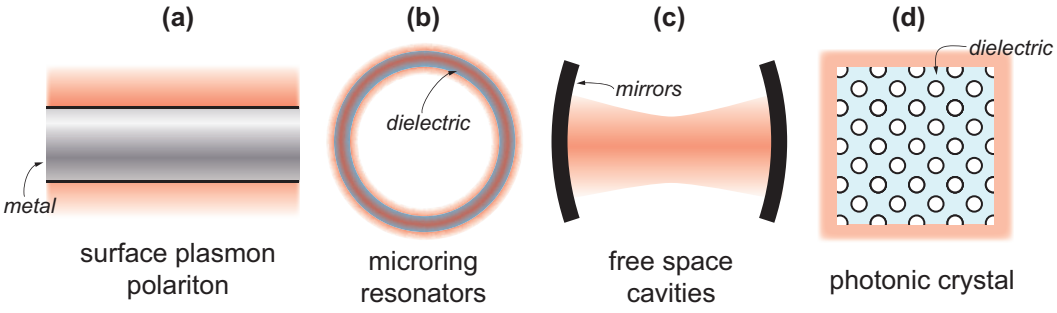

Fig. 1.1. Every electromagnetic (photonic) mode is quantized and posseses zero-point-fluctuations, finite electromagnetic fluctuations/noise. (a) Metal-dielectric interfaces support surface plasmon polaritons, (b) microring resonators support guided mode resonances, and (c) free space cavities support Fabry-Perot resonances; the ground state of each of these photonic modes is populated with zero-point-fluctutations. (d) The interior of a photonic crystal has a photonic bandgap, supporting no modes. In this case there is no zero-point-fluctuations because there exists no modes! In this thesis we utilize plasmonic Metamaterials to engineer vacuum fluctuations with the ultimate end goal of fundamentally extending the range of dipole-dipole interactions and enhancing single photon sources. The key principle is that the dispersion of quantum vacuum is altered by a homogeneous material response as opposed to resonant structures.

The quantization of the electromagnetic radiation field described by Maxwell's equations shows the well known result that radiation is absorbed and emitted in discrete bundles called photons [1]. One peculiar result of this quantized electromagnetic field is that the ground state of vacuum, a volume of empty space containing no photons nor matter, has finite fluctuations in the electric and magnetic fields,

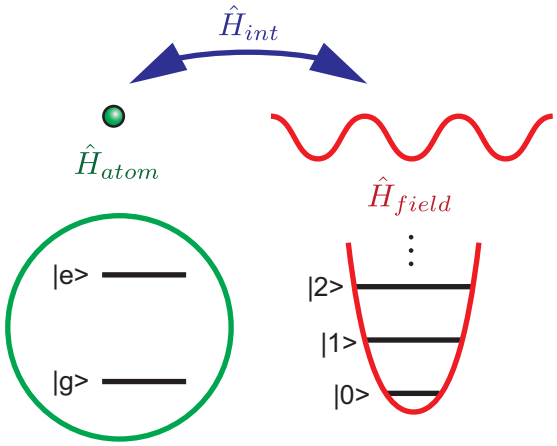

Fig. 1.2. *Single-atom radiation field interactions.* The photon states of the electromagnetic radiation field (right, red) interacts with the states of an atom or molecule (left, green) through an interaction Hamiltonian $\hat{H}_{int}$. This interaction Hamiltonian couples the normally stable atomic states and causes transitions between atomic energy levels. $\hat{H}_{\text{atom}}$ is the Hamiltonian describing the unperturbed atomic states, and $\hat{H}_{field}$ is the Hamiltonian describing the unperturbed photon states.

analogous to the ground state motion of the quantized harmonic oscillator [2]; these zero photon ground state fluctuations are called the zero-point-fluctuations or vacuum fluctuations [3]. Interestingly, the macroscopic Maxwell's equations describing electromagnetic radiation in and around materials $(\epsilon(\vec{r}), \mu(\vec{r}))$ can also be quantized and thus show that any electromagnetic mode (solutions to Maxwell's equations) also exists as discrete quanta and has zero-point-fluctuations. Figure 1.1 shows a few such modes, each of which has zero-point-fluctuations and whose strength is distributed in space according to the modal profile of the specific photonic mode [2–4].

The actual existence of these vacuum fluctuations is well established and gives rise to a myriad of well known observable phenomena: spontaneous emission [1, 5]; the Lamb shift [6, 7]; van der Waal's forces and the Casimir effect [8]; Förster resonance energy transfer (FRET) [9]; and, spontaneous parameteric downconversion [10–12]. Recent experiments (2015-17) have shown that vacuum fluctuations can be measured directly; ground state noise at one frequency can be imprinted on the polarization

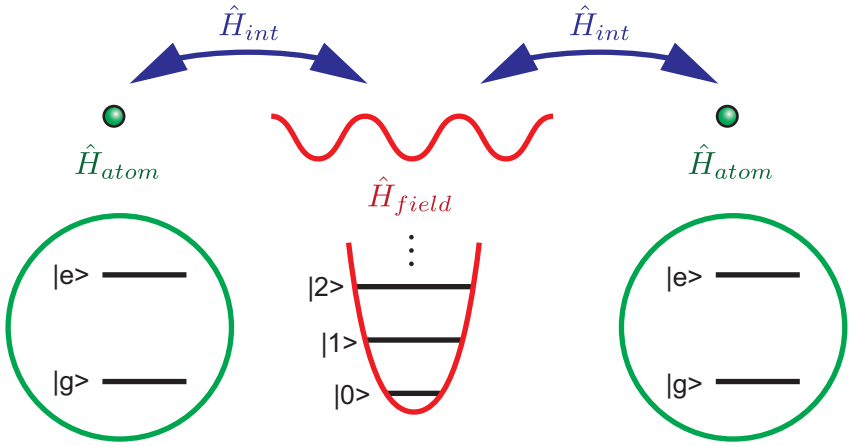

Fig. 1.3. *Multiple atoms interacting via radiation field.* The energy levels of atoms and molecules can mutually interact through the radiation field as in van Der Waals forces, Dicke Super Radiance, and Förster Resonance Energy Transfer. The atoms do not directly interact; the coupling between the them is mediated by their individual coupling with the photon field. The Hamiltonians are as defined in the caption of figure 1.2. The dominant coupling between atoms is through dipole-dipole interactions.

state of a laser at a different frequency via coupling in an electro optic crystal. The noise of the vacuum fluctuations can then be directly read out with classical polarization optics [13, 14].

While spontaneous emission and the Lamb shift arise from a single atom (or molecule) interacting with the electromagnetic vacuum fluctuations (figure 1.2), van der Waal's forces, super radiance, FRET and the Casimir effect arise from two or more atoms mutually interacting through the quantum ground state of vacuum (figure 1.3). These quantum interactions are fully characterized to first order (dipole approximation) by Coulombic dipole-dipole interactions whose strength V_{dd} decreases rapidly with distance, scaling as $V_{dd} \sim 1/r^3$ in the near-field [4, 9, 15, 16]. We note that these interactions between atoms and molecules separated by a small vacuum gap are not due to electron wavefunction overlap, but stem from the existence of fluctuations in the ground state of the photon field.

Engineering dipole-dipole interactions is paramount for both fundamental science and device technology, and as such has been a long standing goal of quantum engineering due the breadth of physical phenomena whose root cause is dipole-dipole couping. For example, extending the range of atom-atom coupling via dipole-dipole interactions would serve as a rich testing ground for long-range quantum entanglement, but can also result in practical technology relating to quantum state engineering.

In this thesis, we leverage the emerging physics of metamaterials, bulk media with designed and exotic optical properties, for the ultimate purpose of extending near-field dipole-dipole interactions to the far-field. The thesis starts by detailing the microscopic physics and photonic mode structure of nanofabricated epsilon-near-zero (ENZ) metamaterials; we observe unique bulk plasmon modes that couple to the optical far-field called Ferrell-Berreman modes and cause a polarization sensitive absorption in ENZ metamaterials. Next, we design a hyperbolic metamaterial based single photon source and provide an experimental proof of principle for its promise as an efficient nanoscale light source. We then provide experimental verification of Super-Coulombic dipole-dipole interactions, an extension of the Coulombic near-field of dipole-dipole coupling, by showing long range resonant energy transfer ten times the traditional near-field. Lastly, we provide an outlook on promising evidence for engineering and harnessing dipole-dipole interactions using disordered plasmonic substrates. The basic principles of engineering the quantum vacuum with hyperbolic metamaterials and the corresponding applications for single photon sources and Super-Coulombic dipole-dipole interactions is outlined in the next sections.

1.2 Engineering Dipole-Dipole Interactions

1.2.1 Two Point Spectral Energy Density Function

It has been shown conclusively that vacuum fluctuations can be locally tailored with photonic structures to strongly affect spontaneous emission by engineering the local photonic density of states (LDOS), loosely speaking the density of vacuum fluc-

tuations at the fluorophore location [1, 5]. The LDOS is quantified by the Green's function at the location of the fluorophore $G(\omega, \vec{r}, \vec{r})$. This has led a number of breakthroughs in engineering materials and structures for tailoring spontaneous emission for highly efficient single photon fluorescence sources [17–29]. Complementary to this, photonic bandgap structures have been designed to inhibit spontaneous emission by expelling any vacuum fluctuations (see figure 1.1) [30–33].

However, dipole-dipole interactions can not be controlled by engineering the photonic density of states and a fundamentally different approach must be used [34]. Instead dipole-dipole interactions are quantified by the *two-point spectral density function* (S_{EE}), a physical quantity distinct from the photonic density of states (see Chapter 4 and appendices). S_{EE} can be rigorously quantified by the evaluation of the Green's function of fluorophore at position $\vec{r}_A$ at the separate location of the fluorophore at position $\vec{r}_B$ $G(\omega, \vec{r}_A, \vec{r}_B)$. S_{EE} scales rapidly with distance r in the near-field $1/r^3$ while in the far-field it scales slowly as a radiative interaction $1/r$.

The control and modification of dipole-dipole interactions' rapid scaling with distance has become a long-standing theme in quantum engineering. Progress in the engineering of dipole-dipole interactions has led to long-range qubit interactions in circuit QED [35], super-radiance in atoms and quantum wells mediated by photonic crystals [36, 37], collective Lamb shifts of atoms in cavity QED [38], enhanced energy transfer between molecules in cavities [39] and quantum phases in optical lattices [40].

A unifying theme in these approaches, however, is the enhancement of radiative interactions and departure from the far-field ($V_{dd} \sim 1/r$) scaling of interaction with distance. A still outstanding challenge has been the control of the non-radiative Coulombic near-field interactions which scale considerably faster with distance ($V_{dd} \sim 1/r^3$) and are conventionally limited to the extreme near-field [3]. Here we utilize Hyperbolic metamaterials to tailor the quantum vacuum and extend the Coulombic near-field of dipole-dipole interactions. The basic principles of this are shown in figure 1.4.

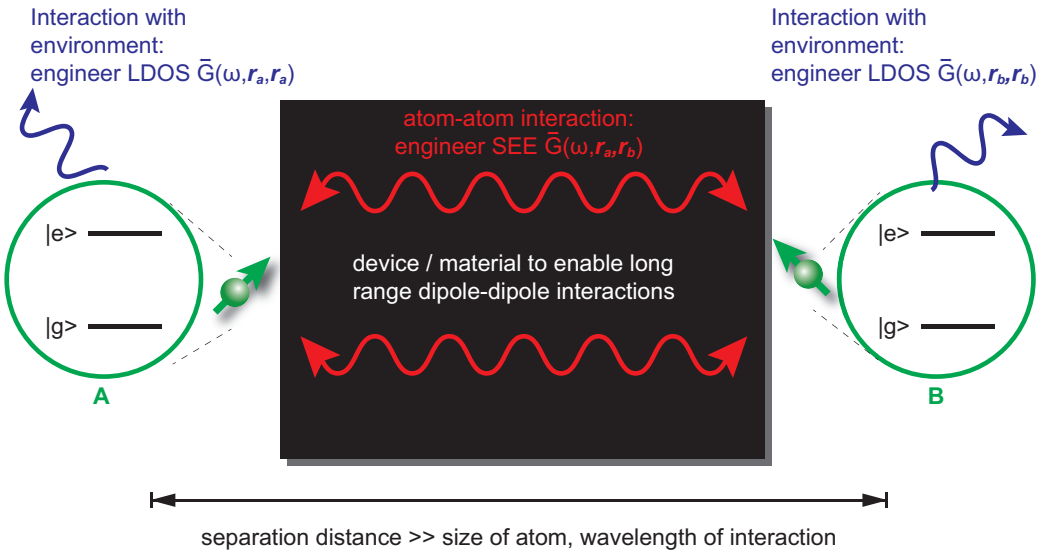

Fig. 1.4. Interactions of atoms and fluorophores with the evniron-ment are engineered by tailoring the local photonic density of states (LDOS). Dipole-dipole interactions are governed by the two point spectral energy density (S_{EE}) and are engineered separately from the LDOS. Here we utilize hyperbolic media to extend the Coulombic near-field of S_{EE}) to the far-field to enable long-range non-radiative dipole-dipole interactions.

1.2.2 Super-Coulombic Dipole-Dipole Interactions in Hyperbolic Media

Hyperbolic media are a class of uniaxial crystal whose optical response is described by a dielectric tensor with extreme anisotropy: $\bar{\bar{\epsilon}} = \text{diag}[\epsilon_x, \epsilon_x, \epsilon_z]$ with $\epsilon_x \cdot \epsilon_z < 0$. Fourier analysis of Maxwell's equations in such media show that the dispersion relation for plane extraordinary waves (TM polarization) in such a crystal is $\omega^2/c^2 = k_\rho^2/\epsilon_z + k_z^2$, where ω is the temporal frequency, c is the speed of light, k_ρ is the transverse wavevector (normal to the crystal optic axis), and k_z is the wavevector parallel to the optic axis. As shown in figure 1.5, for materials with extreme anistropy, the dispersion relation is hyperbolic and there is no upper cutoff to the spatial frequencies allowed to propagate within the bulk. This is in stark contrast to traditional dielectrics with $\epsilon_x \cdot \epsilon_z > 0$ whose dispersion relation is spherical (or elliptical) [41]. These so called high-k modes of hyperbolic media are collectively referred to as hyperbolic polaritons.

Hyperbolic media have garnered intense interest since 2005 due to the lack of a spatial wavevector cut-off as described in figure 1.5 [42]. The initial burst of interest for this exotic property was for sub-diffraction imaging applications [43,44]. However, around the beginning of this thesis work (2010-2011), it was noted that media with an unbound hyperbolic dispersion provide a diverging density of photonic states and thus quantum processes such as spontaneous emission will be significantly enhanced near such materials [17, 45]. Most importantly, Cortes and Jacob [46], and Milton et al. [47] have recently shown that media with hyperbolic dispersion can fundamentally alter the strength and spatial scaling of dipole-dipole interactions.

Theoretically, hyperbolic metamaterials cause an indefinite extension of extreme short-range dipole-dipole distance scaling $V_{dd} \sim 1/r^3$ despite the physical separation between interacting quantum emitters [46, 47]. Since the non-radiative Coulombic near-field is extended indefinitely, we call these interactions Super-Coulombic Dipole-Dipole Interactions. As shown in figure 1.6, this route to controlling dipole-dipole interactions is a significant departure from current resonant approaches (photonic

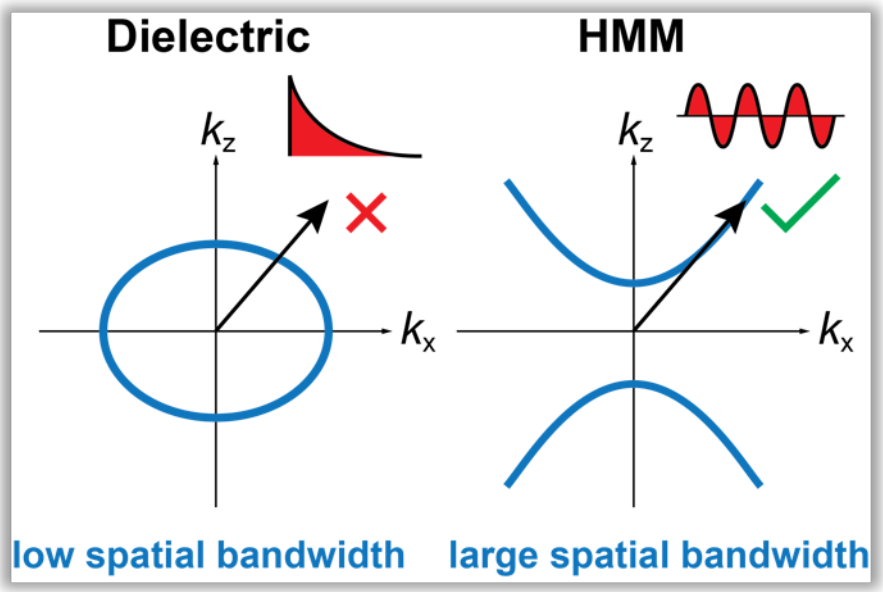

Fig. 1.5. Iso-frequency curves for dielectric media and hyperbolic media are shown. Conventional materials such as a dielectric ($\epsilon > 0$) have closed iso-frequency curves, limiting the maximum spatial frequency that is allowed to propagate. Hyperbolic media ($\bar{\bar{\epsilon}} = \text{diag}[\epsilon_x, \epsilon_x, \epsilon_z]$, $\epsilon_x \cdot \epsilon_z < 0$) have a hyperbolic isofrqeuency curve and there is no cut-off to the spatial frequencies that can propagate within the bulk of the material. We utilize this property to engineer light-matter interactions and long-range dipole-dipole interactions.

crystals and resonant cavities) that alter only the weak far-field $\sim 1/r$ scaling of the interaction.

To show this novel effect, we utilize Förster Resonance Energy Transfer (FRET), a form of resonant dipole-dipole interactions (RDDI), as a probe . We fabricate a 100 nm thick metal-dielectric multilayer possessing an effective hyperbolic dispersion and observe FRET between donor and acceptor fluorophores separated by the metamaterial. Using time-resolved fluorescence emission measurements, a marked reduction in the excited state lifetime of the donor fluorophores; as described in detail in Chapter 4, these observations indicate, a long-range Coulombic dipole-dipole interaction and offer proof of the extension of the non-radiative Coulombic near-field of dipole-dipole interactions.

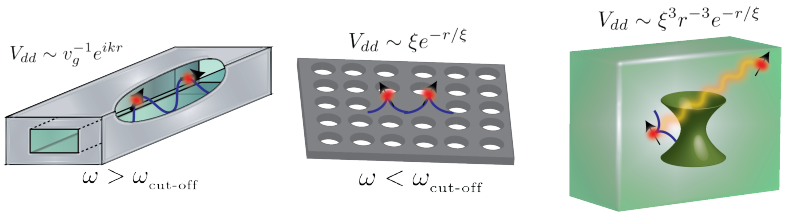

Fig. 1.6. Comparison of dipole-dipole interactions (V_{dd}) in metallic waveguides, photonic crystal band-edge structures and hyperbolic metamaterials. Here r is the distance between interacting emitters, v_g is the group velocity of the waveguide mode with wavevector k, $\omega_{cut-off}$ is the cut-off frequency of the metallic waveguide mode or photonic crystal and ξ is an interaction range. (A) When the transition frequencies of interacting atoms lie above the cut-off, they will have a sinusoidal-type interaction; (B) on the other hand, at the band-edge of a photonic crystal there occur interactions with a divergent strength as well as range (C) Hyperbolic media exhibit fundamentally different Coulombic long-range interactions which diverge for specific angular directions in the low-loss effective medium limit.

It should be noted that a simple semiclassical model can also be used to understand FRET in the weak coupling (irreversible) limit. However, the theory developed by our group [46] takes a unified approach to understand all resonant dipole-dipole interaction effects beyond FRET such as super-radiance, collective Lamb shift and Casimir-Polder force. These effects are all manifestations of RDDI but sensitively depend on the initial state preparation conditions. No semiclassical theory can take into account all the effects in this unified form and a quantum electrodynamic theory is necessary.

1.2.3 Resonant Dipole-Dipole Interactoins in Disordered Plasmonic Media

For engineering dipole-dipole interactions, the primary challenge for the field is increasing rates of interaction beyond those of decoherence (i.e. coupling to the

environment) at room temperature. The issue of using a simple Purcell factor (LDOS engineering) approach is that it increases coupling to the environment (i.e. cavity) and only modestly changes the interactions. Here, the first step towards achieving interactions between quantum emitters at the same strength as their independent interactions with the environment is proposed and demonstrated through the use of disordered plasmonic media.

A summary of the work and relevant distance scales is shown in figure 1.7. We fabricate self-assembled disordered gold nanoparticle (NP) films via conventional sputtering and a rapid annealing process. We then probe near-field resonant dipole-dipole interactions (RDDI) by monitoring Förster Resonance Energy Transfer (FRET) in thin-films above the gold NPs. The key here is the energy transfer bandwidth between donors and acceptors overlaps with the gold NPs' localized surface plasmon resonances. Interestingly, we observe an enhancement of RDDI strengths of 13× relative to those on glass and these outpace the coupling strengths of the dipoles with the gold NPs (spontaneous emission enhancement of 9×). As a result, we observe a 10% increase in FRET quantum efficiency relative to the same mixture on glass. A careful analysis of fabricated control samples leads us to infer the FRET radius, the characteristic interaction distance has increased by 50%!

1.3 Overview of Thesis

The thesis is arranged as follows:

In Chapter 2, we explore the photonic modes of epsilon-near-zero (ENZ) metamaterials. We experimentally observe unique absorption resonances in silver/silica multilayer-based (ENZ) metamaterials that are related to radiative bulk plasmon-polariton states of thin-films originally studied by Ferrell (1958 [48]) and Berreman (1963 [49]). In this chapter we make nanofabrication and characterization advances on ultra-smooth thin films and metamaterials. We use Ferrel-Berreman modes as a key characterization tool later for multilayer thin film hyperbolic metamaterials as well

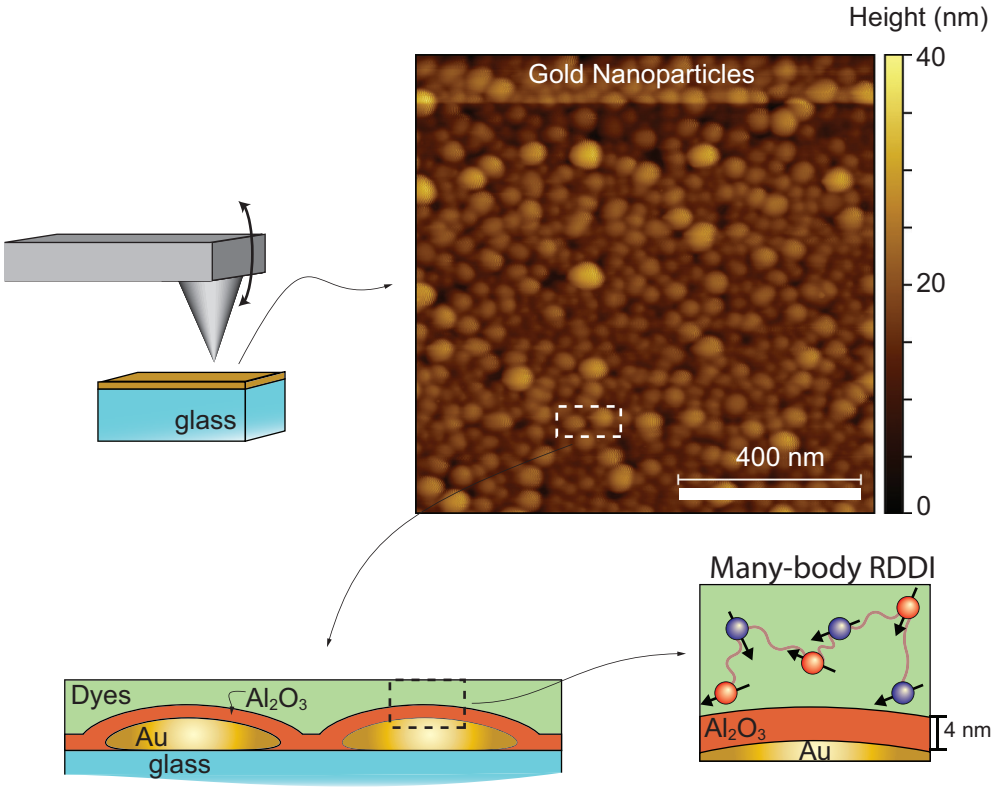

Fig. 1.7. Disordered gold nanoparticle films display enhanced resonant dipole-dipole interactions. Top: Atomic Force Microscope thickness map of a typical sample reveals the presence of gold nanoparticles. Bottom Left: A schematic of the nanoscale structure. Bottom Right: A schematic of the many-body resonant dipole-dipole interactions (RDDI) observed in experiment. We observe that the interactions between dipoles near the metallic nanoparticles exceeds their individual interactions with the nanoparticles.

as disordered plasmonic media. This thesis utilized a host of deposition approaches such as e-beam evaporation, sputtering and atomic layer deposition to fabricate metamaterials. At the same time, we also utilized a suite of characterization approaches including ellipsometry, spectrophotometry, x-ray diffraction analysis and atomic force microscopy to quantify the quality of the practically achieved metamaterial response. An increasing number of research groups are now exploring the use of Ferrel-Berreman modes in nonlinear and switching phenomena and using the mode to quantitatively characterize the epsilon-near-zero wavelength of any thin film. We believe our work can emerge as an important benchmark for verifying the ENZ behavior of any thin film including Indium Tin Oxide (ITO), Aluminum Zinc Oxide (AZO) and Titanium Nitride (TiN).

In chapter 3, we design a hyperbolic metamaterial device to enhance and direct the spontaneous emission from isolated fluorescent emitters. We provide stimulating experimental evidence demonstrating that hyperbolic metamaterials are viable candidates for enhancing single photon emission into well defined spatial modes. At the time of publication, it was the first design to address the challenge of out-coupling light efficiently from a hyperbolic metamaterial. Previous work in the field suffered from the significant drawback that outcoupling efficiency was low and absorption loss was significantly large. This theoretical work stimulated an intense experimental effort in the group of Prof. Vinod Menon (City University of New York) on successful light outcoupling strategies from hyperbolic media [50].

In chapter 4, we show that metamaterials can fundamentally modify dipole-dipole interactions and cause a near-field Coulombic scaling in spite of large physical separation between interacting quantum emitters. We measure a two orders of magnitude increase in the near-field resonant dipole-dipole interactions (RDDI) and the show surprising extension of the characteristic non-radiative Coulombic scaling law of RDDI to intermediate field distances (10 times the near field).

In chapter 5, we present exciting evidence that disordered plasmonic substrates enhance dipole-dipole interactions. We observe a 50% increase in the effective FRET

radius and thirteen times increase in the energy transfer rate between donor-acceptor mixtures deposited on self-assembled, disordered plasmonic films. We believe that this increased range of dipole-dipole interactions on disordered gold nanoparticle substrates will lead to a simple solution for increased FRET interactions in bio-imaging, and also lead to new directions of research of dipole-dipole interactions in random media.

A comprehensive set of appendices outlining the experimental techniques and key specifications used in this thesis is provided at the end. These appendices will serve as a detailed guide to other experimentalists and theorists working towards engineered dipole-dipole interactions and single photon sources via nanofabricated metamaterials.

2. FERRELL-BERREMAN MODES IN PLASMONIC EPSILON NEAR ZERO MEDIA

We observe unique absorption resonances in silver/silica multilayer-based epsilon-near-zero (ENZ) metamaterials that are related to radiative bulk plasmon-polariton states of thin-films originally studied by Ferrell (1958) and Berreman (1963). In the local effective medium, metamaterial description, the unique effect of the excitation of these microscopic modes is counterintuitive and captured within the complex propagation constant, not the effective dielectric permittivities. Theoretical analysis of the band structure for our metamaterials shows the existence of multiple Ferrel-Berreman branches with slow light characteristics. The demonstration that the propagation constant reveals subtle microscopic resonances can lead to the design of devices where Ferrell-Berreman modes can be exploited for practical applications ranging from plasmonic sensing to imaging and absorption enhancement.

2.1 Principle of Optical Metamaterials

In naturally occurring materials, the bulk properties such as the refractive index are governed by the complex three-dimensional arrangement of atoms and molecules: the atomic lattice. Despite the microscopic complexity, the effect the material has on monochromatic optical field can be well characterized by two single parameters (or tensors), the relative dielectric permittivity ϵ and the relative magnetic permeability μ.[1] Optical metamaterials are engineered, artificial media that have macroscopic electromagnetic properties (ϵ, μ) resulting from the designed nanoscopic structure. Metamaterials are composed of periodically arranged unit-cell building blocks with a

[1]Of course ϵ and μ are spectrally dispersive, that is $\epsilon \to \epsilon(\omega)$ and $\mu \to \mu(\omega)$; however, this spectral dependence has been suppressed for brevity.

characteristic size much smaller than the optical wavelength. To lowest order, these metamaterials are described as a single effective dielectric permittivity tensor $\bar{\bar{\epsilon}}$ and magnetic permeability tensor $\bar{\bar{\mu}}$ (figure 2.1). By designing the resonances of the unit cells and the mutual coupling between unit cells, a bulk electromagnetic response can be tailored to achieve exotic properties not available with natural or conventional materials.

In the fictitious metamaterial example shown in figure 2.1, it is clear that the optical response would be anisotropic as different polarizations and propagation directions of an electromagnetic wave would drive different plasmonic resonances along the metallic extruded cross object. Tuning the mutual coupling between adjacent unit cells hybridizes the single particle resonances and thus provides a method for tailoring the bulk optical response [51–54]

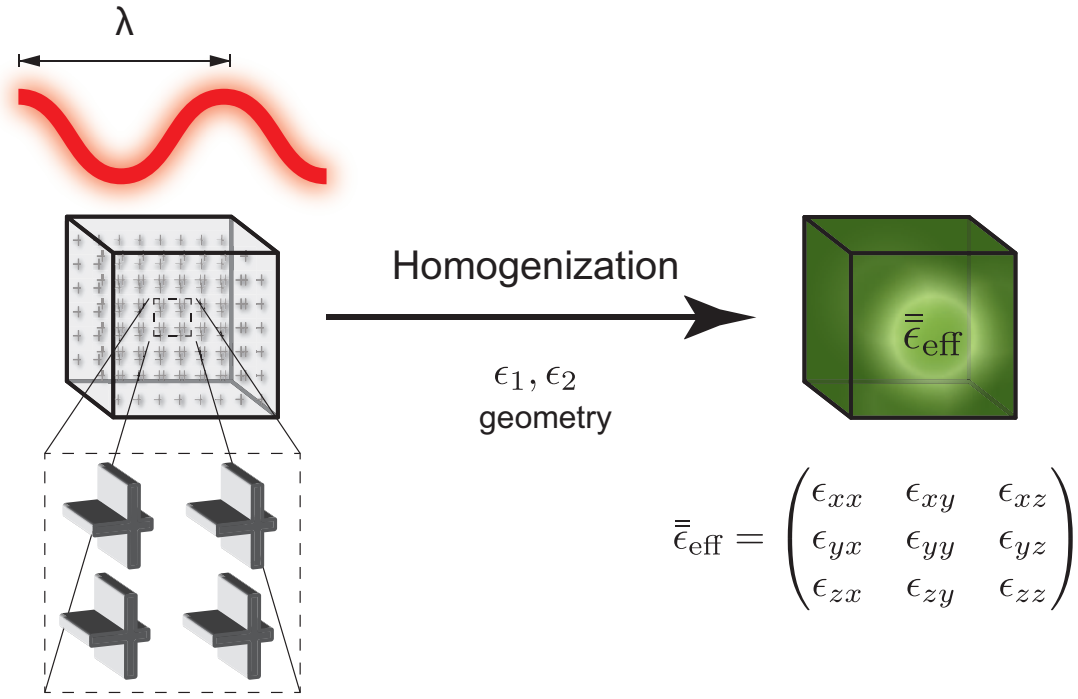

Fig. 2.1. A material composed of periodic arrays of sub-wavelength building blocks yields an effective anisotropic dielectric tensor. This effective dielectric tensor can be engineered by designing the shape and relative positioning of the building blocks.

Metamaterial technologies have matured over the past decade for a variety of applications such as super-resolution imaging [43, 55, 56], cloaking [57] and perfect absorption [58]. Various classes of metamaterials have emerged that show exotic electromagnetic properties like negative index [59, 60], optical magnetism [61] , giant chirality [62–64], epsilon-near-zero [65, 66], bi-anisotropy [67] and spatial dispersion [68] among many others.

2.2 Epsilon Near Zero Metamaterials

An important class of artificial media are the epsilon-near-zero (ENZ) metamaterials that are designed to have a vanishing dielectric permittivity $|\epsilon| \to 0$. Waves propagating within ENZ media have a divergent phase velocity that can be used to guide light with zero phase advancement through sharp bends within sub-wavelength size channels [69, 70], or to tailor the phase of radiation/luminescence within a prescribed ENZ structure [71, 72]. The electric field intensity within an ENZ medium can be enhanced relative to that in free space leading to strong light absorption [73]. This enhanced absorption in ENZ media has been exploited for novel polarization control and filtering in thin films [74], as well the proposal to use ENZ absorption resonances to tune thermal blackbody radiation of a heated object to the band-gap of a photovoltaic cell [75]. An enhanced non-linear response based upon strong spatial dispersion of waves in ENZ media has been demonstrated, and proposed for all-optical switching [53, 54].

Here we show theoretically and experimentally that ENZ metamaterials support unique absorption resonances related to radiative bulk plasmon-polaritons of thin metal films. These radiative bright modes exhibit properties in stark contrast to conventional dark modes of thin-film media (surface plasmon polaritons). The unique absorption resonances manifested in our metamaterials were originally studied by Ferrell in 1958 for plasmon-polaritonic thin-films in the ultraviolet [48], and by Berreman in 1963 for phonon-polaritonic thin-films in the mid-infrared spectral region [49].

Surprisingly, two research communities have developed this independently with little communication or overlap until now: we therefore address these resonances as Ferrell-Berreman (FB) modes of our metamaterials. Counterintiutively, in the metamaterial effective medium picture, these resonances are not captured in the metamaterial dielectric permittivity constants but rather in the effective propagation constant. Furthermore, we show the existence of multiple branches of such FB modes that have slow light characteristics fundamentally different from the single thin film case. Our work can lead to applications where FB modes are used for thin-film characterization [76], sensing [77], imaging [78], absorption enhancement [79] and polarization control [80].

An isotropic ENZ occurs naturally in metals such as silver and aluminum, and in polar dielectrics such as silicon carbide and silicon dioxide. However, due to the low effective mass of electrons, the ENZ inevitably occurs in the ultraviolet (UV) spectral range for metals ($\omega_p \propto 1/\sqrt{m_e}$). On the other hand the large effective mass of ions shifts the ENZ at the longitudinal optical phonon frequency to the the infrared (IR) spectral range for polar dielectrics ($\omega_{LO} \propto 1/\sqrt{M_{ion}}$). Thus very few natural materials exhibit ENZ behaviour in the optical frequency range, and designed artifical media must be used for ENZ-based applications in the visible [54,81]. Here, we design ENZ media using silver (Ag) /silica SiO_2 multilayers with nanoscale, sub-wavelength layer thicknesses to achieve a tunable anisotropic ENZ at optical frequencies.

Zeroth order Maxwell-Garnett Effective Medium Theory (EMT) shows that the permittivity of multilayer structures composed of a subwavelength thickness metal/dielectric unit cells with dielectric constants ϵ_m and ϵ_d, and layer thicknesses d_m and d_d is indeed uniaxially anisotropic. The response of the multilayer is described via a dielectric permittivity tensor of the form $\bar{\bar{\epsilon}}_{\text{eff}} = \text{diag}[\epsilon_{||}, \epsilon_{||}, \epsilon_{\perp}]$, where $\epsilon_{||} = \rho\epsilon_m + (1-\rho)\epsilon_d$ is the permittivity for polarizations along the layer interfaces, and $\epsilon_{\perp} = (\rho/\epsilon_m + (1-\rho)/\epsilon_d)^{-1}$ is the permittivity for polarizations perpendicular to the layer interfaces. $\rho = d_m/(d_d + d_m)$ is the metal volume filling fraction.

We apply the local EMT model that is valid for free space wavelengths that are much longer than the multilayer unit cell thickness equal to $d_m + d_d$. However, it has been shown that this local EMT model fails to accu-rately describe the highly confined Bloch surface plasmon-polariton modes of metal/dielectric superlattices (so called high-k waveguide modes of hyperbolic metamaterials). There has been significant development of a non-local EMT that more accurately describes the high-k waveguide modes of metal/dielectric superlattice-based metamaterials [82–85]. In this chapter we study photonic modes that can be excited from free space (exist within the light cone) and are therefore not deeply sub-wavelength. Our simulations of practical multilayer structures beyond the effective medium model consider the role of finite unit cell size, absorption and dispersion. The results show strong agreement with experimental observations.

The permittivity of almost all traditional metals can be approximated using free-electron Drude dispersion and using this fact, we see that the parallel dielectric constant $\epsilon_{\parallel}$ is a modified Drude-like dispersion, and the presence of the weakly dispersive dielectric layers effectively adds a positive background dielectric constant. As a result, the dielectric layers serve to dilute the metal and red-shift the effective plasma frequency of the multilayer superlattice. The metamaterial has an ENZ in the parallel direction at the spectral frequency satisfying the relation $\rho\epsilon_m(\omega_{ENZ}) = -(1-\rho)\epsilon_d$. We can thus tune the parallel permittivity ENZ frequency by choosing an appropriate metal $\epsilon_m(\omega)$, dielectric ϵ_d, and fill fraction ρ. Similarly, the perpendicular permittivity $\epsilon_{\perp}$ has a Lorentz-like response with a resonance pole at the spectral frequency satisfying the relation $(1-\rho)\epsilon_m(\omega_{LP}) = -\rho\epsilon_d$. The Lorentz-resonance pole for the perpendicular permittivity $\epsilon_{\perp}$ is blue-shifed to higher frequencies with decreasing fill fractions of metal while the resonance pole quality is reduced.

2.3 Experimental Evidence of Radiative Bulk Plasmons in ENZ Metamaterials

Figure 2.2(a)-(c) shows the calculated dispersion of the effective medium dielectric constants for silver/silica metamaterials with various fill fractions of silver. The fill fractions shown in Figure 2.2 correspond to multilayers with silver thickness 20 nm and silica thickness 20, 30 and 40 nm. We see that the ENZ in the parallel direction can be spectrally tuned by varying the relative fill fraction of the silver within the metamaterial. We also note that a resonant ENZ effect can occur in the perpendicular component of the dielectric constant as well; however the dissipative, lossy component of the perpendicular permittivity is relatively large with $\mathrm{Im}[\epsilon_\perp] \sim 1 - 10$ in the perpendicular direction. This severely weakens the observable ENZ effects. Furthermore, we emphasize that for small enough fill fractions of silver, the Lorentz-resonance pole in the permittivity in the perpendicular direction is weakened to that point where the real part of the perpendicular permittivity does not vanish at all, as shown in Figure 2.2(c).

We now discuss wave propagation through multilayer metamaterial slabs. The dispersion of p-polarized plane waves with wave vector $\vec{k}$ and spectral frequency ω is described by the equation $k_\parallel^2/\epsilon_\perp + k_\perp^2/\epsilon_\parallel = k_o^2$ for waves in the metamaterial. We define $k_\perp = \sqrt{\epsilon_\parallel(k_o^2 - k_\parallel^2/\epsilon_\perp)}$ as the propagation constant of waves in the metamaterial. Figure 2.2(d) shows the imaginary part of the propagation constant for the three metamaterial samples shown in Figure 2.2(a)-(c),and for bulk silver. We see the metamaterials possess a spectral range where the attenuation of waves within the medium is low (small $\mathrm{Im}[k_\perp]$). Over this spectral range the metamaterial is effectively dielectric with $\mathrm{Re}[\epsilon_{\parallel,\perp}] > 0$. The real part of the propagation constant in the metamaterial $\mathrm{Re}[k_\perp]$ is close to the propagation constant of vacuum and $\epsilon_\parallel \approx \epsilon_o = 1$, thus resulting in a low reflectivity. This spectral range where both $\mathrm{Im}[k_\perp]$ and reflec-

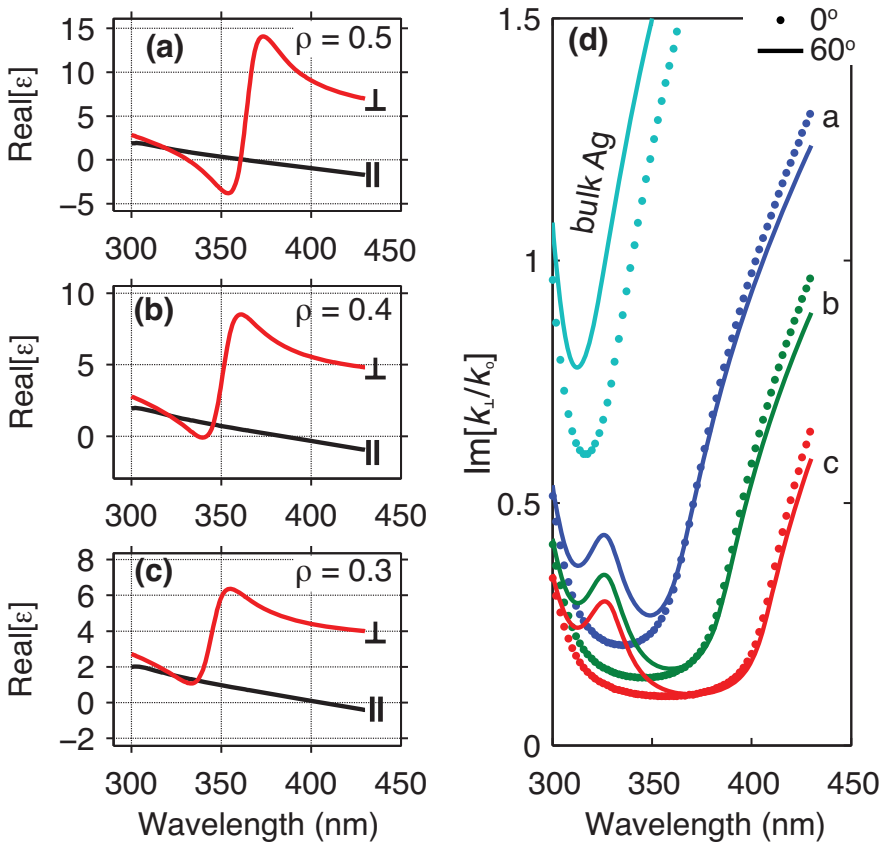

Fig. 2.2. The real part of the dielectric permittivity tensor is shown for silver/silica multilayer metamaterials with a silver thickness of 20 nm and silica thicknesses (a) 20 nm, (b) 30 nm, and (c) 40 nm. The dispersion is calculated using experimentally obtained dielectric permittivities for the constituents. (d) The imaginary part of the complex propagation constant $k_\perp$ for p-polarized light is shown for the metamaterials samples in panels (a)-(c), and for bulk silver. $\mathrm{Im}[k_\perp^p]$ governs the transparency window and exhibits an anomalous peak at the ENZ of of the constituent silver ($\lambda \approx 326$ nm) for obliquely incident light.

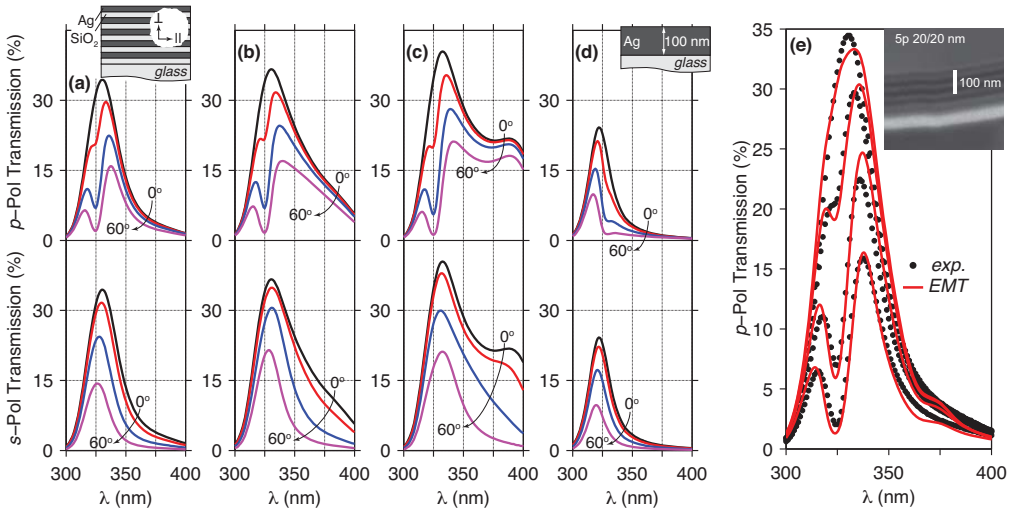

Fig. 2.3. Experimental s- and p-polarized transmission at angles of incidence 0^o, 20^o, 40^o and 60^o is shown for five period silver/silica multilayer metamaterials with layer thicknesses (a) 20/20 nm, (b) 20/30 nm, (c) 20/40 nm, and for a (d) 100 nm silver film. The excitation and subsequent dissipation of Ferrell-Berreman (FB) modes within the silver films appears as anomalous transmission for obliquely incident p-polarized light at the ENZ frequency of the constituent silver films ($\lambda \approx 326$ nm). FB modes can not be excited with s-polarized light and thus no anomalous transmission is present. The FB mode is only weakly present in the relatively thick silver film. Panel (e) shows the strong agreement of EMT calculations with experiment for the five period 20/20 nm sample. *Inset:* SEM micrograph of the sample.

tivity are small defines the transparency window of the metamaterial. Transparency windows have been exploited for optical filters in the UV [86].

We note that Figure 2.2(d) shows a counterintuitive local absorptive peak in the propagation constant for p-polarized waves obliquely incident at $\lambda \approx 326$ nm, the ENZ of silver. The spectral location of this peak is fixed, independent of the silver filling factor ρ and is not observed in bulk silver or bulk silica. It should also be stressed that this absorption peak does not occur for s-polarized waves propagating in the metamaterials. Therefore, its physical origin is not solely material absorption within the constituent layers of the metamaterial but must be due to special modal properties. We emphasize that the anomalous peak at $\lambda = 326$ nm occurs at the ENZ of the constituent silver films and does not occur at the ENZ nor at the Lorentz-pole of the metamaterial permittivity tensor components; there is no peak in the imaginary, dissipative part of the permittivity tensor components [2].

Our main aim is to show theoretically and experimentally that the physical origin of this anomalous absorption peak in metamaterial propagation constant is due to the excitation of microscopic resonances of the metamaterial: radiative bulk polaritons of thin-films which we call Ferrell-Berreman modes. This absorption peak exists within the light cone of vacuum and can therefore be observed in the free-space transmission spectrum of the metamaterials.

We deposited five-period silver/silica multilayer metamaterials on glass microscope slides via electron beam evaporation. The permittivities of silver and silica were extracted through ellipsometry on individual silver and silica films. Atomic Force Microscope measurements indicate an RMS surface roughness of $\approx 1 - 2.5$ nm. For a control sample, a 100 nm silver film was also fabricated. By volume, the control sample contains an equal amount of silver as the metamaterials. In Figure 2.2 we showed the extracted permittivity tensors and propagation constants, calculated using the extracted dielectric constants for the fabricated samples.

[2] See appendix A for the imaginary part of the dielectric permittivity tensors

Figures 2.3(a)-(c) show the experimentally observed *s*- and *p*-polarized specular transmission through the three silver/silica multilayer samples and through the control sample. Each metamaterial displays a transparency window whose width increases as the metal is diluted further (decreasing ρ). As expected from EMT predictions, the three metamaterial samples exhibit a counterintuitive *p*-polarized transmission dip at the silver ENZ $\lambda \approx 326$ nm. Furthermore, we observe that this anomalous dip does not depend on the silver filling fraction nor on the total metamaterial thickness. This clearly implies that the effect is not due to cavity Fabry-Perot resonances. Another important aspect is that this anomalous transmission dip is hardly distinguishable in the 100 nm thick silver control sample (Figure 2.3(d) while the dip's spectral energy is slightly red-shifted from the ENZ of silver. Panel (e) of Figure 2.3 shows the excellent agreement between the local EMT predictions and the experimentally observed transmission.

2.4 Modal structure of metal-dielectric metamaterial and the radiative bulk plasmons - Ferrell-Berreman Modes

Through modal analysis, taking into account the finite unit cell size of the metamaterial, we now show that the physical origin of this bulk absorption in the metamaterials is due to the excitation of leaky bulk polaritons called Ferrell-Berreman modes [87, 88]. Bulk metal supports volume charge oscillations at the ENZ of the metal (bulk or volume plasmons). These excitations are a completely longitudinal wave and therefore can not be excited with free space light, a transverse wave. For films of metal with thicknesses less than the metal skin depth, the top and bottom interface couple, allowing for collective charge oscillations across the film. The bulk plasmon then is no longer purely longitudinal and can interact with free space light at frequencies near the metal ENZ [89]. This was originally pointed out by Ferrell for metallic foils [48, 90, 91], and by Berreman for polar dielectric films [49]. Our multilayer metamaterials support several of these radiative excitations which we call FB modes.

These FB modes differ from the well known surface plasmon polaritons supported by metal foils, by the fact that in surface plasmon modes, energy propagates along the surfaces of the metal, whereas in FB modes volume charge oscillations are setup across the foil and energy propagates within the bulk of the metal. Additionally, surface plasmon modes lie to the right of the light line and do not interact with free space light. The thin-film bulk polaritons we observe have transverse wavevectors similar to free space light and exist to the left of the light line. In Figure 2.4(a), we show the dispersion of the radiative bulk plasmon and the surface plasmons for a thin and a thick silver foil treated in the low loss limit. The thin vertical line is the light line of vacuum. We determine the modal dispersion by locating the poles of the reflection coefficient of the structure $r_p(k_\parallel, \lambda)$ (see appendix A and references therein for details) Here $k_\parallel = k'_\parallel + ik''_\parallel$ is the complex wavevector along the direction parallel to the interfaces. $k'_\parallel$ describes the wavelength parallel to the interface and thus phase advancement of the guided wave, while $k''_\parallel$ describes the propagative decay or attenuation. To the right of the light line we see the two well known surface plasmon modes of a single metallic thin-film: the long- and short-ranged surface plasmon polaritons (LRSPPs and SRSPPs). To the left of the light line we see the radiative bulk plasmon, FB mode of the silver film which exists at energies near the ENZ of silver. The radiative bulk plasmon mode exhibits a nearly flat anomalous dispersion with a negative group velocity $v_g = \partial\omega/\partial k'_\parallel < 0$. The negative group velocity indicates a strong presence of electromagnetic energy flow within the metal and this energy flow is opposite to the direction of phase front advancement [92].

Even in the low loss limit, the FB modes are described with a complex propagation wavevector $k_\parallel$. This fact immediately implies that FB modes attenuate as they propagate along the film due to loss of energy from radiation into free-space light. On the other hand, in the low-loss limit, the surface plasmons are described by a completely real propagation wavevector $k_\parallel$ and do not radiate.

To understand the role of the multiple FB branches in thin film metamaterials, we define the figure-of-merit for the radiative FB modes to be $FOM = L/\lambda_\parallel$ where

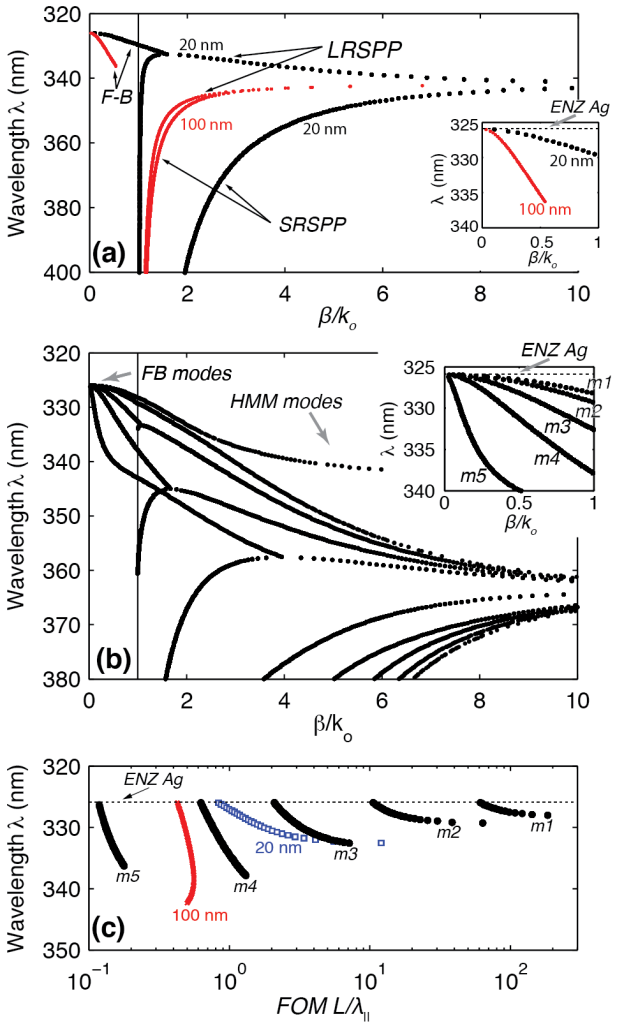

Fig. 2.4. Ferrell-Berreman (FB) mode dispersion for (a) a 20 nm and a 100 nm thick Ag foil on glass, and (b) for a 5 period 20/30 nm Ag/SiO_2 multilayer on glass. The silver and silica glass is modeled in the limit of neglible material losses. (c) Figure of merit, ratio of the decay length to the wavelength, is shown for the 20 nm and 100 nm Ag foils and the 20/30 nm Ag/SiO_2 multilayer. The large figure of merit for the metamaterial FB modes allow them to couple strongly to free-space light. Their low group-velocity, slow-light nature leads to dissipation due ohmic losses in the metal, not re-radiation to be the dominant decay channel for the FB excitations.

$L = 1/k''_{\|}$ and $\lambda_{\|} = 2\pi/k'_{\|}$ are the decay length and effective wavelength of the mode as it propagates along the film. The FOM defined here is analogous to the quality factor of the excitation. If $FOM \lesssim 1$ the FB excitation is overdamped and essentially attenuates before propagating one wavelength. The figure-of-merit gives insight to the coupling of the FB modes with free-space radiation.

Figure 2.4(c) shows the FOM for the FB modes for the thin and thick silver films. We see that for thicker films of silver, the FOM is strongly reduced relative to thin-film silver and the radiative surface mode of thick silver films interact poorly with free space light despite lying to the left of the light-line. It is worth emphasizing that as the thickness of the silver film increases, the FOM of the FB mode decreases, and in the limit of extremely thick silver film the figure-of-merit vanishes $FOM \to 0$. Thus silver films with thicknesses greater than about four to five skin-depths of silver do not support a FB mode and optical measurements will not reveal an anomalous transmission for p-polarized light. The LRSPP and SRSPP are pure surface waves and their figure-of-merit diverges in the low loss limit $FOM \to \infty$.

Note that despite treating the silver in the low-loss limit, the FB mode dispersion and FOM for the 100 nm silver film shown in Figure 2.4 agrees with the experimentally observed behaviour of silver. The observed anomalous transmission for a 100 nm silver foil on glass, shown in Figure 2.3(d), is red shifted from the $\lambda = 326$ nm ENZ of silver as predicted by modal analysis. Furthermore, the experimental dip in p-polarized transmission is hardly discernible indicating poor free-space/FB mode coupling (low FOM).

We have treated the silver films with a completely local dielectric model and predict the existence of a radiative bulk plasmon mode. The full non-local dielectric response gives rise to multiple absorption resonances called Tonks-Dattner resonances [93]. Experimental observation of these multiple bulk plasmon absorption resonances only becomes apparent for silver films thinner than about 12 nm, much thinner than the film thicknesses considered here. Our experimental results and single film / multilayer plasmonic band structure calculations are in agreement with Ferrells

original prediction that the radiative polaritons in thin metal films occur at energies slightly below the ENZ frequency. This is in complete contrast to the Tonks-Dattner resonances that are observed at energies above the ENZ frequency.

We now discuss the multiple radiative bulk plasmon, FB modes supported by metal/dielectric multilayer metamaterials that show fundamental differences from the thin film case. Figure 2.4(b) shows the predicted modal dispersion of the radiative FB modes supported by a five period 20/30 nm silver/silica multilayer on glass in the limit of negligible material losses. Analogous to the single interface surface-plasmons splitting into the LRSPP and SRSPP for a thin film of metal, the FB radiative surface plasmon of a single film splits into several radiative modes for the multilayer structure with the dominant modes existing only in a narrow spectral range below the ENZ of the silver film. Figure 2.4(c) shows that the figures of merit for the multilayer radiative FB modes are much greater than unity and they are orders of magnitude higher than the equal thickness of bulk silver (100 nm), and thus the multilayer FB modes interact strongly with freespace light. The dominant radiative state is loosely defined as the mode with the slowest group velocity and highest FOM (see mode labelled *m1* in Figure 2.4(b)-(c)).

The slow-light nature of the FB modes leads to the anomalous transmission observed experimentally. As shown in Figure 2.4, the FB excitations in thin-films have a slow, negative group velocity and long lifetimes as the mode propagate along the film. When dissipation in silver is included, a competing decay or attenuation channel for the FB modes is present. Propagation losses due to dissipative ohmic heating in the metal is enhanced for slow light [94], and thus the dissipative ohmic losses are the dominant decay channel for the FB modes, not re-radiation [90,95]. Therefore, we interpret the observed anomalous *p*-polarized transmission in the multilayer structures as the excitation and subsequent dissipation of the dominant FB mode.

We note also that the electric field profile for the FB modes excited in our multilayer metamaterial is completely different from the well-known modes in the transparency window [86]. Figure 2.5 shows the predicted electric field distribution for a

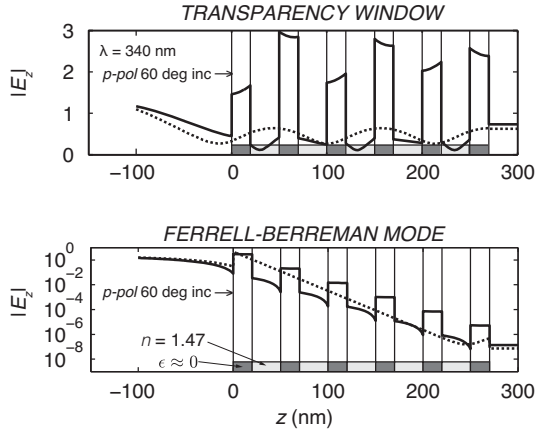

Fig. 2.5. *Top: transparency window.* At $\lambda = 340$ nm, p-polarized light obliquely incident on the metamaterial is transmitted without significant attenuation. *Bottom: Ferrell-Berreman Mode.* Within the transparency window at the plasma frequency of the constituent silver, there is an anomalous decaying mode which attenuates very rapidly and is not transmitted. Ferrell-Berreman modes are excited within the constituent silver films and charge oscillates across the volume of the silver resulting in a strong field enhancement in each silver layer. The solid curve (—) is the exact multilayer calculation and the dashed curve (- - -) is the effective medium approximation. (Note the logarithmic scale in the bottom panel.)

p-polarized 60^o obliquely incident wave upon the 20/30 nm siliver/silica multilayer. The top panel shows light incident at $\lambda = 340$ within the transparency window where both the exact multilayer and the effective medium approximation predict that the wave is transmitted through the metamaterial without significant attenuation. In the bottom panel we show light incident at the ENZ of silver $\lambda \approx 326$ nm. The FB modes are excited within the constituent silver layers resulting in a strong attenuation of the wave (note the logarithmic scale). In the exact multilayer treatment we see a strong field enhancement due to the excitation of radiative bulk plasmon modes within the metal layers. Charge oscillations are setup across the volume of the silver films resulting in a static capacitor-like electric field profile. In the effective medium picture however, the wave attenuates continuously. We emphasize, that this bulk-like loss in the effective medium approximation is highly angle and polarization dependent. In stark contrast, the normally incident and s-polarized waves are transmitted at the ENZ of the silver.

2.5 Conclusion

To summarize we have shown that metal/dielectric superlattice based epsilon-near-zero metamaterials exhibit unique micropscopic radiative bulk plasmon resonances called Ferrell-Berreman modes that can be excited with free-space light. In the metamaterial, effective medium picture the excitation of these modes is captured in the propagation constant, not in the effective dielectric permittivity constants. We observe these modes as anomalous transmission minima which lie within the transparency window of the metamaterials. These radiative volume polaritonic modes could be exploited in applications such as sensing, imaging and absoprtion spectroscopy.

3. ENHANCED AND DIRECTIONAL-SINGLE-PHOTON EMISSION IN HYPERBOLIC METAMATERIALS

It was noted in 2010 that hyperbolic media strongly influence the quantum vacuum as their lack of a spatial frequency cut-off effectively supports an infinite amount of propagating bulk modes [17]. A finite slab of such hyperbolic material supports an infinite amount of slab waveguide modes, where the wavevector along the slab can take on arbitrarily large values. Collectively, these modes are called hyperbolic polaritons: light fundamentally coupled with hyperbolic matter. The quantized macroscopic Maxwell's equations imply each of these hyperbolic modes (bulk or guided modes) is quantized; at a given frequency ω and wavevector $\vec{k}$, hyperbolic polaritons can be absorbed, emitted, scattered, etc in discrete bundles of energy $E = \hbar\omega$. Further each polaritonic mode has a quantum ground state, a state that is void of any observable (absorbable) polaritons but does indeed possess zero-point-fluctuations [2]. A fluorescent emitter (atom) in the vicinity of hyperbolic media is then coupled to the infinite amount of hyperbolic polaritons, each mode populated by zero-point noise, that effectively stimulates spontaneous emission – the emitter sees an infinite density of photonic states [1–3, 17]. Near hyperbolic media, the density of photonic radiation modes (free space) is completely overwhelmed by the density of hyperbolic polariton modes and therefore the fluorescent emitter then has an extremely high probability of emitting into the hyperbolic material.

In this chapter, we propose an approach to enhance and direct the spontaneous emission from isolated emitters embedded inside hyperbolic metamaterials into single photon beams. The approach rests on the collective plasmonic Bloch modes of hyperbolic metamaterials (hyperbolic polaritons) which propagate in highly directional beams called quantum resonance cones. We propose a pumping scheme using the transparency window of the hyperbolic metamaterial that occurs near the topo-

logical transition. Finally, we address the challenge of outcoupling these broadband resonance cones into vacuum using a dielectric bullseye grating We give a detailed analysis of quenching and design the metamaterial to have a huge Purcell factor in a broad bandwidth inspite of the losses in the constituent metal. At the end of the chapter, we provide experimental proof of principle for the hyperbolic metamaterial-based light source designed here; we provide data showing the drastically increased local density of states in metamaterials and show the promise of diffractive gratings to outcouple hyperbolic polaritons to the far-field. Our work should help direct and motivate experiments in the development of single photon sources for broadband emitters such as nitrogen vacancy centers in diamond. The theory and design work shown here was published in [19] while experimental evidence was published in [50].

3.1 Introduction

Nanoscale light-matter interactions can be tailored using plasmonic approaches to have an impact on quantum information processing [96]. It has been conclusively demonstrated that propagating surface plasmon polaritons (SPPs) can possess non-classical properties such as entanglement [97] and squeezing [98]. Furthermore, inspite of the decoherence expected from losses and electron collisions, these properties are preserved during propagation and are manifested in the outcoupled photons [99]. Thus SPPs could potentially be used as a carrier of quantum information at the nanoscale [45, 100].

One important application where plasmonics can play a key role is in the development of room temperature single photon sources [20,27]. The broadband nature of many quantum emitters such as nitrogen vacancy (NV) centers in diamond make them unsuitable for conventional resonant cavity based approaches [101]. The high index of diamond leads to total internal reflection of photons and a poor collection efficiency (4 %) [21]. Therefore, the use of nanoplasmonic structures capable of a broadband Purcell effect is necessary for efficient extraction of single photons [22,102]. Plasmonic

metamaterials which engineer the spontaneous emission can also be used to enhance the absorption spectrum of the isolated emitter [103].

However, a significant limitation of any plasmonic approach is the presence of loss and non-radiative quenching [104]. Especially near the plasmon resonance, only a modest increase in quantum efficiency and collection efficiency is possible [105]. The key is to move away from resonant approaches and focus on low mode volume plasmons. The figures of merit for single photon sources are the collection efficiency, directional spontaneous emission and Purcell effect [23, 24, 28]. Deterministic out-coupling of single photons and tolerance to emitter positioning is another important factor affecting device performance [26].

Below, we show that tailored plasmonic metamaterials support collective modes which can efficiently channel single photons from an isolated quantum emitter to highly directional beams and simultaneously provide a broadband Purcell effect. Our design for the single photon source, compatible with emitters such as NV centers in diamond, takes into account all non-idealities in the structure arising from the finite patterning scale, absorption and dispersion. We also provide a detailed account of quenching and function away from resonance to achieve an efficient single photon source inspite of the losses.

3.2 Quantum Resonance Cones

Our approach relies on engineering the plasmonic Bloch modes of periodic metal-dielectric structures. Such 1D (multilayer) or 2D (nanowire) plasmonic crystals can behave as an effective metamaterial when the lattice spacing is far below the operating wavelength [52, 68, 106]. We consider a 1D multilayer metal-dielectric lattice as shown in Fig.3.1a. The short range propagating surface plasmon polaritons on each metal-dielectric interface couple, leading to Bloch modes with unique properties not available in conventional photonic crystals. They are described by effective medium theory (EMT) in the metamaterial limit by a homogeneous medium that has

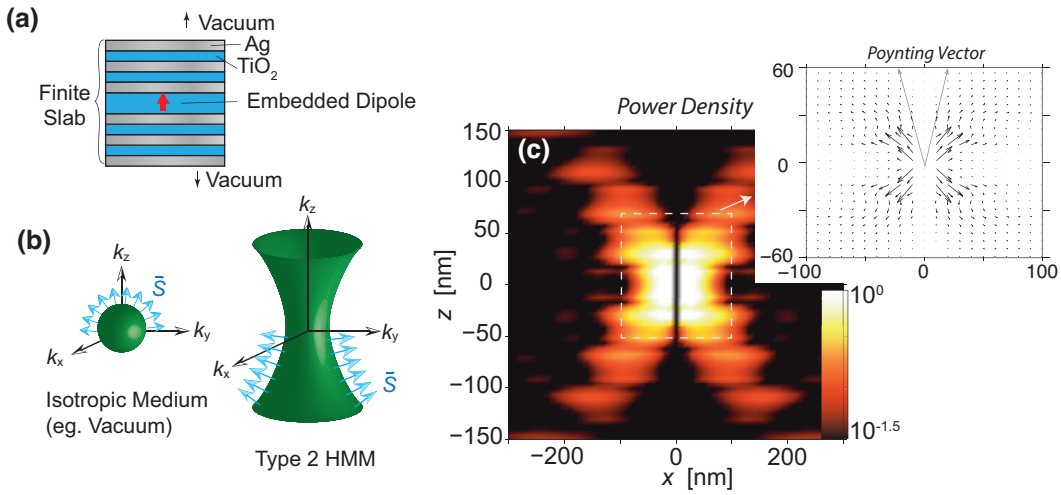

Fig. 3.1. (a) A multilayer stack of Ag/TiO_2 with 10/30 nm layer thicknesses behaves like a homogeneous metamaterial slab with hyperbolic dispersion ($\epsilon_{\|} < 0, \epsilon_{\perp} > 0$) above $\lambda \approx 720$ nm. The emitter is embedded symmetrically in a 30 nm layer of TiO_2. (b) The direction of power flow is normal to the isofrequency surface. In HMMs, the power flow of all high-k states tends to *bunch* and point in the same direction, thus forming resonance cones. (c) A quantum dot embedded in a HMM emits preferentially into high-k states and hence the resonance cone ($\lambda = 800$ nm). The Power Density and Poynting Vector are are normalized by the total time averaged power emitted from the oscillating point dipole. The grey arrows show the asymptotic direction of power flow for extremely high-k states for an ideal HMM.

a metallic dispersion along one direction but a dielectric dispersion in the perpendicular direction.

The multilayer structure behaves as an effective metamaterial slab with an extremely anisotropic dielectric tensor $\bar{\bar{\epsilon}} = \mathrm{diag}[\epsilon_{\|}, \epsilon_{\|}, \epsilon_{\perp}]$, where the directions are parallel and perpendicular to the above mentioned layers. Extraordinary plane wave propagation in uniaxial anisotropic media is governed by the dispersion relation

$$k_x^2/\epsilon_{\perp} + k_z^2/\epsilon_{\|} = (\omega/c)^2 \,. \tag{3.1}$$

which describes an open hyperboloid (Fig.3.1(b)) when $\epsilon_{\|}\epsilon_{\perp} < 0$. These artificial media are known as hyperbolic metamaterials (HMM) [107]. They have the property of large momentum bulk propagating waves (high-k modes with unbounded magni-

tudes of k_x and k_z) which arises due to surface-plasmon-polariton Bloch waves in the plasmonic crystal. For ordinary materials such as glass with $\epsilon_{\|}\epsilon_{\perp} > 0$, the dispersion relation describes a bounded sphere and the magnitudes of k_x and k_z have an upper cut-off. Above this cut-off, waves are evanescent and simply decay away.

The Poynting vector in a medium is related to the normal vector to the dispersion relation (blue arrows in Fig.3.1(b)). The Poynting vector, given by $\overrightarrow{S} = k_x/(k_0\epsilon_{\perp})\hat{x} + k_z/(\epsilon_{\|}k_0)\hat{z}$, where k_x and k_z are related by the dispersion relation, eq. 3.1, lie within a narrow region known as the resonance cone. Thus energy flow due to the bulk plasmonic Bloch modes in this metamaterial is inherently directional. The half angle of the plasmonic resonance cone is given by [108]

$$\tan\theta_{RC} = \sqrt{-\frac{\epsilon_{\|}}{\epsilon_{\perp}}}. \tag{3.2}$$

Furthermore, for all the waves in the medium with wavevectors along the asymptotes of the hyperbola, the Poynting vectors point in the same direction. Since there are infinitely many waves (in the EMT limit) with wavevectors along the asymptotes of the hyperbola, a spatial crowding of Poynting vectors is expected in preferred directions (Fig.3.1(b)). This phenomenon has been observed in anisotropic plasmas [108, 109] and emulated in microwave metamaterial circuits [110]. Here, we consider the plasmonic equivalent of resonance cone behavior at optical frequencies. Below, and in the following sections we show that spontaneous emission from an isolated emitter is enhanced and directed into sub-diffraction resonance cones. The enhanced emission can lead to single photon resonance cones which propagate 100's of nm, thus allowing the study of non-classical light propagation in metamaterials and opening the route to quantum applications.

We consider the case of an emitter such as a quantum dot or dye molecule with a dipole transition, placed within the practical multilayer metal-dielectric metamaterial. Preferential emission into the resonance cone is observed for a dipole emitter placed within a 30 nm TiO_2 layer surrounded on top and bottom by alternating layers of silver and TiO_2. The thickness of the silver layer and TiO_2 layers are 10 nm and 30 nm respectively. There are 5 Ag layers and 4 TiO_2 layers on each side of

the embedded layer. The resonane cone phenomenon is due to the combination of three effects: a) strong overlap of the plasmonic Bloch modes with the emitter b) presence of a large number of such modes and c) subwavelength confinement of the emitter. The resonance cone emission in the finite multilayer realization matches quite closely with the high-k limit predicted by effective medium theory for an ideal hyperbolic metamaterial. The Poynting vector is non-zero only outside the resonance cone ($\theta \geq \theta_{RC}$) and energy tends to flow along the surface of the resonance cone $\theta \approx \theta_{RC}$ (Fig.3.1(c)inset)

3.3 Decay Rate Enhancement

Along with the directional nature of radiation, we show that a large Purcell factor in a broadband range is possible especially when the emitter is embedded inside the metal-dielectric multilayer structure. The plasmonic Bloch modes of the multilayer structure have a higher momentum than conventional SPPs even away from resonance. This leads to broadband enhancement in the local density of states and these modes are a new radiative decay channel for embedded dye molecules or quantum dots [17, 18, 100, 111]. This initial research into hyperbolic metamaterials has shown their potential for radiative decay engineering and here we consider the transmission of these modes for applications such as single photon sources. We use a Green's function formalism [4] and define the local density of states (LDOS) within a practical multilayer structure taking into account non-idealities such as loss and dispersion. A large increase in the LDOS at the location of the emitter is observed which results in a large decay rate enhancement due to Fermi's Golden Rule [104].

Figure 3.2(a) shows the large total decay rate enhancement $\beta = \Gamma/\Gamma_0$ of an emitter embedded in a Ag/TiO_2 multilayer slab across the region of hyperbolic dispersion ($\lambda > 720$ nm) (Γ_0 is the decay rate in a homogeneous slab of TiO_2). The Green's tensor calculation of β shows extremely good agreement with the full wave FDTD calculation. The monotonically increasing behaviour of $\beta(\lambda)$ is explained by noting

that the coupling strength between the emitter and the HMM modes increases at shorter interaction distances, d/λ. In figure 3.2(a) d is fixed, however as λ increases the interaction distance decreases; furthermore, material dispersion plays a strong role in the exact nature of the $\beta(\lambda)$ scaling. In sections 3.4 and 3.5 we elucidate a semi-analytic Green's Function technique for calculating the local density of states and predicting the dominant decay channels of the emitter. We shows that the dominant decay channels are plasmonic bloch and gap modes. Thus emission is not quenched and the large total decay rate enhancement shown in figure 3.2 can be utilized for single photon sources.

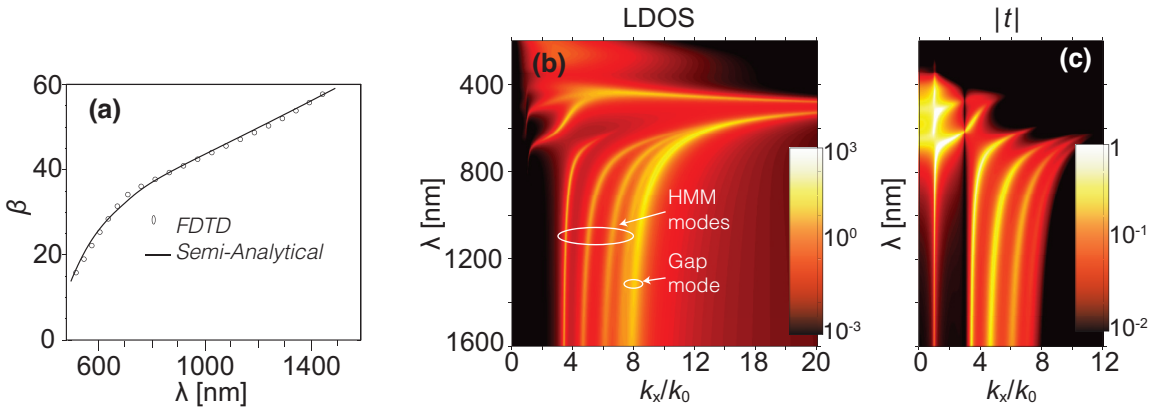

Fig. 3.2. (a) A large decay rate enhancement is predicted across the region of hyperbolic dispersion. (b)The W-LDOS (normalized by vacuum) available to a quantum emitter embedded in a multilayer realization of a HMM show that emission occurs into bulk waveguide modes of the HMM slab in the region of hyperbolic dispersion. (c) The transmission coefficient (computed using a transfer matrix method for a plane wave launched from the embedded layer) at the top of the multilayer slab shows that the HMM waveguide modes propagate to the top of the HMM slab and can be outcoupled.

3.4 Local Density of States

This enhanced spontaneous emission is channeled to multiple modes all of which carry energy along the above mentioned resonance cones. We therefore analyze the modal distribution of the spontaneously emitted radiation by defining the wavevector resolved local density of states (W-LDOS) [112]. This separates the density of states available to the emitter within the multilayer structure according to the modes characterized by the wavevector parallel to the layers (k_x).

Figure 3.2(b) shows the enhanced W-LDOS available to a single emitter embedded in a 30 nm thick layer of TiO_2 clad by realistic finite slabs of Ag/TiO_2 multilayer HMM (see figure 3.1(a)). We identify the series of bright vertical bands as high-k HMM waveguide modes that arise from coupled surface-plasmon-polaritons, and identify the last bright line as the gap mode. When the embedded layer thickness is kept above ≈ 30 nm, emission into the high-k modes of the HMM and hence resonance cones dominates the total decay enhancement β. When the embedded layer is smaller, emission into the gap plasmon mode and emission quenching begins to dominate the total decay enhancement β.

Two severe limitations on plasmonic approaches in general are the finite absorption length in the structure and non-radiative quenching. To study the propagation length of high-k modes in the hyperbolic metamaterial we plot the transfer function of a practical structure. Figure 3.2(c) shows the transmission coefficient at the top of the multilayer HMM slab, and shows that the high-k HMM waveguide modes propagate a distance of $L \approx 170$ nm to the edge of the slab, and therefore can indeed be out coupled. A detailed account of non-radiative decay and quenching is provided later in this chapter. We note that functioning away from resonance and optimizing the embedded layer thickness can lead to a large fraction of spontaneous emission directed into the high-k modes and hence resonance cones.

We emphasize that single photon sources based on the HMM high-k modes are fundamentally different than those based on MIM plasmonic modes [113, 114], slow

light modes [115], localized plasmons [25,29] and slot waveguide modes [116]. In MIM and slot waveguides, energy flow is along the MIM interfaces; while in HMM systems energy flows through the metal-dielectric multilayers at oblique angles. Furthermore, by examining the band structure in the W-LDOS calculation we observe that the group velocity $v_g = \partial\omega/\partial k$ does not vanish and the HMM waveguide modes are therefore, not slow light modes.

3.5 Green's function technique

In the general quantum mechanical approach, the decay rate of a single emitter is given by

$$\Gamma = \frac{2\omega^2}{\hbar c^2} \left(\vec{\mu} \cdot \mathrm{Im} \left[\bar{\bar{G}}(r_0, r_0, \omega) \right] \left(\vec{\mu} \right) \right) \tag{3.3}$$

where $\bar{\bar{G}}(r_0, r_0, \omega)$ is the Green's tensor of the electromagnetic wave-equation, evaluated at the location of the quantum emitter with dipole moment $\vec{\mu}$.

Here we use the semi-classical approach developed by Ford and Weber [104] which treats the quantum emitter as a radiating point dipole. In the weak coupling limit, the general quantum mechanical approach and the semi-classical approach are equivalent, since the power radiated from an electric point dipole is proportional to $\bar{\bar{G}}(r_0, r_0, \omega)$. Similar to the general quantum mechanical approach, this semi-classical approach employs a Green's function technique to compute the fields and thus the radiated power from a point dipole.

Using this approach, we find for a point dipole with dipole moment $\vec{\mu}$ placed a distance d above (or embedded in) a HMM planar slab, the decay rate enhancement (relative to vacuum) is computed as

$$\beta = \Gamma/\Gamma_0 = (1-\eta) + \eta \ \mathrm{Re} \left[\int_0^\infty \rho(\lambda, d, \vec{k}) \mathrm{d}k_\parallel \right] \left(\tag{3.4}$$

where $k_\parallel$ is the wavevector parallel to the interface of the HMM, and η is the intrinsic quantum yield. Where $\rho(\lambda, d, \vec{k})$ is the local density of states (LDOS) seen by the emitter, normalized by the LDOS of vacuum. The LDOS is computed by taking into

account the various modes of the system which is captured by the angular reflection spectrum.

$$\rho(\omega,d,\vec{k})=\frac{3}{2}\frac{1}{k_1^3}\frac{1}{|\vec{\mu}|^2}\frac{k_x}{k_z}\mathrm{e}^{i2k_zd}\left\{\frac{1}{2}\mu_\parallel^2\left[(1+r^{(s)})k_1^2-(1-r^{(p)})k_z^2\right]+\mu_\perp^2(1+r^{(p)})k_\parallel^2\right\}\left(\right. \tag{3.5}$$

where $r^{(s)}$ and $r^{(p)}$ are the reflection coefficients for s- and p-polarized light respectively. k_1 is the magnitude of the wavevector in the medium where the dipole resides $k_1=\sqrt{\epsilon}(\omega/c)$. Finally k_z is determined from the dispersion relation where the dipole resides $k_z=\sqrt{k_1^2-k_\parallel^2}$.

Peaks in ρ indicate dominant decay channels of the emitter, and as shown below, when the emitter is in the near-field of a HMM slab, ρ is dominated by unique high-k propagating waveguide modes. In the following sections, the interaction distance d dependence of β and ρ for an effective metamaterial and a physical realizable structure are investigated. To help elucidate the dependence on the interaction distance we compute the *effective power dependence*

$$n=\frac{\mathrm{d}\log\beta}{\mathrm{d}\log d} \tag{3.6}$$

which approximately gives $\beta\sim d^n$.

3.5.1 $\beta(d)$ for Effective HMM Slabs

In this section, we treat the HMMs using effective medium theory. The systems studied are shown schematically in figure 3.3a,b. To compute the reflection coefficients required to calculate β and ρ for each of these two geometries, the fresnel reflection coefficients for plane waves incident on a finite slab are used.

In the case of a dipole placed above the HMM slab the reflection coefficients are

$$r^{(s,p)}=\frac{r_{1,2}^{(s,p)}+r_{2,3}^{(s,p)}\mathrm{e}^{j2k_{2,z}t}}{1+r_{1,2}^{(s,p)}r_{2,3}^{(s,p)}\mathrm{e}^{j2k_{2,z}t}} \tag{3.7}$$

where t is the thickness of the HMM slab and $r_{i,j}^{(s,p)}$ are the fresnel reflection coefficients for a single interface, and $k_{2,z}=\sqrt{\epsilon_\parallel(k_0^2-k_\parallel^2/\epsilon_\perp)}$.

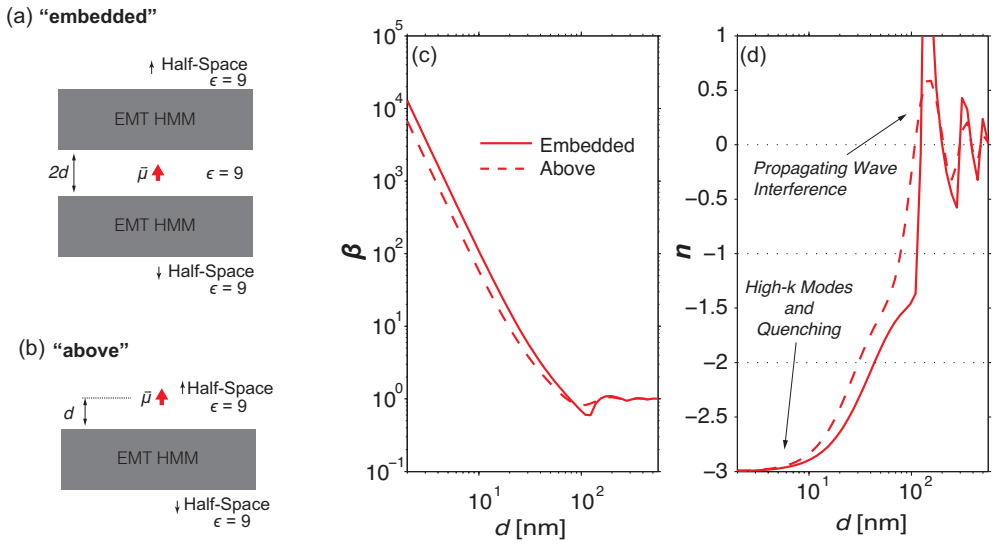

Fig. 3.3. (a) A dipole is embedded symmetrically between two 370 nm thick HMM slabs composed of Ag/TiO_2 with a silver filling fraction of 0.25. Type 2 hyperbolic dispersion is predicted above $\lambda \sim 720$ nm. The embedded layer thickness is varied. (b) A dipole is placed above one of the finite HMM slabs from ())a. The dipole/interface distance is varied. (c) Calculated enhanced decay rate β at $\lambda = 900$ nm show that the decay rate enhancement is stronger when the dipole is embedded between two HMMs. (d) In the extreme near-field, the decay rate enhancement varies as the inverse cube of the interaction distance which is attributed to emission into high-k HMM modes and quenching. At far-field interaction distances, the decay rate enhancement is governed by plane wave interference effects.

For the case of a dipole embedded between two finite HMM slabs the reflection coefficients are computed using plane wave reflection coefficients in the *tunnel junction geometry* which can found in [104].

The calculated β and n are shown in figure 3.3c,d for a *vertically oriented dipole* at a wavelength of $\lambda = 900$ nm and for 370 nm thick metamaterial slabs consisting of Ag/TiO_2 with a metal filling fraction of 0.25. Realistic loss and dispersion were used for the effective medium computation [117,118]. The metamaterial is predicted to be type 2 ($\epsilon_{\parallel} < 0$, $\epsilon_{\perp} > 0$) above $\lambda \sim 720$ nm; the predicted permittivity dispersion of this structure are shown in figure 3.8a. At $\lambda = 900$ nm, the dielectric response of the

parallel and perpedicular compenent of the dielectric tensor are $\epsilon_{\|} = -4.3 + i0.4$ and $\epsilon_{\perp} = 11.0 + i0.07$

Due to confinement effects, the embedded dipole has a larger enhanced decay rate than the dipole simply above the effective medium HMM slab. Furthermore, in the limit of the dipole located very close to the HMM interface(s) $d << \lambda/\sqrt{\epsilon}$, the decay rate enhancement is proportional to the inverse cube of the interaction distance $\beta \sim d^{-3}$. This extreme near-field behaviour is attributed to emission into the unique high-k modes of the HMM and emission into lossy surface waves (quenching) which is discussed in more detail in the following sections. For large interaction distances where $d \sim \lambda/\sqrt{\epsilon}$, plane wave interference/field intensity effects govern the decay rate enhancement; this is discussed in more detail in the following sections.

3.5.2 $\beta(d)$ for Practical Realization of HMMs: Multilayer Slabs

In this section, we treat the HMMs using a physical realizable multilayer structure. The systems studied are shown schematically in figure 3.4a,b. To compute the reflection coefficients required to calculate β and ρ, a transfer matrix method is used.

We first consider the case of a dipole placed above a N-layer stack with the i^{th} layer having a dielectric constant ϵ_i and a thickness t_i. The reflection coefficient $r^{(s,p)}$ can be found by solving the matrix equation at each incident k_x

$$\begin{bmatrix} 1 \\ r^{s,p} \end{bmatrix} = (D_0^{(s,p)})^{-1} T^{(s,p)} D_{N+1}^{(s,p)} \begin{bmatrix} t^{(s,p)} \\ 0 \end{bmatrix} \tag{3.8}$$

where $T^{(s,p)}$ is the transfer matrix product

$$T^{(s,p)} = \prod_{i=1}^{N} D_i^{(s,p)} P_i (D_i^{(s,p)})^{-1} \tag{3.9}$$

with the individual propagation and interface matrices for the i^{th} layer defined as

$$D_i^{(p)} = \begin{bmatrix} 1 & 1 \\ \frac{k_z^i}{\epsilon_i} & -\frac{k_z^i}{\epsilon_i} \end{bmatrix}$$

$$D_i^{(s)} = \begin{bmatrix} 1 & 1 \\ k_z^i & -k_z^i \end{bmatrix}$$

$$P_i = \begin{bmatrix} e^{-jk_z^i t_i} & 0 \\ 0 & e^{jk_z^i t_i} \end{bmatrix}$$

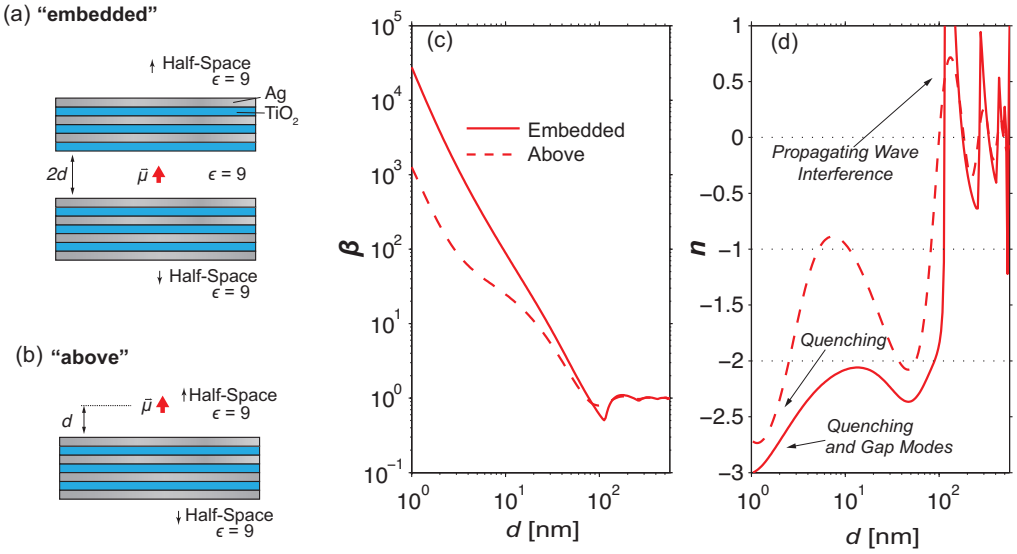

Fig. 3.4. (a) A dipole with vertical dipole moment is embedded symmetrically between two 4.5 period multilayer HMM slabs composed of Ag/TiO_2 with thicknesses 10/30 nm respectively. Type 2 hyperbolic dispersion is predicted above $\lambda \sim 720$ nm. The embedded layer thickness is varied. (b) A dipole is placed above one of the finite HMM slabs from (a). The dipole/interface distance is varied. (c) Calculated enhanced decay rate β calculations at $\lambda = 900$ nm show that the decay rate enhancement is considerably stronger when the dipole is embedded between two multilayer HMMs. (d) In the extreme near-field, the decay rate enhancement varies as the inverse cube of the interaction distance; this is attributed to (i) emission into a gap plasmon mode and quenching when the emitter is embedded and (ii) emission quenching when the emitter is placed above the multilayer. At far-field interaction distances, the decay rate enhancement is governed by propagating wave interference effects.

This transfer matrix method is generalized in the tunnel junction geometry, where the dipole is embedded between two multilayer stacks.

The calculated β and n are shown in figure 3.4c,d at a wavelength of $\lambda = 900$ nm and a 4.5 period Ag/TiO_2 multilayer with thicknesses 10/30 nm respectively. Realistic loss and dispersion were used for the calculations [117,118]. At $\lambda = 900$ nm, TiO_2 is lossless and the loss in the structure is due to silver which has $\epsilon_{Ag} \approx -40+i1.7$ The metamaterial is predicted to be type 2 ($\epsilon_{\parallel} < 0$, $\epsilon_{\perp} > 0$) at this wavelength; the predicted effective medium dispersion of this structure can be in figure 3.8a, later in this chapter.

We observe that in general, the embedded dipole has a larger enhanced decay rate than the dipole simply above the multilayer. For large interaction distances where $d \sim \lambda/\sqrt{\epsilon}$, plane wave interference/field intensity effects govern the decay rate enhancement; this is observed in the low-k LDOS shown following sections. In the limit of the dipole located extremely close to the HMM interface $d << \lambda/\sqrt{\epsilon}$, the behaviour of the dipole located above the multilayer and the dipole embedded between the multilayers is different: there are different modes available for dipole to decay into in each geometry. This is elucidated through the high-k LDOS discussed in the following sections.

3.6 Quenching

The wave vector resolved density of states $\rho(\omega, d, \vec{k})$ provides insight into the dominate decay channels of the emitter and helps explain the dependence of β on the interaction distance. Here we show the preferred decay channels of a dipole at various distances from an effective medium HMM and a physically realizable multilayer HMM.

3.6.1 Far-Field Interference: Low-k Interactions

Figure 3.5 shows the calculated low-k LDOS for the four geometries considered in the previous two sections. We see distinct peaks in the LDOS attributed to propagat-

ing wave interference effects. When the waves interfere constructively at the location of the emitter, there is an enhancement in the electric field intensity, and thus an enhancement in the decay rate of the emitter. In the embedded case, the propagating wave interference is due in Fabry-Perot modes. Purely dielectric microresonators used to enhance spontaneous emission utilize these low-k modes.

As the dipole is brought closer to (embedded layer shrunk), the k-space location of the emission enhancement is shifted from low-k modes to high-k modes. For interaction distances smaller than approximately half the wavelength in the medium $\lambda \leq 1/2\ \lambda/\sqrt{\epsilon} \sim 150$ nm near-field interactions begin to dominate, and emission into low-k modes no longer takes place.

3.6.2 EMT Near-Field Modes: High-k Interactions

When the dipole is located at near-field distances, emission directed into the high-k modes of HMM slab. In the effective medium limit there is no upper cut-off on the allowed wave vectors, and as the dipole is brought closer to (embedded layer shrunk), extremely larger wave vector modes become available to the emitter. At very small distance $d/(\lambda/\sqrt{\epsilon}) \ll 1$ emission into these infinite amount of high-k propagating modes of the HMM contribute to the enhanced total decay rate as the inverse cube of the interaction distance $\beta \sim 1/d^3$ [100]. However, there is a competing decay channel, namely quenching. If the emitter is brought extremely close to the interface then emission into lossy surface waves begins to dominate the emission into high-k HMM modes, thus β is mainly due to non-radiative decay. This is demonstrated in figure 3.6 which shows the wave vector resolved local density of states $\rho(\omega, d, \vec{k})$ for a perpendicular oriented dipole placed above a HMM slab and embedded between two HMM slabs. The geometry is the same as that used in figure 3.3. As the emitter is brought closer to the HMM slab (embedded layer shrunk) larger and larger high-k propagating modes appear to the emitter. These modes are interpreted as confined waveguide modes of the HMM slab. In the LDOS, these modes are manifested as

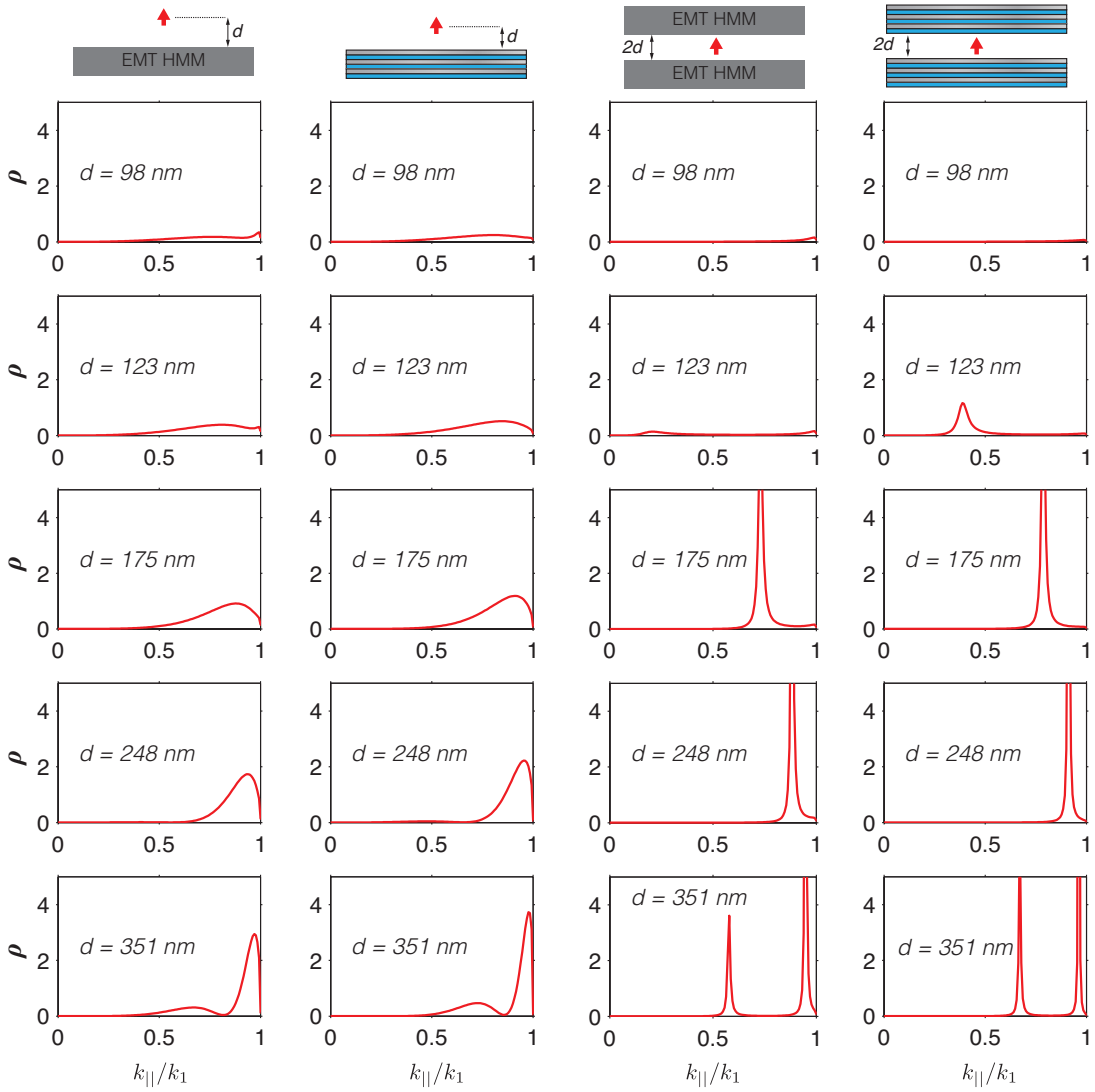

Fig. 3.5. Low-k LDOS: Calculated wave vector resolved LDOS at various far-field interaction distances at $\lambda = 900$ nm show that when $d \geq 1/2\ \lambda/\sqrt{\epsilon} \sim 150$ nm, low-k interactions dominate. As the dipole is brought closer (embedded layer shrunk), emission is shifted into high-k modes. The peaks in the low-k LDOS are due to propagating wave interference.

distinct, relatively narrow peaks. When the emitter is at extreme near-field distances quenching begins to dominate the total decay enhancement β. Quenching (emission into lossy surface waves) appears as a broad peak in the LDOS.

By separating the LDOS integral which determines the decay rate enhancement (equation 3.4) into the two dominant decay channels, the decay rate enhancement due to the HMM waveguide modes (HMM) and the lossy surface waves (LSW) can be estimated from

$$\begin{aligned} \beta &= \beta_{HMM} + \quad \beta_{LSW} && (3.10) \\ &\sim \iint_{\text{HMM}} \rho(\lambda, d, \vec{k}) \mathrm{d}k_{\|} + \iint_{\text{LSF}} \rho(\lambda, d, \vec{k}) \mathrm{d}k_{\|} && (3.11) \end{aligned}$$

By examining equation 3.11 and figure 3.6, we then conclude, at optical wavelengths and at intermediate near-field distance $d \sim 5 - 20$ nm, emission into high-k HMM waveguide modes, and hence resonance cones dominates in the EMT limit. For interaction distances of $d < 5$ nm, the emission is quenched, and the decay enhancement is largely unusable.

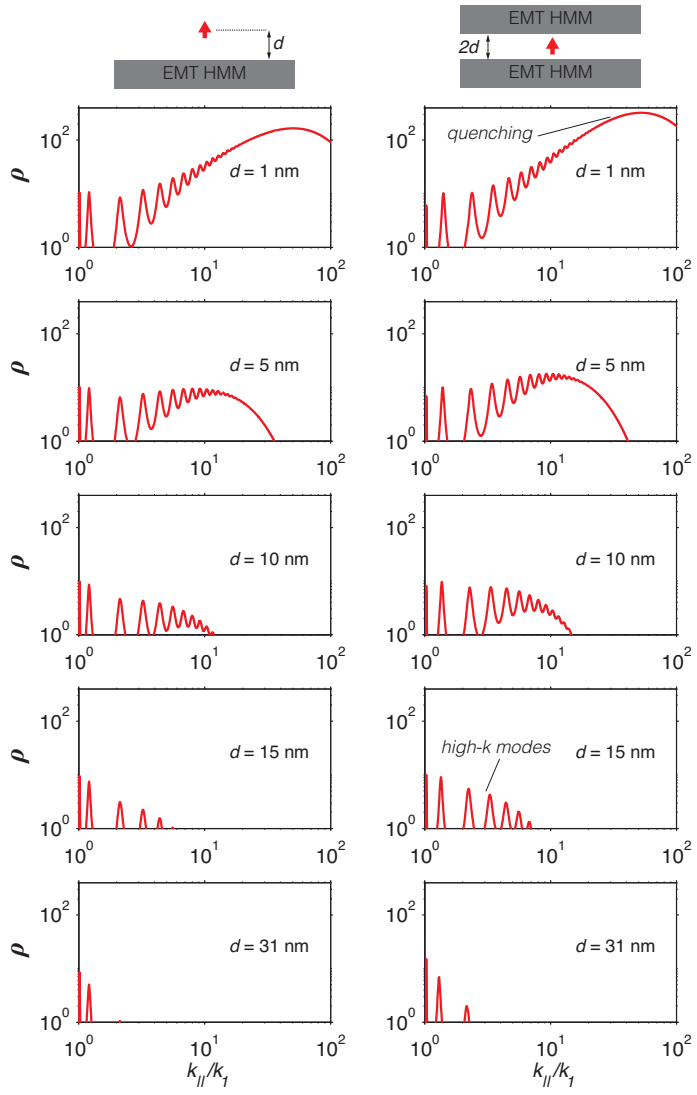

Fig. 3.6. High-k LDOS - Effective Medium Theory: Calculated wave vector resolved LDOS at various near-field interaction distances at $\lambda = 900$ nm show that as the interaction distance d is decreased, additional high-k modes become accessible to the emitter. The HMM modes are recognizable as sharp peaks in ρ and are attributed to propagating waveguide modes of the HMM. When the emitter is embedded between two HMM slabs the coupling to high-k HMM modes is slightly stronger and the onset of the strong near-field interactions occurs at larger d. At very small d, emission quenching begins to dominate. This is recognized as the wide smooth peak in ρ. Emission into the high-k HMM modes and emission quenching cause the total decay rate enhancement β to scale as $\sim d^{-3}$ in the extreme near-field.

3.6.3 Multilayer Realization Near-Field Modes: High-k Interactions

In the effective medium limit there is no upper cut-off on the transverse wave vector allowed by the medium. In a physical realizable system, the maximum transverse wave vector $k_{\|}$ that can be supported is inversely proportional to the unit cell size $1/a$. As a result, there is finite number high-k modes supported by the multilayer HMM structure and thus high-k modes will have a limited effect on the β dependence on d in the extreme near-field. This is demonstrated in figure 3.7 which shows the LDOS dependence on the interaction distances d for the *above* and *embedded* multilayer geometries shown in figure 3.4.

As the emitter is brought closer the multilayer slab (embedded layer shrunk), additional high-k modes of the HMM appear to the emitter. We observe the presence of the *finite period cut-off*, above which no high-k HMM waveguide modes are present. The onset of quenching (broad smooth peak in LDOS) occurs at much closer distances in the physical multilayer system than in the EMT approximation (compare figures 3.6 and 3.7). In the case of an emitter embedded between two multilayer HMMs, we see the presence of a gap plasmon mode (metal-insulator-metal plasmon mode) when the embedded layer thickness (gap) is smaller than about 15 nm. The gap mode can identified by a large sharp peak in the LDOS.

Similar to above, the LDOS integral which determines the decay rate enhancement β (equation 3.4) is separated into the three dominant decay channels: high-k bloch plasmon modes (HMM), the gap plasmon mode (GPM), and lossy surface waves (LSW). The decay rate enhancement from each can then be determined from

$$\beta = \beta_{HMM} + \beta_{GPM} + \beta_{LSW} \tag{3.12}$$

$$\sim \int_{\text{HMM}} \rho(\lambda, d, \vec{k})\mathrm{d}k_{\|} + \int_{\text{GPM}} \rho(\lambda, d, \vec{k})\mathrm{d}k_{\|} + \int_{\text{LSW}} \rho(\lambda, d, \vec{k})\mathrm{d}k_{\|} \tag{3.13}$$

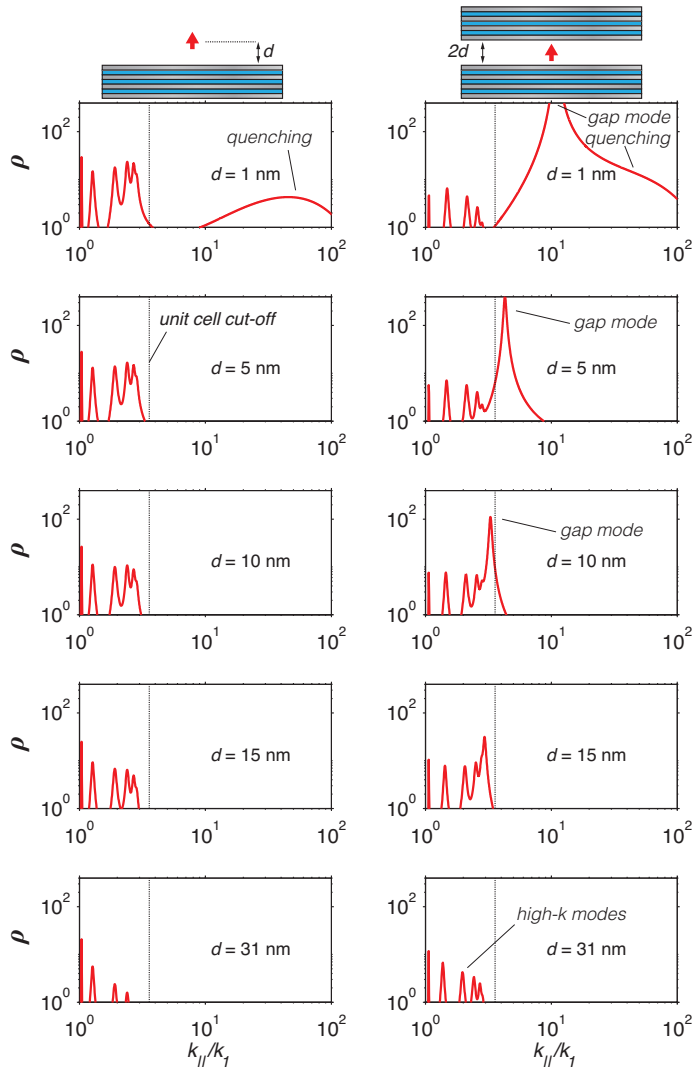

Fig. 3.7. High-k LDOS - Multilayer System:Calculated wave vector resolved LDOS at various interaction distances at $\lambda = 900$ nm show that as the interaction distance d is decreased, additional high-k modes become accessible to the emitter. No high-k HMM modes exist above the cut-off (dashed line). In the case of the emitter above the multilayer slab the onset of emission into lossy surface waves (smooth broad peak) occurs at much smaller distances than in the EMT case. In the embedded case we see the presence of a gap plasmon mode, identified by the large peak which shifts with embedded layer thickness. Again, the onset emission into lossy surface waves occurs at smaller distances than in the EMT case.

Utilizing equation 3.13 and figure 3.7 we conclude that at optical wavelengths and at intermediate near-field interaction distances of $d \sim 10 - 20$ nm, the first term (HMM) in equation 3.13 is much greater than the other two contributions, and thus emission into the finite number of high-k HMM modes dominates the total decay enhancement β. These high-k modes contribute to emission into highly directive resonance cones. By moving the emitter closer to the multilayer HMM, emission into the gap mode and quenching begins to dominate the total decay enhancement. However, in contrast to the EMT case, when the emitter is embedded in an extremely small layer, emission into the gap plasmon mode dominates, not quenching, the other decay channels. This result is in agreement with [113]. The gap plasmon mode does not contribute to emission into resonance cones.

3.7 Topological transition assisted pumping scheme

We now address the critical challenge of pumping embedded emitters in metamaterials. Quite often the large impedance mismatch with vacuum leads to inefficient coupling of radiation to emitters placed inside such structures. We design our metamaterial to have a transparency window at the pumping wavelength and a large density of states (plasmonic response) only in the wavelength of emission.

Figure 3.8(a) shows the effective medium dielectric response of the Ag/TiO_2 multilayer. Below $\lambda_{OTT} \approx 720$ nm the multilayer slab is effectively a dielectric ($\epsilon_{\parallel} > 0, \epsilon_{\perp} > 0$) and transparent to normal incident light. Above $\lambda_{OTT} \approx 720$ nm the multilayer slab is a type 2 HMM ($\epsilon_{\parallel} > 0, \epsilon_{\perp} < 0$), where enormous increase in the LDOS yields large decay rate enhancement β into high-k modes of the HMM. This significantly different behaviour is attributed to an optical topological transition (OTT) in the iso-frequency (k-space) surface from a closed ellipsoid to an open hyperboloid at $\lambda_{OTT} \approx 720$ nm which drastically changes the decay channels available to the emitter (see Eq.3.1) [119]. The difference in the electromagnetic responses above and below the topological transition allows for a novel realistic pumping scheme: a

single emitter can be pumped where the HMM is transparent, and in turn have its lower energy emission enhanced and extracted in the type 2 hyperbolic dispersion region.

To understand the nature of spontaneously emitted radiation we consider the case of a high index superstrate ($\epsilon >> 1$) and define the Purcell factor using only propagating waves that reach the far-field. As expected, without the superstrate all the modes are confined to the structure and do not out couple to the far-field. However a very interesting transitional behavior is seen in the far-field with the high index superstrate. Figure 3.8b shows the predicted far-field Purcell factor F_p of the emitter inside a practical metal-dielectric multilayer with a high-index superstrate ($\epsilon \approx 30$). Enhanced spontaneous emission reaches the far-field of the superstrate and there is a large increase in the Purcell factor exactly at the transition wavelength predicted by effective medium theory (λ_{OTT}). Note the broad bandwidth in which this Purcell factor occurs.

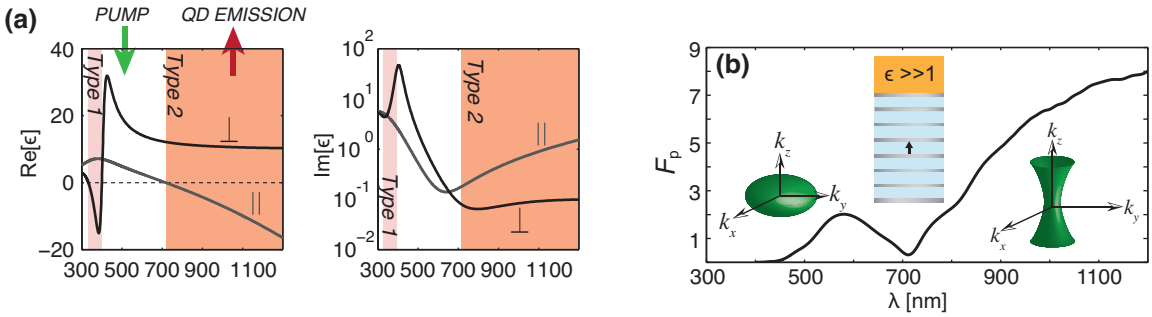

Fig. 3.8. (a) Parallel and perpendicular components of the dielectric permittivity predicted by EMT for a 10 nm and 30 nm Ag/TiO_2 multilayer structure. A topological transition between elliptical dispersion and hyperbolic dispersion occurs just above $\lambda_{OTT} \approx 720$ nm. (b) Using a large dielectric constant half-space superstrate ($\epsilon >> 1$), the high-k modes of the resonance cones are outcoupled into well defined propagating modes in the far-field of the dielectric over a broadband spectral range. There is excellent agreement between the topological transition predicted by EMT and the large Purcell factor achieved in the practical multilayer structure.

3.8 Outcoupling

We now address the outcoupling of high-k modes which has been the significant limiting factor for all applications of hyperbolic metamaterials [18, 119]. Given the cylindrical symmetry of the dipole/multilayer system, we propose a Bullseye grating structure [120] to out couple the resonance cone to vacuum. Figure 3.9a shows the proposed bullseye structure etched into an 85 nm TiO_2 layer on top of the Ag/TiO_2 HMM structure. Figure 3.9b shows that the far-field Purcell factor can exceed 6, and the spectral location of the maximum F_p can be tuned by varying the Bullseye grating period Λ. It is worth emphasizing that the colour selective out coupling by the grating is a resonant phenomenon [121], however the magnitude of the F_p is due to the decay rate enhancement into the high-k HMM modes (resonance cones), which is fundamentally non-resonant and broadband.

Since the quantum emitter couples into specific metamaterial modes with a unique lateral wave vector k_x (figure 3.2a), the Bullseye grating scatters these modes into well defined free space modes. The directivity D gives a measure of the enhanced directivity of a given emission pattern relative to an isotropic point source; it is defined as $D(\theta) = P(\theta)/(P_{rad}/4\pi)$ where $P(\theta)$ is the power density at a given far-field angle θ and $P_{rad}/4\pi$ is the total power radiated into the far-field averaged over all solid angles. Figure 3.9(c) shows the directivity on a linear scale for a grating period of $\Lambda = 400$ nm at the wavelength of maximum far-field Purcell factor $\lambda \approx 900$ nm. We see that the Bullseye scatters the resonance cone into a highly directive well defined spatial mode: a thin conical shell with a half angle of $\theta \approx 34^o$.

In this investigation, we have considered a single period Bullseye grating which can be used to outcouple a single wavelength despite the fact that the HMM structure provides a spectrally broad decay rate enhancement. In high-Q microcavities large decay rate enhancements and outcoupling occur at the same resonant wavelength with far-field Purcell factors that can far exceed the values demonstrated here. This process is fundamentally narrow band and therefore not suitable for broadband single

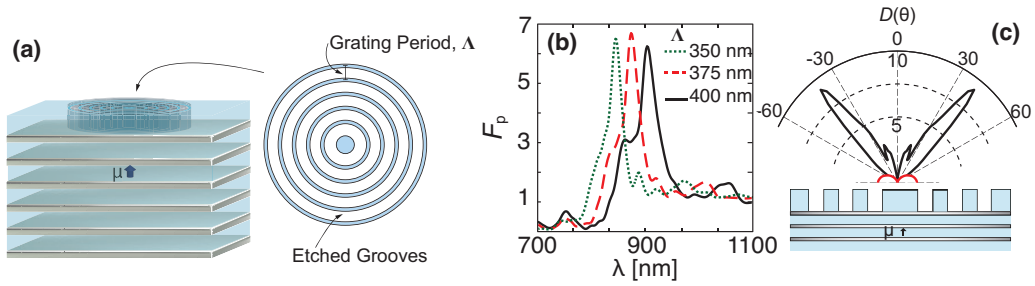

Fig. 3.9. HMM-based single photon source utilizing a bullseye grating to outcouple single photon resonance cones from the metmaterial. (a) A subwavelength cylindrical *Bullseye* grating can be used to scatter the high-k states which are intrinsically confined to the HMM slab, into vacuum propagating modes. (b) FDTD simulations show that the spectral location of the maximum far-field Purcell factor F_p can be tuned by varying the grating period. (c) The directivity $D = P(\theta)/(P_{tot}/4\pi)$ is shown at the location of maximum far-field enhancement ($\Lambda = 400$ nm; $\lambda_{max} \approx 900$ nm). The emission from the bullseye occurs into a highly directive conical shell. The small grey curve shows the directivity of a dipole in TiO_2. Directivity is a measure of the power density directed along a particular direction relative to an isotropic point source emitting the same total power.

emitters. Recent work on broadband plasmonic scattering [122,123] has demonstrated that efficient outcoupling of plasmons across the optical spectrum can be achieved with chirped gratings. Therefore with chirped gratings, it may be possible to utilize the broadband decay rate enhancement provided by the HMM, and achieve a broadband far-field Purcell factor. The single-period Bullseye structure described here is a proof of principle showing that decay rate enhancement provided by HMMs may be utilized for far-field single photon sources. Further design of the Bullseye grating and other outcoupling techniques will fully utilize the non-resonant broadband decay rate enhancements provided by HMMs making them far more advantageous than microcavities for applications with broadband emitters. In the next section, we provide an experimental proof of principle for the promise of this device.

3.9 Experimental Proof of Principle

Motivated by the promise of the hyperbolic metamaterial, bullseye grating device for use as a single photon source, we forged a collaboration with Dr. Tal Galfsky and the Prof. Vinod Menon group in the Dept. of Physics at the City University of New York. This section outlines the key results from a proof of principle experiment and the nano fabrication for our device above. We observe that for quantum dot emitters (QDs) embedded within a multilayer HMM, the spontaneous emission lifetime is decreased by about a factor 10 and the addition of a bullseye grating boosts the total fluorescence output to the far-field by a factor of about 20 relative to a blank metamaterial (no grating). We note that these experiments are not yet in the single dipole emitter regime, but in the many dipole emitter limit.

In the design outlined above TiO_2 was used as the dielectric. However, in these experiments we use Al_2O_3 as the dielectric material in the metamaterial unit cell. Ag/Al_2O_3 multilayer metamaterials were fabricated via electron beam evaporation. Figure 3.10(a) shows a schematic of the Ag/Al_2O_3 metamaterial and figure 3.10(b) shows a TEM cross section confirming the key geometrical parameters (Ag thickness $\approx$ 12 nm, Al_2O_3 thickness $\approx$ 20 nm). An ultrathin ($\approx 1-2$ nm) germanium wetting layer was deposited below each Ag film; this allows the fabrication of thinner, smoother Ag films with lower optical losses as described in detail in ref. [124]. Embedded within the metamaterial between a metamaterial unit cell, CdSe/ZnS core-shell QDs were spin-cast as a thin film ($\approx$ 20 nm thick). Figure 3.10(c) shows the effective dielectric tensor of the metamaterial extracted from spectroscopic ellipsometry; from this data type II hyperbolic dispersion is confirmed throughout the spectral bandwidth of the QD fluorescence emission.

Figure 3.10(d) shows the measured fluorescence lifetime of the QDs embedded in HMMs with different total number of total periods (metamaterial unit cells); also shown is the corresponding measurement on glass. The experimental setup is shown in figure 3.11. We observe that the QDs fluorescence lifetime reduces as the total

number of unit cell periods is increased thus confirming the broadband increase in the density of states within hyperbolic media. A 10× decrease in the spontaneous emission lifetime (relative to glass) is inferred for QDs embedded within a seven period metamaterial.

The emission of the QD fluorophores is guided into hyperbolic polariton modes, the so called high-k states; the transverse wavevector of these modes lies outside the light cone of vacuum (and glass) and a grating must be used to scatter (diffract) these modes into vacuum. We now show that a bullseye grating effectively out-couples the high-k states of the metamaterial to the far-field. We fabricate germanium bullseye gratings on top of the multilayer metamaterials via electron beam lithography and lift-off lithography. Figure 3.12 shows an example SEM micrograph of a fabricated bullseye grating on top of the multilayer metamaterial. The left inset shows a low magnification SEM micrograph of different grating periods fabricated adjacent one another on the same sample.

Figure 3.13 shows experimental evidence of the bullseye grating's ability to effectively outcouple the high-k states of the metamaterial. We observe a 20× enhancement in fluorescence emission intensity when the grating period is tuned to $\Delta = 125$ nm. If we take into account the ensemble of random QD dipole moment angular orientations, then FEM *Comsol* simulations accurately model and predict this enhancement.

To conclude, we have experimental proof that HMMs drastically decease (10×) the fluorescence lifetime of quantum dots due to the broadband increase in local density of photonic states inside hyperbolic media. Nanofabricated bullseye gratings on top of the metamaterials show that the high-k states making up the majority of the QD emission are effectively out-coupled to the far-field via diffractive scattering.

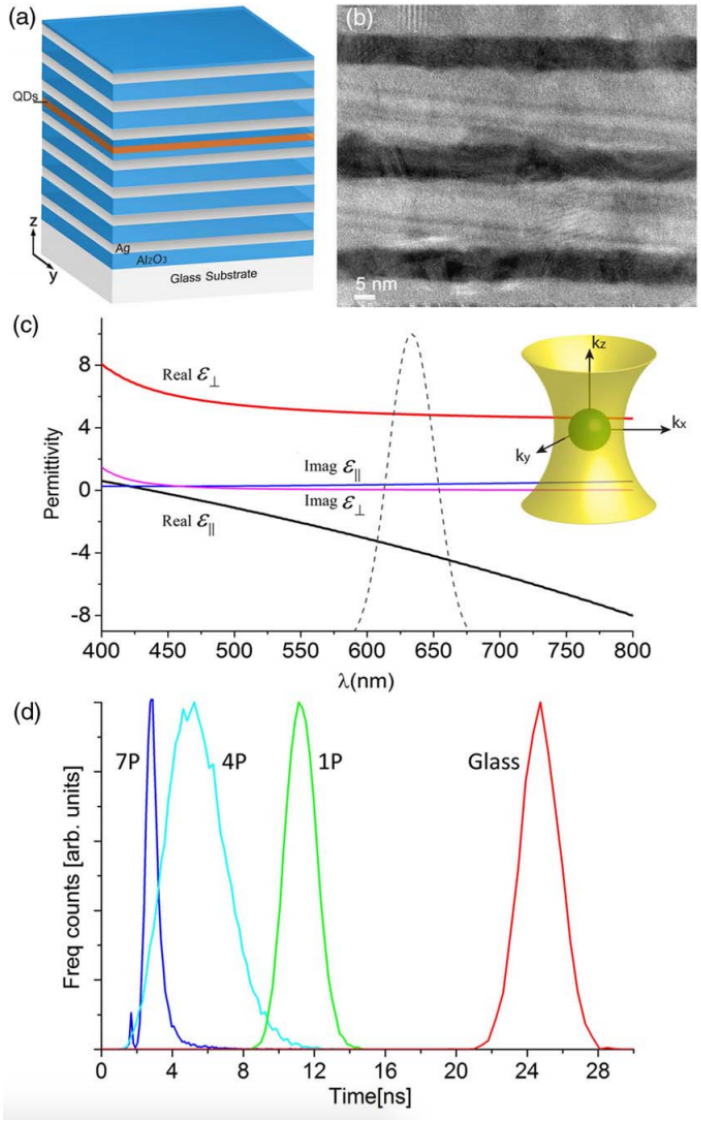

Fig. 3.10. (a) Schematic of the HMM composed of Ag/Al_2O_3. (b) Cross-sectional TEM image showing smooth continuous films of Ag (dark) and Al_2O_3 (bright). (c) Permittivity of the structure as calculated from Effective Medium Theory based on experimentally determined dielectric constants and metal fill fraction. Dotted line corresponds to the emission spectrum of the QDs. Inset, hyperbolic isofrequency contour of an ideal HMM overlaid on the spherical IFC of air. (d) Lifetime distribution of QDs on glass, 1-period, 4-period, and inside a 7-period nonpatterned HMM. Experiment credit goes to Dr. Tal Galfsky and Prof. Vinod Menon of the City University of New York. Figure reprinted with permission from ref. [50], Optical Society of America.

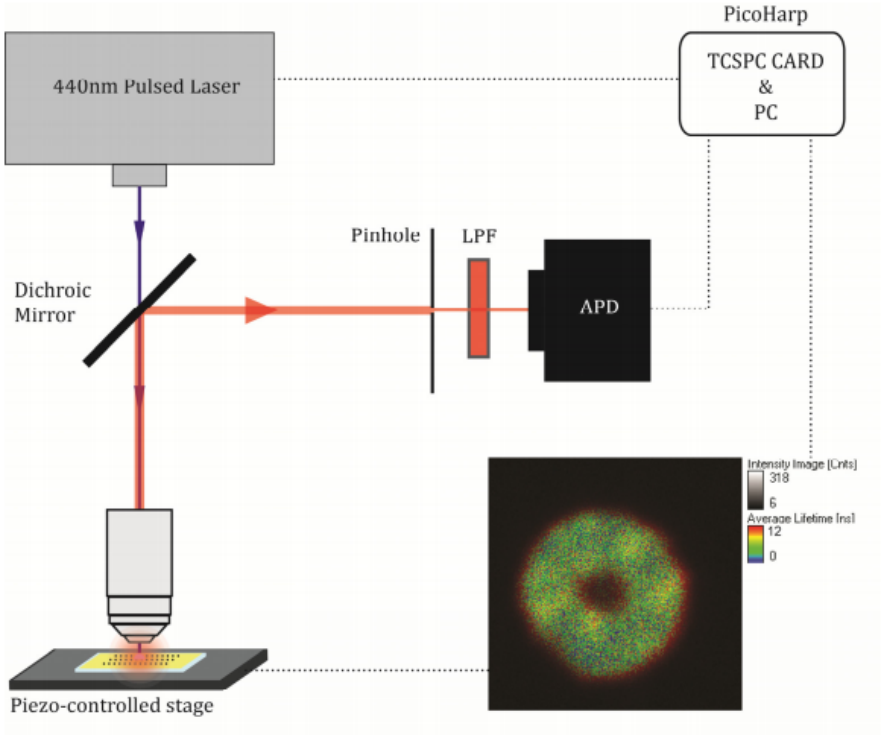

Fig. 3.11. The experimental setup measuring the fluorescence lifetime of the QD emitters embedded in the HMM is shown. The QDs are excited by a solid-state laser diode pump (440 nm, $\approx$ 90 ps pulses at 8 MHz repetition rate), while the fluorescence emission is collected in a confocal pin-hole geometry. The emission kinetics are measured via time-correlated-single-photon-counting and the collection location is raster scanned via a piezo-electric stage. Experiment credit goes to Dr. Tal Galfsky and Prof. Vinod Menon of the City University of New York. Figure reprinted with permission from ref. [50], Optical Society of America.

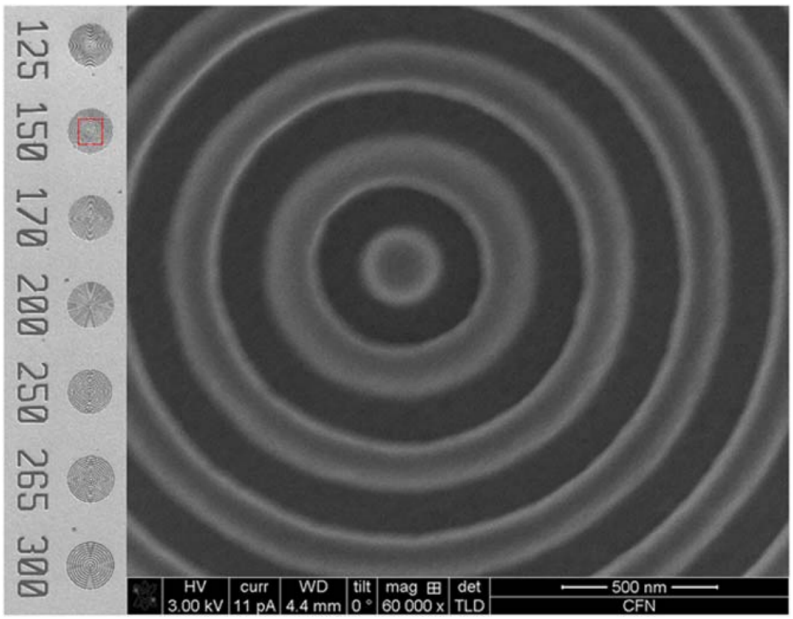

Fig. 3.12. SEM image of $\Delta = 150$ nm germanium bullseye grating on top of a multilayer metamaterial. Left inset: array of gratings with different periods. Experiment credit goes to Dr. Tal Galfsky and Prof. Vinod Menon of the City University of New York. Figure reprinted with permission from ref. [50], Optical Society of America.

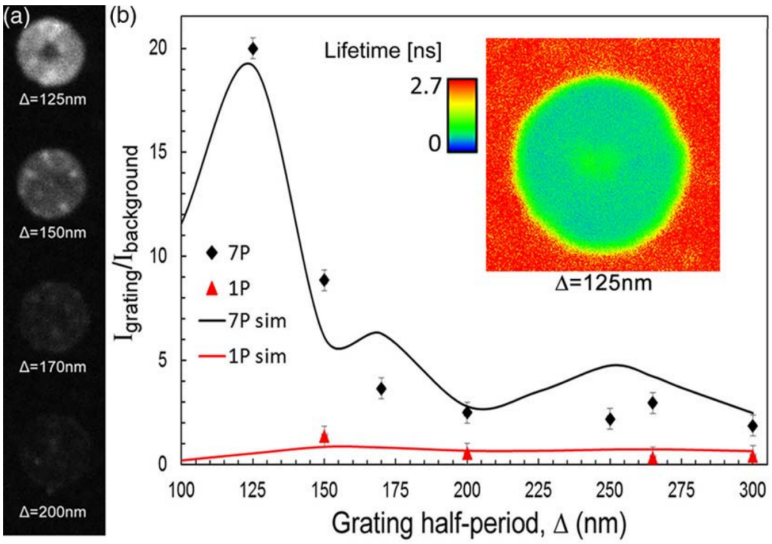

Fig. 3.13. (a) Confocal microscope image of PL emission from bullseye gratings with half periods $\Delta = 125$ nm, $\Delta = 150$ nm, $\Delta = 170$ nm, and $\Delta = 200$ nm on 7P HMM. The measurements were carried out over a scan area of 10 μm$\times$40 μm. (b) Experimentally measured ratio between the intensity at the center of the grating to that of nonpatterned background for 7P and 1P for different grating periods. Solid lines are the calculated ratios from simulations. Inset, fluorescence lifetime map of the $\Delta = 125$ nm device. Experiment credit goes to Dr. Tal Galfsky and Prof. Vinod Menon of the City University of New York. Figure reprinted with permission from ref. [50], Optical Society of America.

3.10 Conclusion

We have proposed a device using plasmonic metamaterials to efficienctly extract single photons from broadband quantum emitters such as NV centers in diamond. Detailed analysis of quenching and non-radiative decay shows that the device can achieve a broadband Purcell effect and directional far-field spontaneous emission despite the metal losses. Low mode volume confinement of the emitter and the ability to function away from plasmonic resonances holds the key to efficient outcoupling of light. The proposed structure will lead to a platform for understanding propagation of non-classical light in plasmonic metamaterials and can be integrated with other plasmonic structures for future nanoscale quantum information applications.

4. SUPER-COULOMBIC DIPOLE-DIPOLE INTERACTIONS IN METAMATERIALS

4.1 Introduction

Zero point fluctuations not only cause the decay of an excited state and energy level shifts of atoms but also induce dipole-dipole interactions (V_{dd}) between nearby atoms and molecules. These universal interactions are related to real photon and virtual photon exchange between quantum emitters and decrease in the near-field with the characteristic Coulombic dipole field law ($V_{dd} \sim 1/r^3$). The control and modification of this dramatic scaling with distance has become a long-standing theme in quantum engineering since dipole-dipole interactions govern Van der Waals forces, collective Lamb shifts, atom blockade effects and Förster resonance energy transfer. Here, we show that metamaterials can fundamentally modify the interactions and cause a near-field Coulombic scaling in spite of large physical separation between interacting quantum emitters. We demonstrate two orders of magnitude increase in the near-field resonant dipole-dipole interactions and, the surprising extension of the characteristic non-radiative Coulombic scaling law to intermediate field distances (10 times the near field). In marked distinction to existing approaches of engineering long-range radiative interactions, our work paves the way for controlling real photon and virtual photon interactions using metamaterials.

Engineering of dipole-dipole interactions has led to demonstrations of long-range qubit interactions in circuit QED [35], super-radiance of atoms and quantum wells mediated by photonic crystals [36,37] , collective lamb shifts of atoms in cavity QED [38], enhanced energy transfer between molecules in cavities [39], and quantum phases in optical lattices [40]. A unifying theme in these approaches is the enhancement of radiative interactions and departure from the far-field ($V_{dd} \sim 1/r$) scaling of interaction

with distance. A significant challenge is the control of the non-radiative Coulombic near-field interactions which scale considerably faster with distance ($V_{dd} \sim 1/r^3$) and are conventionally limited to the extreme near-field [3].

The canonical understanding of dipole-dipole interactions in cavity/waveguide QED stems from modification of the vacuum density of states and spectral tuning of atoms towards regions where the group velocity goes to zero and the corresponding density of states diverges. The two conventional approaches to achieve this criterion, as shown in figure 4.1(A-B), use either metallic waveguides operating near the cut-off frequency or cavities operating near a photonic band-edge [125–127]. The resonant nature of the density of states modification leaves little room for tolerance in terms of the range of emitters that can be used, as well as the environmental conditions necessary for direct experimental observation. All experiments so far have relied on a resonant interaction intrinsically requiring emitters with linewidths much smaller than the resonance linewidth of the cavity or waveguide mode; this condition inherently requires either cold atom systems where the linewidth of the atoms are on the order of GHz or less, or circuit QED systems where the metallic waveguide is cooled to ultra-low temperatures.

In this work, we provide the first experimental demonstration of the Super-Coulombic dipole-dipole interaction recently predicted to occur in hyperbolic media [46]. We employ many-body dipole-dipole interactions between quantum emitters mediated by a nano-structured hyperbolic metamaterial to show the dramatic spatial extension of the Coulombic near-field compared to conventional media. Our work is the first to provide a direct comparison between theory and experiment comparing the magnitude, range and distance scaling of this modified dipole-dipole interaction.

4.2 Theory

Resonant dipole-dipole interactions (RDDI) in metamaterials with hyperbolic dispersion are fundamentally different from photonic crystal waveguides [36] or cir-

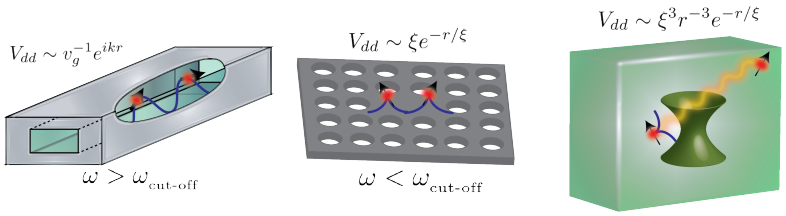

Fig. 4.1. Comparison of dipole-dipole interactions (V_{dd}) in metallic waveguides, photonic crystal band-edge structures and hyperbolic metamaterials. Here r is the distance between interacting emitters, v_g is the group velocity of the waveguide mode with wavevector k, $\omega_{cut-off}$ is the cut-off frequency of the metallic waveguide mode or photonic crystal and ξ is an interaction range. (A) When the transition frequencies of interacting atoms lie above the cut-off, they will have a sinusoidal-type interaction; (B) on the other hand, at the band-edge of a photonic crystal there occur interactions with a divergent strength as well as range (C) Hyperbolic media exhibit fundamentally different Coulombic long-range interactions which diverge for specific angular directions in the low-loss effective medium limit.

cuit QED waveguides [35]. The unique RDDI properties of the hyperbolic medium [41], which is a homogeneous material with dielectric tensor $\epsilon = \text{diag}[\epsilon_x, \epsilon_x, \epsilon_z]$ with $\epsilon_x \epsilon_z < 0$, arises from the topology of the k-surface of extraordinary waves [see SI]. It takes on a hyperboloidal relation ($(k_x^2 + k_y^2)/\epsilon_z - k_z^2/|\epsilon_x| = \omega^2/c^2 = k_0^2$) between wavevector ($\boldsymbol{k} = [k_x, k_y, k_z]$) and frequency ($\omega$) instead of the usual spherical form for conventional media. This k-surface allows for giant interactions mediated by real and virtual hyperbolic polaritons [46] along the asymptotes of the hyperboloid when the radius vector joining the two emitters makes an angle $\theta_R \approx \arctan\sqrt{-\epsilon_x/\epsilon_z}$ with respect to the optic axis (z-axis). To illustrate the unique properties of the Super-Coulombic interaction, we consider a hyperbolic medium where the permittivity along the optic axis is modeled as a free-electron Drude metal with plasma frequency ω_p,

$\epsilon_z = 1 - \omega_p^2/\omega^2$, while ϵ_x is equal to one [46], resulting in the RDDI for hyperbolic media ($\omega < \omega_P$)

$$V_{dd} \sim \frac{\omega^3 e^{-r/\xi}}{\omega_p^3 \sqrt[3]{\sin^2\theta - \omega^2/\omega_p^2}} \left(\frac{1}{r^3}\right)\Bigg(\tag{4.1}$$

where the interaction range is given by $\xi_{ideal}^{-1} = \frac{\omega_p}{c}\sqrt{\sin^2\theta - \omega^2/\omega_p^2}$ in this ideal limit. This equation shows a striking similarity to the RDDI in band-edge cavities or cut-off waveguides clearly outlining the origin of the singular Super-Coulombic interaction strength and diverging spatial range. In stark contrast to the single-frequency divergence that occurs near a band-edge, the anisotropy of the medium provides an additional degree of freedom (directional angle θ) allowing the interaction strength to diverge for a broad range of wavelengths. This result provides an interesting interpretation of the hyperbolic medium as a directionally-dependent band-gap medium where certain directions ($\theta < \theta_R, \theta \in [0, \pi/2]$) allow propagating modes with traditional Coulombic dipole-dipole interactions limited only to the near-field, while other directions ($\theta > \theta_R, \theta \in [0, \pi/2]$) only allow for exponentially decaying evanescent-type interactions. Exactly at the resonance angle θ_R (or cut-off angle) of propagating modes, there exists a diverging interaction strength similar to photonic crystals and waveguides. We further note that the resonant dipole-dipole interaction in hyperbolic media contains a dominant Coulombic r^{-3} power law dependence as opposed to either the purely exponential decay that occurs inside a photonic band gap, or the sinusoidal dependence that occurs above cut-off (see figure 4.1). Thus quantum emitters interacting along these special angular directions will have a Coulombic power law scaling irrespective of their physical separation [46, 47]. We also note that the two-dimensional quasi-static (Coulombic) equation in the hyperbolic medium remarkably resembles a wave equation implying the extension of Coulombic near-fields to infinity [46, 47]. Figure 4.2 (A) shows the point-to-point scaling of RDDI along the resonance angle for a hyperbolic medium with realistic loss compared to metal (Ag) and dielectric (SiO_2). These long-range Coulombic (non-radiative) interactions are

fundamentally different from long-range radiative interactions [103] and interactions in plasmonic waveguides [72, 128, 129].

The real part of the RDDI generally predicts a cooperative frequency shift, while the imaginary part predicts a cooperative decay rate between resonant atoms. Isolating such effects is quite difficult at room temperature due to inhomogeneous broadening and vibrational dephasing mechanisms that destroy coherence between atoms. Nevertheless, it is still possible to isolate dipole-dipole interactions at room temperature through the well-known Forster resonance energy transfer process [130]. This type of dipole-dipole interaction is an energy transfer process which occurs when two distinct molecules with overlapping emission and absorption spectra are in the extreme near-field ($<$ 10 nm apart). The FRET rate is dependent on the squared magnitude of the RDDI, $\Gamma_{ET} = 2\pi\hbar^{-1}|V_{dd}|^2\delta(\hbar\omega_a - \hbar\omega_b)$, thus providing a direct probe of the Super-Coulombic dipole-dipole interaction (Figure 4.2). Here, the delta function $\delta(\hbar\omega_a - \hbar\omega_b)$ imposes the requirement that the two dipole transitions must occur at the same energy (emission and absorption overlap). This energy transfer provides an additional decay channel for the excited state of the donor and here we use this increased relaxation rate of the donor excited state as a distinct signature of FRET across a 100 nm metamaterial (Figure 4.2(C,D)). The broadband and non-resonant nature of hyperbolic dispersion [44, 112] allows us to observe the Super-Coulombic interaction through FRET at room temperature and at optical frequencies. In experiment we choose as the interacting FRET molecules, the organic dyes Alq3 (donor, peak emission $\lambda \approx 523$ nm) and R6G (acceptor, peak absorption $\lambda \approx 525$ nm) whose FRET radius we estimate to be $R_o \approx 5.1$ nm using their photoluminesnce and absorption spectra.

4.3 Design of Metamaterial

Extremely thin films ($<$ 2 nm) of Alq3 donor molecules are spin-cast onto glass substrates. On top of these dyes we then fabricate a metal-dielectric thin film imple-

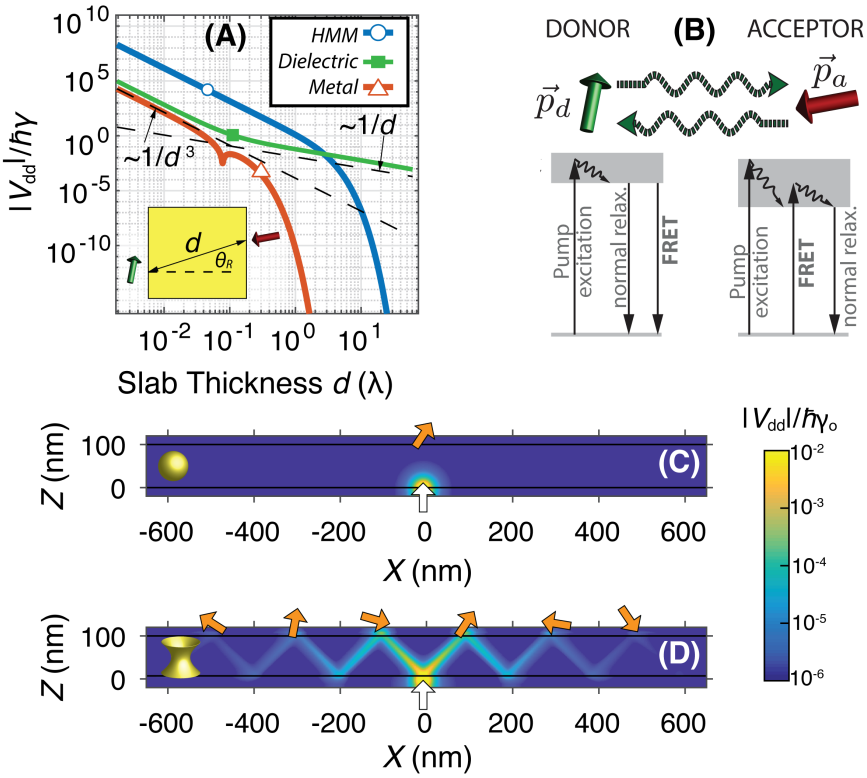

Fig. 4.2. (A) The calculated vacuum fluctuation induced dipole-dipole interaction potential is shown for two molecules separated by a realistic (dissipative) slab of HMM, SiO_2 and Ag is shown. γ_o is the free space decay rate. The HMM provides strong dipole-dipole interactions along the asymptotes of the resonance cone which show a Coulombic near-field scaling ($\sim 1/r^3$) even for distances comparable with the free-space wavelength – orders of magnitude stronger than conventional materials. The HMM dielectric constants are $\epsilon_x \approx -4.2 + 0.2i$, $\epsilon_z \approx 5.4 + 0.01i$. (B) FRET is used as a probe for long-range super-Coulombic RDDI. The donor atom's radiative dipole transition is resonant with the acceptor absorption dipole-transition. (C,D) The enhanced RDDI mediated by directional hyperbolic polaritons is shown for a dipole located below a 100 nm slab of SiO_2 and HMM. The HMM allows a single dipole (white arrow, bottom) to interact with many physically separated acceptors (orange arrows, bright regions, top) giving rise to unique super-Coulombic enhancements for thin films of acceptors and donors.

mentation of a hyperbolic medium: electron beam evaporation of a multilayer stack of alternating silver/silicon dioxide layers (20 ± 2 nm thick layers $\ll \lambda_{Alq3} = 525$

nm) . Deviations from effective medium theory are expected but ellipsometric transmission and reflection measurements confirm that hyperbolic dispersion is achieved within the entire bandwidth of overlap between the emission spectrum of the donor and absorption spectrum of the emitter. The effective dielectric constants can be approximated by $\epsilon_x \approx -4.2 + 0.2i$, $\epsilon_z \approx 5.4 + 0.01i$ at $\lambda = 525$ nm [66]. This confirms the effective hyperbolic dispersion behavior essential to create super-coulombic interaction pathways.

Figure 4.3(A) shows the comprehensive set of samples required to demonstrate super-Coulombic interactions in the metamaterial, not present in any conventional material. We isolate the role of the metamaterial on enhancing RDDI as opposed to its role in increasing two competing physical phenomena - the local photonic density of states (LDOS) and non-radiative quenching of donor molecules on top of the metal. [34, 119, 131]. This is achieved using a careful comparison between donors with acceptors (hybrid, front row of figure 4.3(A)) to the donor-alone and acceptor alone cases (middle and back rows, figure 4.3(A)). Along with the metamaterial, we fabricate Ag and SiO_2 control samples of equal thickness to the metamaterial (100 nm).

4.4 Photoluminescence Enhancement

To demonstrate evidence of energy transfer from donors to acceptors we measure the steady state fluorescence of the control samples and contrast these to the hybrid, donor with acceptor samples. Figure 4.3(B,C,D) shows the transmitted photoluminescence (PL) spectra of the control samples and the hybrid samples for the three types of material systems. The samples are optically pumped with steady state fluence of $\approx 25\mu$/W/1 mm^2 from 405 nm CW laser. We note clear evidence of energy transfer from donors to acceptors in all three material systems. We conclude this by observing that when acceptors are present on the opposite side of the donors (hybrid, black curve), there is an increase in the acceptor emission intensity compared

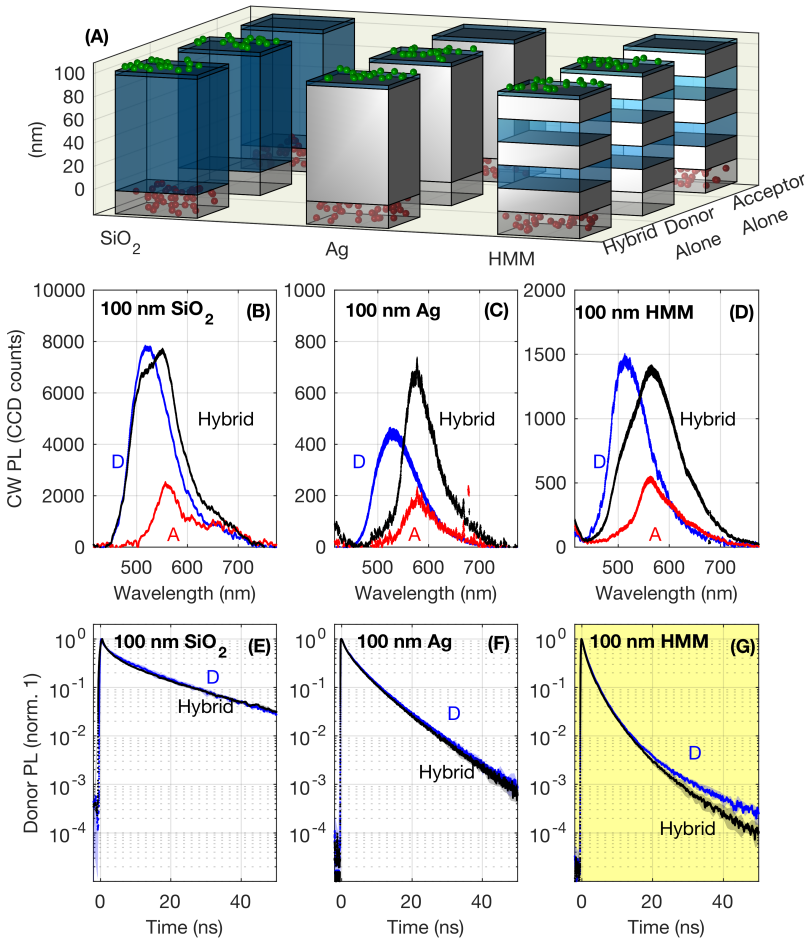

Fig. 4.3. (A) The sample-types used to isolate RDDI in various material systems is shown. Donors (Alq3) are shown green on top while acceptors (R6G) are shown red on the bottom. (B,C,D) The transmitted PL spectra for the donor and acceptor separated by dielectric, metal and metamaterial is shown. We note that energy transfer is clearly visible in all three material systems; that is, the donor excited state is causing the acceptor to be excited and subsequently relax and emit a photon. This is concluded by noting an increased intensity of acceptor emission and a quenched donor emission when the emitters are placed in the hybrid geometry (black curve) relative to the donor-only (blue curve) and acceptor-only (red curve) control systems. (E,F,G) The time resolved donor fluorescence for donor-only (blue) and hybrid (black) samples are shown for the three material systems. For the donors:acceptors separated by 100 nm of SiO_2 or Ag (G, H), the hybrid decay traces reveal no additional lifetime reduction compared to the donor-only case, indicating no long-range RDDI. When the donor and acceptors are separated by a 100 nm Ag/SiO_2 multilayer metamaterial (G), we observe a marked excited state lifetime reduction when the acceptor molecules are present, providing evidence of long-range super-coulombic RDDI.

to acceptors alone (red curve). This is accompanied by a decrease in donor emission intensity (relative to donors alone, blue curve).

To gain insight into the nature of this energy transfer process, we utilize time-resolved emission kinetics of the Alq3 donor and isolate the additional increase to the donor relaxation rate in the presence of R6G acceptors across the metamaterial.

4.5 Time-Correlated Single Photon Counting Measurements

Figure 4.3(E) compares the decay trace for the 100 nm SiO_2 film with and without acceptors. We denote these traces by D (blue data points) and Hybrid (black data points). We note that the introduction of acceptors to the far-side of the SiO_2 film produces no change in the emission kinetics, despite the fact that the steady state fluorescence indicates that there is energy transfer from donors to acceptors. This clearly shows that the energy transfer mechanism is radiative, mediated by a photon emitted by the excited donor which propagates through the 100 nm SiO_2 film and is subsequently absorbed by the acceptor. The 100 nm Ag material system only causes the well-known decrease in lifetime of the donor lifetime due to the metallic environment [104, 132]. Similar to the SiO_2 thin film, this system also lacks strong long range interactions since no additional decrease in lifetime is observed when the acceptors are introduced on the opposite side of the metal [133].

Figure 4.3(G) shows the fundamentally different emission kinetics of the donor in the HMM system. The donor only sample shows a decreased excited state lifetime relative to the pure Ag sample (blue Figure 4.3(F)). This is due to the enhanced optical density of photonic states in the near-field of HMMs [112,119]. When acceptors are introduced on the opposite side of the HMM in the hybrid sample (black data points), we observe a marked additional reduction in the excited state lifetime of the donor. This lifetime reduction offers proof of super-Coulombic dipole-dipole coupling of donors and acceptors with a physical separation distance of 100 nm.

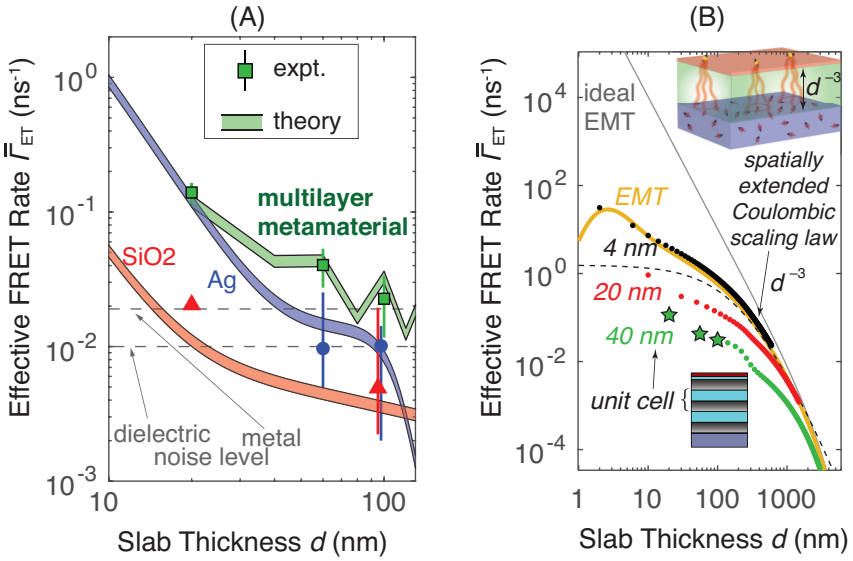

Fig. 4.4. Spatial scaling of Super-Coulombic interactions. (A) Experimental confirmation of enhanced energy transfer rates due to the Super-Coulombic effect in a hyperbolic metamaterial (green) compared to silver film (blue) and SiO_2 film (red). The noise floors are denoted by dashed curves and the numerically calculated many-body dipole-dipole interaction curves are denoted by the colored bands. The theoretical predictions include 10% error bands accounting for uncertainty in the independently extracted physical parameters. (B) Numerically simulated spatial dependence of sheet-to-slab (2D sheet of donors and thin slab of acceptors) many-body dipole-dipole interactions demonstrating an enhanced FRET rate of the effective medium model (yellow) with $\sim d^{-3}$ power law dependence. Super-lattice structures with unit-cell sizes of 40 nm, 20 nm, and 4 nm respectively are also shown exhibiting an extended spatial range with enhanced Coulombic interactions beyond the scale of a wavelength. The green stars correspond to the experimentally measured data. The solid grey line shows the ideal EMT limit of adsorbed quantum emitters on a hyperbolic medium whereas the dashed black line presents the analytical scaling law taking into account the finite distance between the emitter and metamaterial.

4.6 Comparison of Theory and Experiment

To elucidate the distance scaling law of dipole-dipole interactions mediated by metamaterials, we fabricate additional structures displaying varying strengths of

RDDI owing to the different separation distance (20, 60 nm) between donors and acceptors. We robustly quantify the effective FRET strength between the donors and acceptors using the harmonic mean of the measured decay rates of the donor emission kinetics with and without the presence of acceptors (see SI, [130]). If the observed decay traces $I(t)$ are normalized to unity at time zero, then the integral of the trace over time yields the average excited state lifetime, that is $\bar{\gamma}^{-1} = \bar{\tau} = \int dt I(t)$. Since we are in the weak coupling limit, the difference between the average decay rate of the donors with and without acceptors present yields the effective FRET rate of donors to acceptors: $\bar{\Gamma}_{ET} = \bar{\gamma}_{DA} - \bar{\gamma}_{D}$.

The observed effective FRET rates and their scaling for the three separation distances between donor and acceptor molecules are shown in figure 4.4. To connect these data with theory, we have developed a rigorous theoretical framework of many-body dipole-dipole interactions which allows for quantitative comparison of the metamaterial response in the ideal effective medium theory (EMT) limit as well as the practical absorptive-dispersive, finite-sized multilayer structure. Using only physical quantities extracted independently from experiment (permittivity, layer thicknesses, FRET radius, donor decay rate, and acceptor concentration) and no fitting parameters, the many-body Super-Coulombic interaction theory shows excellent agreement with experimentally observed FRET rates across the metamaterial (figure 4.4(A)). The enhancement of FRET due to the HMM is close to two orders of magnitude compared to the dielectric and one order of magnitude compared to the metal. We note that our simulations take into account the discrete nature of the metamaterial and the sawtooth behavior of the RDDI enhancement is related to the influence of the metamaterial termination layer (metal or dielectric).

We now compare the ideal super-Coulombic interaction predicted by Eq. (1) and the regime of enhanced FRET rate observed in experiment. We emphasize that the characteristic Coulombic scaling $\Gamma_{ET} \sim r^{-6}$ only occurs for point-to-point interactions along the resonance angles. In contrast, for sheet-to-slab (2D sheet of donors and thin film slab of acceptors) interactions, a many-body behavior starts manifesting since

each donor molecule can interact with multiple acceptor molecules at the base of conical region formed at the resonance angles. Using the FRET radius, concentration of dye molecules, photoluminscence and absorption spectra, collection optics and beam size, we estimate a single donor to interact with approximately 16,000 acceptors. The characteristic scaling of Coulombic energy transfer in this many-dipole interacting limit is given by $\Gamma_{ET} = \gamma_o c_a \int_d^\infty \mathrm{d}z_a \iint_\rho \mathrm{d}\rho \mathrm{d}\theta \, (R_o/r)^6 = \gamma_o c_a \pi R_o^6/6d^3 \sim d^{-3}$ where d is the distance between the sheets (see appendix C).

Motivated by the excellent agreement between theory and experiment (green stars and green dots in Fig. 4B), we compare the scaling law of interactions for the experimental realization of the metamaterial to the ideal effective medium theory limit of super-Coulombic RDDI for adsorbed quantum emitters on a hyperbolic medium (light grey line). As the unit cell size is decreased to 4 nm, a very strong agreement is noticed between effective medium theory (yellow curve) and the multilayer system (black dots). We emphasize that the dramatic spatial extension of the Coulombic scaling law ($\Gamma_{ET} \sim d^{-3}$) to beyond the wavelength scale ($d > 500nm$) in spite of losses, dispersion, absorption and finite unit cell size of the metamaterial is evidence of the super-Coulombic effect. Furthermore, the dashed black curve presents our analytical model of super-Coulombic FRET taking into account the finite distance between the emitter and metamaterial (z_a). The modified Coulombic scaling law taking into account this proximity effect is

$$\Gamma_{ET} \sim (d\,\mathrm{Re}[\sqrt{\epsilon_x/\epsilon_z}] + z_a)^{-3} \tag{4.2}$$

A strong agreement in the scaling law between EMT and multi-layer simulations occurs when the unit-cell size is significantly smaller than the molecule-interface separation distance (see SI). The spatial range of the Super-Coulombic interaction is ultimately curtailed by material absorption (ϵ'') and the resulting interaction range becomes $\xi^{-1} = \frac{\omega}{c}\sqrt{\frac{\epsilon_z''|\epsilon_x'| + \epsilon_z''|\epsilon_x'|}{|\epsilon_x'| + |\epsilon_z'|}}$.

4.7 Synergy between Theory and Experiment

The accurate modeling of our experimental results took a strong collaboration between theory and experiment. The tour de force of theory and modeling techniques used in this chapter were developed by Cristian Cortes (Purdue University) and, to our knowledge, have not been used before in many-body dipole-dipole interactions in nanophotonic environments. A detailed theoretical analysis of many-body dipole-dipole interactions in nanoscale plasmonic metamaterials will be explored fully in Cristian Cortes's thesis (expected early 2018). A brief overview of the modeling technique is outlined here. Figure 4.5 shows the flow-chart describing the careful strategy required to go from point-to-point dipole-dipole interactions to the many-body super-Coulombic dipole-dipole interactions observed in experiment.

Point-to-point dipole-dipole interactions near the hyperbolic metamaterial are modeled with a Green's function method. At this point, key experimental parameters are input such as experimentally observed thicknesses and dielectric permittivities to accurately model the exact structure used in the experiment. Experimental uncertainties are also included and carried forward into the next step.

Position (six degrees of freedom) and dipole orientation (6 degrees of freedom) averaging of the RDDI fields are then completed with a combination of numerical integration, identification of degeneracies, and clever simplifications with less well known mathematical identities of the cylindrical Bessel functions that appear as basis functions in the Green's function of dipoles near planar structures. Several key experimental constants such as FRET radius, acceptor molecule concentration and donor fluorescence lifetime are required to accurately model the ensembles of donors and acceptors in experiment. Uncertainties in these physical constants are also inserted into the model to predict the error bands on the theory curves appearing in figure 4.4(A).

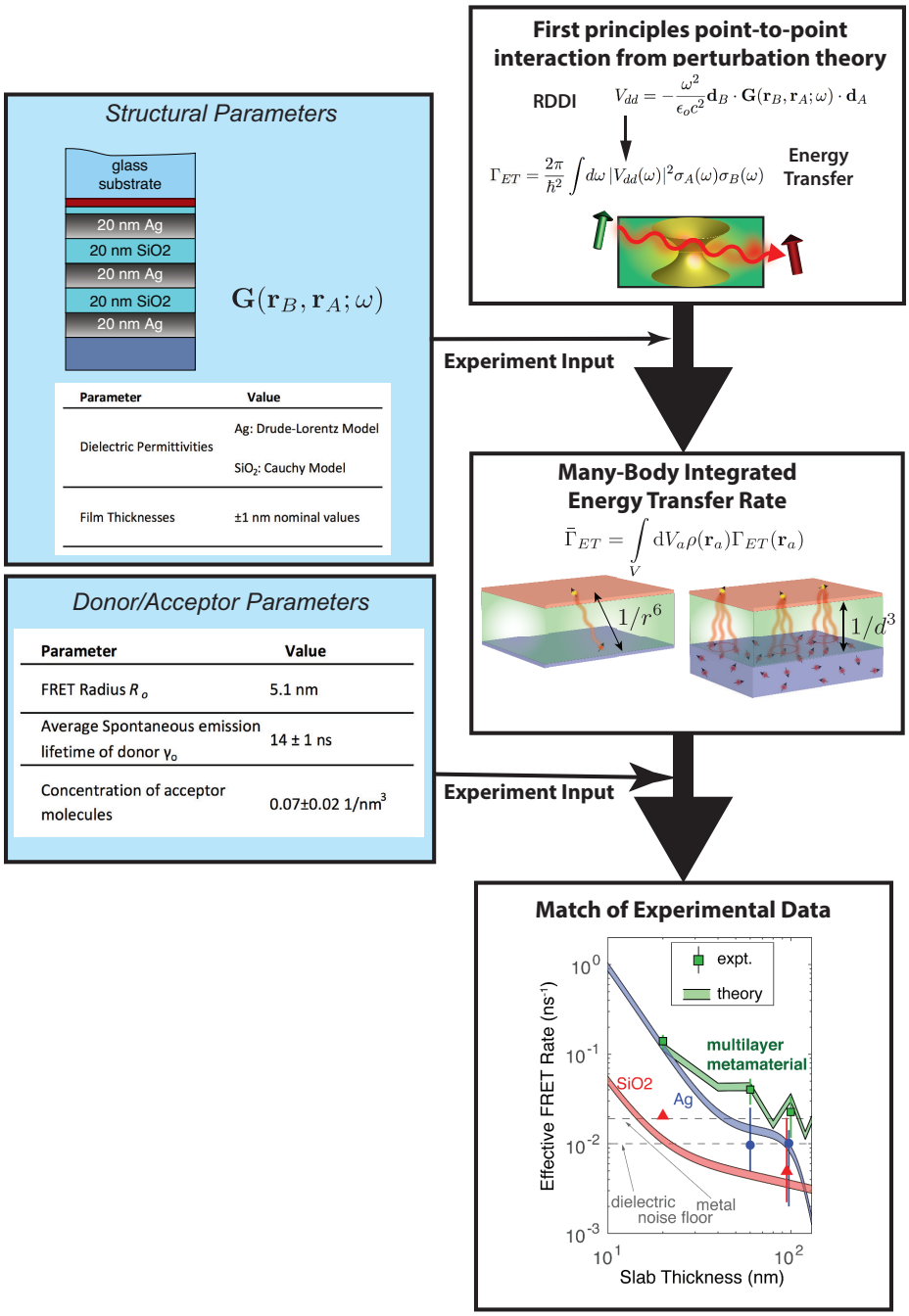

Fig. 4.5. The schematic flow chart describing the modeling of many-body super-Coulombic interactions is shown.

4.8 Conclusion

This metamaterial mediated non-radiative Förster interaction with with Coulombic scaling should be contrasted with the previously reported super-radiant lifetime change in quantum dots which only showed a radiative interaction and $V_{dd} \sim 1/R$ scaling at the comparable distance of 150 nm [134]. Furthermore, two mesoscopic atomic clouds have shown Förster interaction at 40 microns [135]. However, the transition wavelength is 1 cm placing the experiment in the extreme near-field regime ($d \approx \lambda/250$). For comparison, if similar mesoscopic atomic systems were interacting through a hyperbolic metamaterial functioning at $\omega = 30$ GHz $\equiv 1$ cm, the interaction distance would be a centimeter.

In conclusion, we have demonstrated long-range Super-Coulombic dipole-dipole interactions mediated by metamaterials which fundamentally extend the non-radiative near-fields as opposed to engineering radiative interactions. We envision that Super-Coulombic interactions can impact deterministic entanglement creation between remote emitters [136], quantum coherence [137, 138] in metamaterial mediated photosynthetic energy transfer, lead to many-dipole interactive states in metamaterials [126], increase the range of biomolecular FRET rulers as well as FRET imaging systems [139], and accelerate progress towards the long-standing goal of strongly coupled quantum systems at room temperature ($V_{dd} > k_b T_{room}$).

5. RESONANT DIPOLE-DIPOLE INTERACTIONS IN DISORDERED PLASMONIC MEDIA

In this chapter we provide evidence of RDDI enhancement in the vicinity of disordered plasmonic media. A significant amount of research has shown the ability of random plasmonic media to engineer spontaneous emission [130, 140], and act as seed locations in random nanolasers [141, 142]. However, very little work has investigated the effects of such disordered media on dipole-dipole interactions. Here we show that a thin-film of disordered gold nanoparticles results in a 50% increase in the effective FRET radius of donor-acceptor pairs. Since dipole-dipole interactions scale so rapidly in the near-field, this results in the observation of a thirteen times increase in the FRET rate relative to a glass or thin metal substrate. This increase in FRET rate is larger than the increase in fluorescence decay rate due to the interactions of the individual emitters with the plasmonic environments. This work then makes major progress to the long-standing goal of engineering emitter-emitter interactions (dipole-dipole coupling) beyond the coupling of the individual emitters with the photonic environment. This result stands in contrast to several other experiments and theory work that claim that plasmonic substrates can only reduce or enhance RDDI by about a factor of 1.5 [34, 143]. We predict that this increased range of dipole-dipole interactions on disordered gold nanoparticle substrates will provide a rich testing ground of QED in disordered plasmonic media and also offer a simple solution for increased FRET interactions in bio-imaging.

5.1 Introduction

Nanoscale metal particles support resonant electromagnetic states called localized surface plasmon polaritons (LSPs). They arise from the coupling of the photonic

radiation field with the motion of free electronic charges within the metal. The electromagnetic energy density of LSPs is enhanced and sharply confined to the particle. As a result, in the near-field of plasmonic nanoparticles (NPs), electromagnetic fluctuations are strongly altered. This has resulted in a explosion of work in engineering spontaneous emission [114, 130, 144], stimulated emission [145], Raman scattering [146], and even novel optics such as filters and polarizers [147, 148]. There is definitive evidence that dipole-dipole interactions can also be tailored via plasmonic NPs. Recent work has shown that carefully designed individual plasmonic particles can enhance FRET in the immediate near-field of LSPs [149, 150].

Random plasmonic NP ensembles have been used to engineer spontaneous emission in colloidal suspensions and numerous applications have emerged in bio-imaging [130, 140] and nanoscale light sources such random lasers [141, 142]. However, open questions remain on the ability of random plasmonic media to alter or enhance dipole-dipole interactions. Here, we fabricate a thin-film of disordered, self-assembled gold NPs and show that such a film enhances resonant dipole-dipole interactions beyond the coupling of the individual dipoles (emitters) with the photonic environment. This work then makes criticial progress to the long-standing quantum engineering goal of tailoring emitter-emitter coupling to be stronger than emitter-environment coupling.

5.2 Fabrication and Characterization of Disordered Gold Nanoparticle Films

Here, we exploit the concept of the percolation threshold in metals to fabricate disordered plasmonic media. When thin metal films are deposited via physical vapor deposition techniques such as sputtering or electron beam evaporation there exists a critical thickness called the percolation threshold, below which the metal film is not continuous but semi-continuous and island-like [151]. At this threshold there are significant changes to the physical properties of the film [152,153]. For example, when the film is thicker than the percolation threshold, it will tend to conduct electricity

with a conductivity similar to the bulk; as discussed extensively in Chapter 2 a thin continuous film of metal will also support a radiative bulk plasmon called a Ferrell-Berreman mode. On the contrary, when the film is thinner than the percolation threshold, the island-like metallic film will not continuously conduct electricity and no Ferrell-Berreman mode will be supported. Interestingly however, the individual metallic islands, regardless of how oddly they are shaped support localized surface plasmons (LSPs) that couple to free space radiation [140, 144]. Typically, these semi-continuous island-like films have an extremely complex morphology and as a result, even small nanoscale areas (< 100 nm^2) support LSPs at a broad range of spectral frequencies. Here, we apply a rapid annealing process to semi-continuous gold films that triggers the self-assembly of a thin-film of gold NPs. Although the exact physical locations of the particles remain random and disordered, we find the self assembled gold NPs are of a circular island shape and their LSPs resonate at a very consistent spectral frequency.

A brief overview of the fabrication procedure is provided below while a detailed description of the fabrication is provided in the appendix D. We start by sputtering a 3 nm layer of gold (Au) on a glass microscope slide substrate. This thickness is below the percolation threshold of Au ($\approx 6 - 10$ nm) and the Au film is semi-continuous and island-like as revealed by an atomic force microscope (AFM) as shown in figure 5.1(a). We then anneal the semi-continuous Au film in an inert nitrogen atmosphere at 600^oC for four minutes. Although this is below the melting temperature of bulk gold ($\approx 1,064^o$C), the small islands are able to migrate, reflow and recombine into larger NPs at this elevated temperature [124, 151]. The annealing process yields well defined circular looking NPs as shown in figure 5.1(b).

Using the open access AFM analysis software *Gwyddion*, we extract the particle and island size statistics using a common watershed/grain analysis method. Figure 5.1(c,d) shows the NP size distributions for the annealed and unannealed Au films. We observe that the annealing process causes the average NP size to increase by about a factor of five while the particle height increases by about a factor of eight. We find

empirically that in both the unannealed and annealed samples the particle height is approximately the cube root of the particles' lateral radius. From this, we conclude that the NPs and islands are not spherically symmetric but probably shaped similar to a pancake or downwardly squeezed sphere.

If we assume the gold NPs are half ellipsoids, then the total volume of the unannealed islands to that of the annealed gold NPs is smaller by about a factor eight – a violation in conservation of mass (elemental gold in this case). This indicates that our particle shape extraction algorithm is flawed and that we need to take into account the finite tip size of the AFM probe. These effects are likely to be significantly higher on the unannealed gold islands and more thorough AFM techniques will need to be used to accurately extract the sizes and distributions of the gold islands here. A TEM cross-section would further elucidate the exact shape distributions of the NPs and islands, and would thus result in more accurate electromagnetic modeling of the NP film optical response. This is beyond the immediate scope of the current work and is an ongoing subject of future work.

5.3 Localized Surface Plasmon Resonances of Disordered Gold Nanoparticle Films

Figure 5.2(a) shows the measured specular extinction spectra of the disordered gold nanoparticle films. The extinction spectra shows optical losses experienced by a specular beam due to both scattering and absorption losses. We note that the annealed Au film displays a resonant extinction peak at around $\lambda \approx 530$ nm. This observation provides evidence of the presence of well defined LSP resonances in the annealed gold NP film since spherical gold nanoparticles are well known to have a strong scattering and absorption cross section around $\lambda \approx 520$ nm. The unannealed island-like film, on the other hand, displays a broad spectral extinction with no marked resonance; the complex island morphology results in the islands' LSPs resonating in a broad spectral range with poor quality factors [124, 140].

We deposit an ultrathin 4 nm conformal coating of Al_2O_3 on the Au nanoparticle films via atomic layer deposition (ALD) to prevent NP migration/agglomeration and any unwanted chemistry between the gold NPs and fluorescent emitters. Plasmonic resonances are extremely sensitive to the local dielectric media surrounding the metal/dielectric interfaces, and as the Al_2O_3 dielectric film thickness increases, the LSP resonance red-shifts and the quality factor increases. The quality factor increases due to the fact that the Al_2O_3 can support a higher proportion of the LSP resonance electromagnetic energy density than vacuum; as a result, more of the LSP electromagnetic energy is contained within the dielectric coating surrounding the NP, and Ohmic losses within the metal play less of a role in damping the resonance.

We model the extinction spectra of the annealed gold NP film with Mie scattering theory [140, 144]. Figure 5.2(a) shows the relatively good agreement of the Mie scattering theory with experimental observations, confirming that we are indeed observing a LSP resonance. In the modeling, the experimentally extracted ensemble of gold nanoparticle sizes and densities (inset) must be included to accurately predict the spectral location, width and strength of the disordered film's LSP extinction resonance. Here we assume that the gold NPs are spherical (and not island-like) in shape; mutual coupling between the adjacent gold NPs was also neglected. Further details of this modeling can be found in the appendix D.

5.4 FRET Experiment Details and Methods

We monitor FRET in the near-field of our gold nanoparticle films to investigate the effects of disordered plasmonic films on resonant dipole-dipole interactions. We fabricate 20 nm layers of dye-doped PMMA films on top of the disordered gold NP substrates via spin casting (figure 5.2(b)). The donor was the fluorescent dye Alq3, while the acceptor was the organic laser dye R6G. The Alq3 donor concentration in the PMMA was about 3.6×10^{19} dyes/cm^3 while that of the R6G acceptor was about $1.1 = \times 10^{19}$ dyes/cm^3. Films consisting of donor-only and acceptor-only were

also fabricated to isolate the effects of the LDOS from those of RDDI. The peak FRET interaction strength occurs at $\lambda \approx 525$ nm, where there is maximum emission-absorption overlap between the donor-acceptor pair (blue vertical band, figure 5.2(a)).

We quantify FRET by monitoring fluorescence emission spectra and kinetics of the dye-doped PMMA films on top of the disordered gold NP substrates. Figure 5.3 shows a schematic of the experimental setup. With very fast, minor changes to the apparatus (flip mirrors), the setup is capable of measuring dark-field plasmonic NP scattering, fluorescence spectra, and fluorescence emission kinetics of the same physical sample area. The benefits of this experimental apparatus are discussed below.

Utilizing a refractive total-internal-reflection prism, we pump the sample with the evanescent decaying light field of pulsed white light (see appendix E). The LSP resonances of the gold NP film strongly scatter the white light, and we directly obtain high magnification images of the disordered plasmonic film with an imaging spectrograph and intensified CCD camera.

To measure the fluorescence of the donors and acceptors, we pump the dyes in a confocal geometry with ultrafast laser pulses (400 nm, 30-50 fs, 100 KHz, 7 μW, spot size ≈ 9 μm^2), coinciding with the minimum of the acceptor absorption band . The resulting fluorescence is collected and sent to the aforementioned imaging spectrograph as well to a single photon avalanche diode (SPAD) coupled with time-correlated single photon counting (TCSPC) electronics. This allows the simultaneous measurement of fluorescence spectra and emission kinetics.

To avoid any spurious effects of aggregate dyes or large Au NPs, it is critical that we observe FRET in a region of high uniformity of dyes and plasmonic NPs. Of course microscopically the NPs and dyes will be extremely random, however, we must avoid any large obvious defects. Figure 5.4 show an example of this.

Figure 5.4(a) shows the dark-field scattering image of the disordered gold NPs film A small region of abnormally bright signal is observed in the bottom left of the image. This is likely due to a larger agglomeration of gold NPs that are also occasionally observed via AFM. We avoid this region by collecting fluoresence away from the defect

center as shown in figure 5.4(b). The basis of the resulting spectral measurement of this region is shown in panels (c-d). Emission kinetics of the fluorescence from the same physical region is also sent to the SPAD and TCSPC electronics.

After a typical fluorescence data acquisition, we retake a scattered white-light dark-field image to ensure the laser pump for fluorescence measurements has not physically altered the gold NP film (see figure D.8 in appendix D.7 for an example of such damage). It is relatively easy to ablate and melt the gold nanoparticles with 400 nm light since gold has strong interband absorption in this region. To avoid this unwanted side effect of the fluorescence laser pump, we ensure the 30-50 fs duration 400 nm laser pump is kept to pump fluences less than 70 pJ/9 μm^2. In the next section, we utilize the power of this experimental setup to show that dipole-dipole interactions are enhanced in the vicinity of disordered gold NP films.

5.5 Evidence of Enhanced Dipole-Dipole Interactions on Disordered Gold Nanoparticle Films

Figure 5.5 shows the spectral fluorescence intensities of donor only (D), acceptor only (A), and donors with acceptors (DA) deposited as a 20 nm thick homogeneous mixture on top the Au NP substrate. These data show the spectral signature of FRET in the donor with acceptor mixtures. In figure 5.5(a) we observe the donor fluorescence intensity is quenched while that of the acceptor is enhanced.

The differential spectra, defined as the difference between the FRET emission spectra (DA) and the sum of the donor alone and acceptor alone emission spectra (D+A) quantifies the quenching and enhancement intensities (figure 5.5(b)). We observe that the acceptor emission is enhanced by nearly two times the amount that the donor is quenched! This quantitative result hints that at least some of the energy transfer from donor to acceptor is being mediated by dark-modes – LSP modes that rigorously do not couple to the far-field. Examples of such modes are multipolor localized surface plasmon of the NPs such as quadrapole and octopole modes [140].

It is also probable that more complex dark mode band structures are supported by the disordered plasmonic films. Interestingly, these dark modes are not observed in far-field specular extinction measurements as shown in figure 5.2. To elucidate this interesting observation, a much more thorough quantitative analysis is required including the internal quantum efficiencies of the dyes, far-field Purcell factors, and the coupling of the quantum emitters to bright and dark LSP modes on the microscopic distance scales of the disordered films. Complex electromagnetic modeling of the disordered gold NP films is required to fully quantify the Purcell factors and quantum coupling of emitters to the disordered gold NP array, and this is the focus of future work.

Figure 5.6 shows the donor emission kinetics for the donor alone and donor with acceptor samples for dyes mixed on top of our gold nanoparticle substrate. We also show the relevant emission kinetics for the control samples of glass (dielectric environment) and continuous gold film (metallic environment). All of the samples contain a 4 nm Al_2O_3 spacer layer as a control. In all three material systems, we observe a reduction in the donor fluorescence lifetime due to FRET when acceptor molecules are mixed with the donors. We unravel the separate effects of the LDOS and RDDI on the emission kinetics below.

As described in the preceding chapter and derived in the Appendix C.1, we robustly quantify the effective decay rate $\bar{\Gamma}$ of a normalized emission trace $I(t)$ with the equation $\bar{\Gamma} = I(0)/\int I(t)\mathrm{d}t$. We emphasize that this calculation yields the harmonic mean of the decay rate distribution $A(\Gamma)$ and takes into account all decay rates present in the decay trace $I(t)$, not just the long or short times-scales. Figure 5.7(a) shows the effective decay rate for the donor alone (blue squares) and donor with acceptors (red stars) for all three material systems. We observe the well known decay rate enhancement due to surface plasmon polaritons for the donors alone on top both metallic material systems. Note that the donor alone decay on top of the disordered Au NP films is faster than the donor alone on top of continuous Au film despite the fact that at long time-scales, the continuous Au system decays faster.

We now emphasize that for all three material systems the addition of the acceptor has increased the effective decay rate of the donor due to FRET ($\bar{\Gamma}_{\mathrm{DA}} > \bar{\Gamma}_{\mathrm{D}}$). We define the effective FRET rate as the difference between the average decay rate of the donors with and without acceptors present: $\bar{\Gamma}_{ET} = \bar{\Gamma}_{DA} - \bar{\Gamma}_{D}$. Figure 5.7(b) shows the FRET rate (green circles) alongside the donor alone decay rate (blues squares, same as panel (a)). We note that the FRET rate on the 18 nm continuous gold substrate is only slightly larger than that on glass (1.3×). This agrees with recent observations of FRET mixtures on smooth metallic films and multilayer hyperbolic metamaterials made by Noginov, Poddubny and co-workers [143, 154]. However, in the case of the disordered gold nanoparticle substrate, we observe a thirteen times increase in the FRET rate relative to on glass! This indicates that the effective FRET strength and RDDI have drastically increased on top of the disordered nanoparticle substrate. Furthermore, the effective FRET rate increase on the gold NPs has outpaced that of the LDOS: the effective FRET rate is larger than the donor's spontaneous emission rate by about 20%.

The precise reason for this tremendous enhancement of RDDI is not fully explored at the moment but must be due to the precise band structure and specific electric field distributions of the plasmonic modes supported by the disordered plasmonic NP substrate. Photonic bandstructures of disordered media is an active field of research [155] and work in this direction in the context of enhanced RDDI will yield a rich testing ground for QED interactions in disordered systems.

The quantum FRET efficiency η_{ET} is defined as the probability of FRET relative to all other decay processes, and is expressed mathematically as $\eta_{ET} = \bar{\Gamma}_{ET}/\bar{\Gamma}_{DA}$. In Figure 5.7(c) we plot the FRET efficiency η_{ET} along with the spontaneous emission rate enhancement $\beta = \bar{\Gamma}_{D}/\bar{\Gamma}_{D}^{\mathrm{glass}}$ for the three material systems. On glass we observe the FRET efficiency to be about 48%. This indicates that within the mixture, donors are separated by acceptors by about the FRET radius R_o on average[1] On the

[1]The FRET radius is defined as the donor-acceptor separation distance at which the FRET rate equals the spontaneous emission rate. At this distance $\eta_{ET} \equiv 50\%$.

Table 5.1.
The summary of key decay rates $\bar{\Gamma}$, Radiative Decay Rate Enhancements β and FRET efficiencies η is shown for the two control samples and the NP sample.

	SiO_2	18 nm Au	Au NPs
$\bar{\Gamma}_D$ (ns^{-1})	0.05	0.31	0.44
$\bar{\Gamma}_{DA}$ (ns^{-1})	0.09	0.37	1.04
$\bar{\Gamma}_{ET}$ (ns^{-1})	0.04	0.06	0.60
$\bar{\Gamma}_{ET}/\bar{\Gamma}_{ET}^{\mathrm{glass}}$	1	1.2	12.2
$\beta = \bar{\Gamma}_D/\bar{\Gamma}_D^{\mathrm{glass}}$	1	6	9
$\eta = \bar{\Gamma}_{ET}/\bar{\Gamma}_{DA}$	48%	17%	58%

continuous gold film, the FRET efficiency is reduced dramatically to 17% since the radiation rate has significantly increased while the FRET rate has remained the same; this indicates most of the donor decay above continuous gold is comprised of emission into surface plasmons that radiate away some finite distance before being absorbed by the gold or acceptors. Above the disordered gold NP film we estimate a FRET efficiency of 58%, a 10% improvement over the glass substrate. The key quantative results from above are summarized in table 5.1.

5.6 Discussion: Anisotropic FRET Interactions

We now estimate the effective increase in FRET radius of the donor-acceptor pair on top of the golf NP films. The FRET rate within glass is calculated with the well known spherically symmetric Förster equation $\bar{\Gamma}_{ET}^{\mathrm{glass}} = (R_o/\langle R\rangle)^6$, where $R_o = 5.1$ nm for our donor-acceptor pairs in PMMA, and $\langle R\rangle$ is the expectation value of the donor-acceptor separation distance in PMMA. Assuming the RDDI interactions above the Au NP film is also spherically symmetric and isotropic (a crude assumption to be sure), then a similar equation holds for the FRET rate above the Au NPs,

$\bar{\Gamma}_{ET}^{\mathrm{NPs}} = (R_o^{\mathrm{NPs}}/\langle R\rangle)^6$, where R_o^{NPs} is effective the FRET radius above the gold NPs. Since the concentration of dyes is the same above glass and above the gold NPs, then $\langle R\rangle$ is equivalent in both cases. Taking the ratio between these two simple equations and performing some algrebra yields an equation for the effective FRET radius above the gold NPs:

$$R_o^{\mathrm{NPs}} = \left(\frac{\bar{\Gamma}_{ET}^{\mathrm{NPs}}}{\bar{\Gamma}_{ET}^{\mathrm{glass}}}\right)^{1/6} \times R_o \tag{5.1}$$

Given the increase in the observed effective FRET rate of donor-acceptor mixtures on the gold NP films of 13.3 and our value of the FRET radius of the donor-acceptors in PMMA, we crudely estimate that the effective FRET radius has increased about 1.54×, increasing from 5.1 nm to 7.9 nm.

In FRET mixtures, donor emission kinetics display unique signatures of dimensionality that are easily observable [130, 143, 156]. It turns out, that in homogeneous ensembles of donors and acceptors that when the near-field Coulombic potential of the dipole-dipole interactions is spherically symmetric, as is the case within a dielectric, then donor emission decay trace takes on the simple analytical form

$$I_{DA}(t) \sim \exp(-\Gamma_D t - at^b), \tag{5.2}$$

where Γ_D is the spontaneous emission rate, a is a constant related to the FRET radius and the acceptor concentration, and b is a constant determined solely by the dimensionality of the interactions. In particular, for donor:acceptor mixtures in the bulk 3D $b \equiv 1/2$, while in 2D sheets $b \equiv 1/3$, and along lines $b \equiv 1/6$. The critical length scale here is the FRET radius R_o; for the mixture to behave as a 2D sheet, the thickness of the *slab* must be on the order of R_o. Similarly for a 1D line, the mixture must be confined in two dimensions on the order of R_o [156]. We emphasize that this constant b arises solely due to dimensional symmetry (1D, 2D or 3D) and due to the spherical symmetry of the near-field Coulomb potential in ensembles of random dipoles.

By dividing the normalized donor with acceptor decay trace in equation 5.2, by the normalized donor alone decay trace $I_D(t) \sim \exp(-\Gamma_D t)$ and taking the natural logarithm, we isolate the effect of the FRET in the decay function $h(t)$:

$$h(t) = -\log\left[I_{DA}(t)/I_D(t)\right] = at^b. \tag{5.3}$$

Figure 5.8 shows $h(t)$ for the three material systems, calculated from the data in figure 5.6. Note that the plot is in a log-log scale so that the exponent b containing dimensional information is easily discernible from the slope. We observe that in the case of FRET mixtures on glass and on a continuous gold film, the FRET interactions take place as though in a 3D bulk ($b = 1/2$). This is not unexpected. The 20 nm dye:PMMA films are roughly four times the FRET radius of 5.1 nm and there is thus no major symmetry breaking for the majority of the interacting dyes. This also suggests the dipole-dipole interaction potential remains spherically symmetric above the continuous thin gold film.

Meanwhile, in the case of the same thickness FRET mixture on our gold NP substrate, the interactions take place as though in a 2D sheet ($b = 1/3$). Here again the film thickness of the 20 nm dye:PMMA film is roughly two and half times larger than the estimated FRET radius of 7.8 nm; we therefore do not expect to see major 2D dimension confinement effects here! This $b = 1/3$ observation can then be explained in two ways: (1) our estimated FRET radius increase of 5.1 nm to 7.8 nm in the vicinity of the disordered gold NP is an underestimate, or (2) the gold NP film facilitates a near-field Coulombic potential that is no longer spherically symmetric but anisotropic, favoring interactions in planes parallel to the substrate. To verify either of these conjectures via theory requires a much more sophisticated electromagnetic model to capture the effects of gold NP enhancement on many-body FRET in the near-field of the disordered Au NP film. In any case, this result is interesting and will stimulate interest in engineering anisotropic resonant dipole-dipole interactions.

5.7 Conclusion

In conclusion, we have shown enhanced dipole-dipole interactions in the optical near-field of self-assembled disordered gold NP films enhance resonant dipole-dipole interactions. A 50% increase in the FRET radius of Alq3-R6G donor-acceptor pairs is observed. Since dipole-dipole interactions scale so rapidly in the near-field, this results in the observation of a thirteen times increase in the FRET rate relative to a glass or thin metal substrate. The increase in FRET rate is larger than the increase of the LDOS and we observe a 10% increase in FRET quantum efficiency relative to the same mixture on glass.

Motivated by these promising results, future work will investigate how the level of disorder in the resonant plasmonic films affects dipole-dipole interactions. Tuning the temperature and duration of the rapid annealing process results in different Au nanoparticle morphologies this may in turn be exploited to further enhance FRET.

From a strictly engineering standpoint, we predict that this increased range of dipole-dipole interactions on disordered gold nanoparticle substrates will lead to a simple solution for increased FRET interactions in bio-imaging.

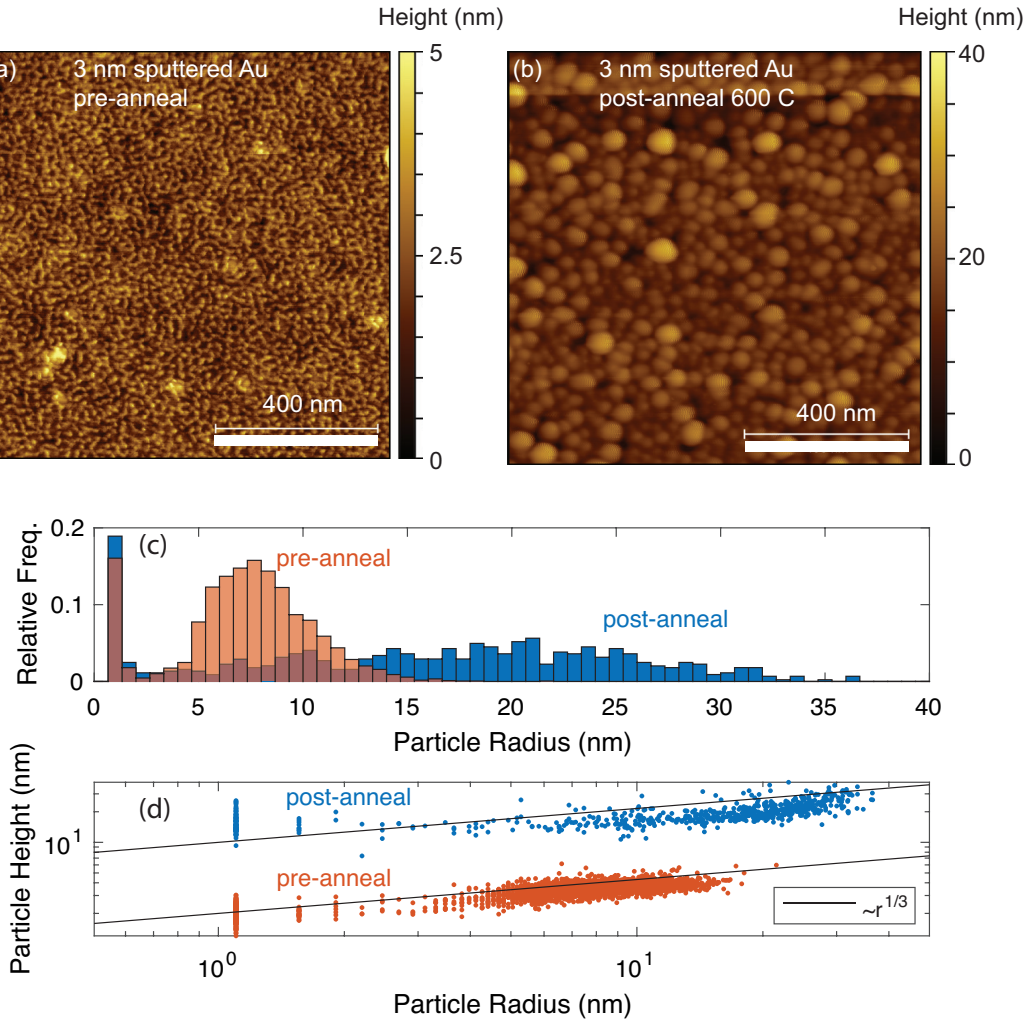

Fig. 5.1. Results of AFM measurements are shown. (a) Before annealing, the film is semi-continuous and composed of many small islands. (b) After annealing the gold islands have reflowed into larger more circular particles. If we assume the particles in both cases have a circular lateral cross section, and a half ellipsoidal top, then the islands/particle size statistics can be extracted. (c) The relative frequency of particle radius (assumed to have circular lateral shape) is increased upon annealing. (d) The measured particle height as a function of extracted particle radius reveals the NP heights increases an order of magnitude upon annealing. We note that the particle height is approximately proportional to the cube root of the particle radius; this purely empirical result indicates that the gold islands (pre-anneal) and gold particles (post-anneal) tend to have an island-like shape (height<lateral dimensions).

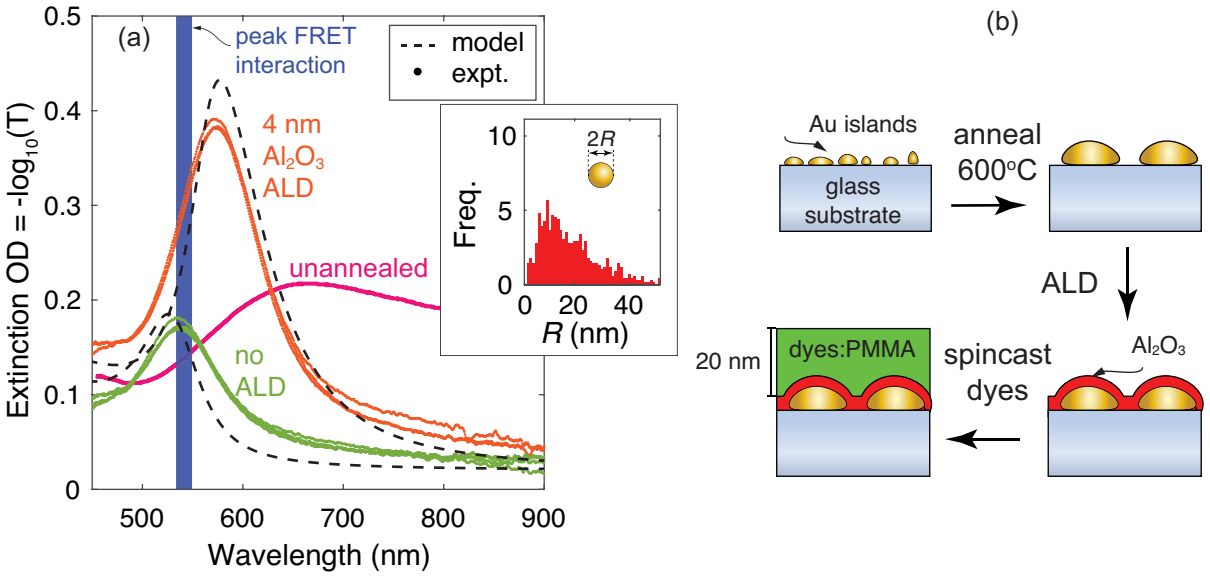

Fig. 5.2. (a) The extinction spectra reveals scattering and absorption losses at $\lambda \approx 530$ nm due to he presence of a LSP resonances in the annealed gold NP films (no ALD applied). The complex morphology of the unannealed gold film possesses low quality resonances over a broad spectral range and indicates the lack of strong plasmonic resonances. The additional ALD deposition of a conformal 4 nm Al_2O_3 layer shows the red-shifting and increase in quality of the LSP resonances (see main text for more details). The observed extinction is modeled reasonably well with Mie scattering theory for spherical Au NPs. In the model, an ensemble of Au NPs (extracted from experiment, inset right) is averaged to get the theory curve shown. The blue vertical band depicts the spectral location of the peak FRET interaction between Alq3 donors and R6G acceptors. (b) A schematic overview of the fabrication procedure is shown.

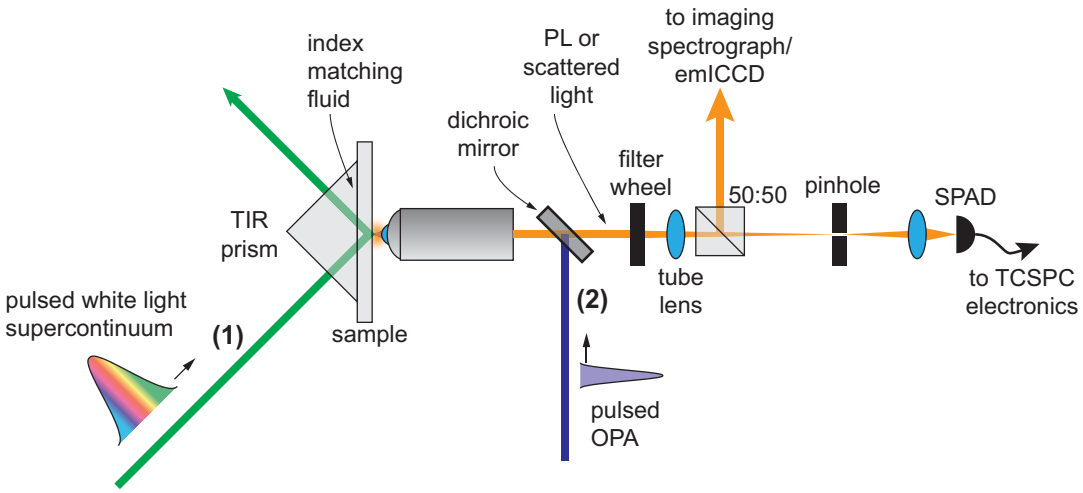

Fig. 5.3. The experimental schematic for a hybrid dark-field / fluorescence microscope is shown. (1) Pulsed white light undergoing total internal reflection reveals the position of resonant LSP particles via dark-field scattering microscopy. (2) At the same physical sample location, fluorescence emission, pumped via narrowband pulsed light, is collected in a confocal geometry. This fluorescence signal is then imaged via the imaging spectrograph. The fluorescence emission kinetics are also simultaneously measured via time-correlated single photon counting. A pin-hole is used to increase spatial resolution in this case. Details on the light sources can be found in appendix E.

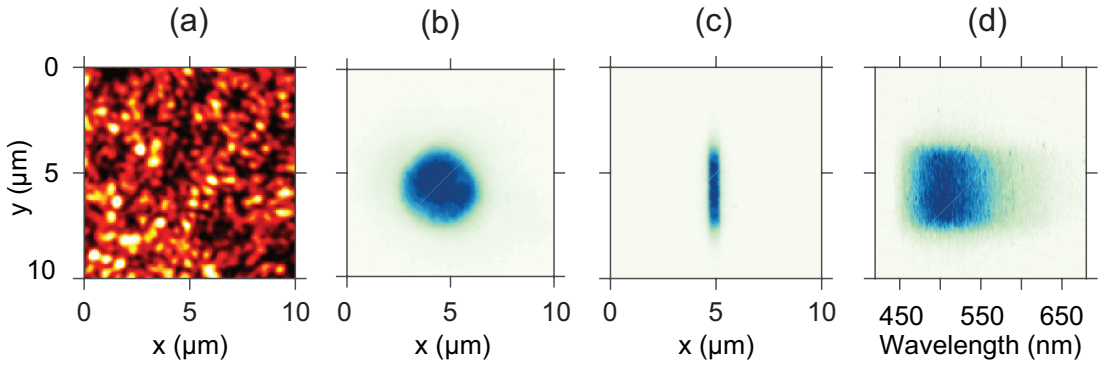

Fig. 5.4. (a) White light scattering image from gold nanoparticle film, pumped with white light continuum. (b) The corresponding fluorescence image is shown. For both (a,b) the imaging spectrograph slit is open and the grating is tilted such that the zeroth order diffraction illuminates the CCD, *i.e. dispersion off*. (c) The same fluorescence image as (b) is shown, except the spectrograph slit is closed. (d) The same image as (c) is shown, except the spectrograph grating has been tilted such that the first diffraction order illuminates the CCD, *i.e. dispersion on*. To obtain a 1D spectrum (signal vs wavelength) from the image shown in (d), we combine (sum/bin) the CCD counts in the y-direction.

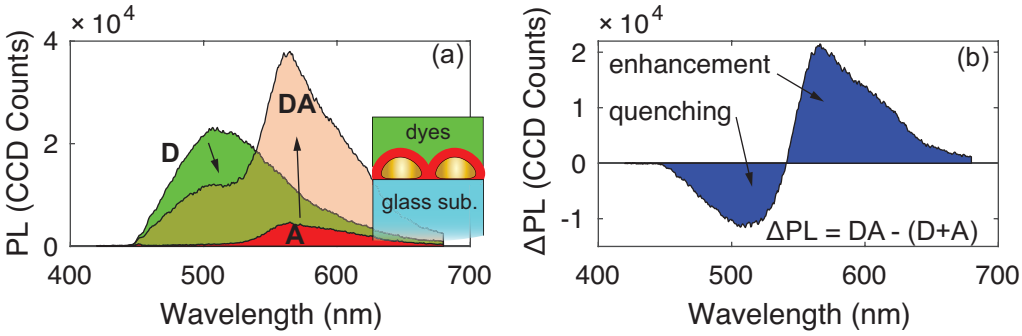

Fig. 5.5. (a) The spectra of dye:PMMA mixtures on top of the gold NPs are shown. The curves are labeld as follows: D = Alq3 donor alone, A = R6G acceptor alone, DA = donor and acceptor mixed with the same concentration as D and A alone. (b) The differential spectra $\Delta PL = DA - (D + A)$ reveals the quenching of the donor fluorecence and enhancement of the acceptor fluorescence.

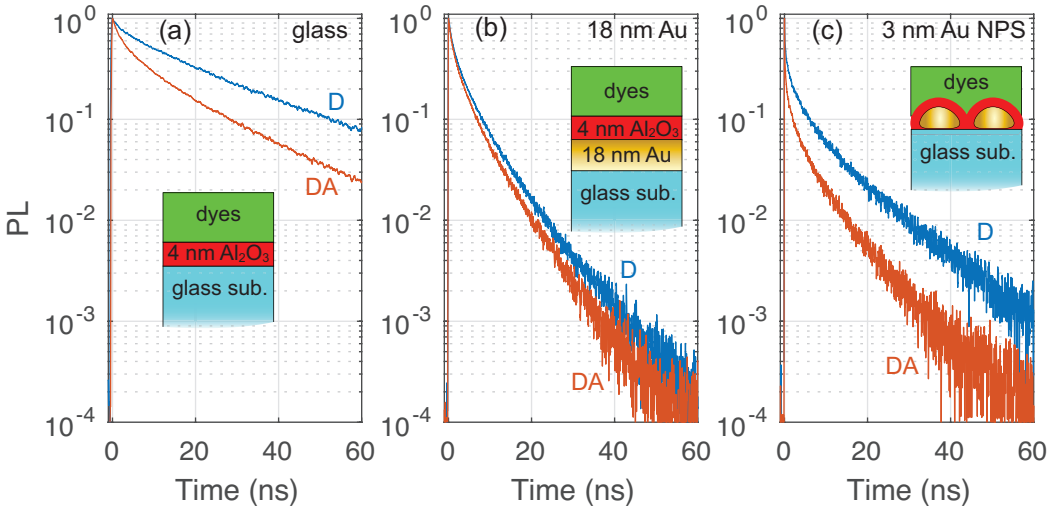

Fig. 5.6. The normalized donor fluorescence decay traces for donor only (D) and donor with acceptor (DA) samples are shown for three material systems: (a) on glass, (b) on 18 nm a continuous Au, and (c) on a gold NP film. All three material systems have a 4 nm continuous layer spacer of Al_2O_3 between the material system and the dyes. In all three material systems we see that the donor emission kinetics are more rapid when the acceptors are present due to FRET.

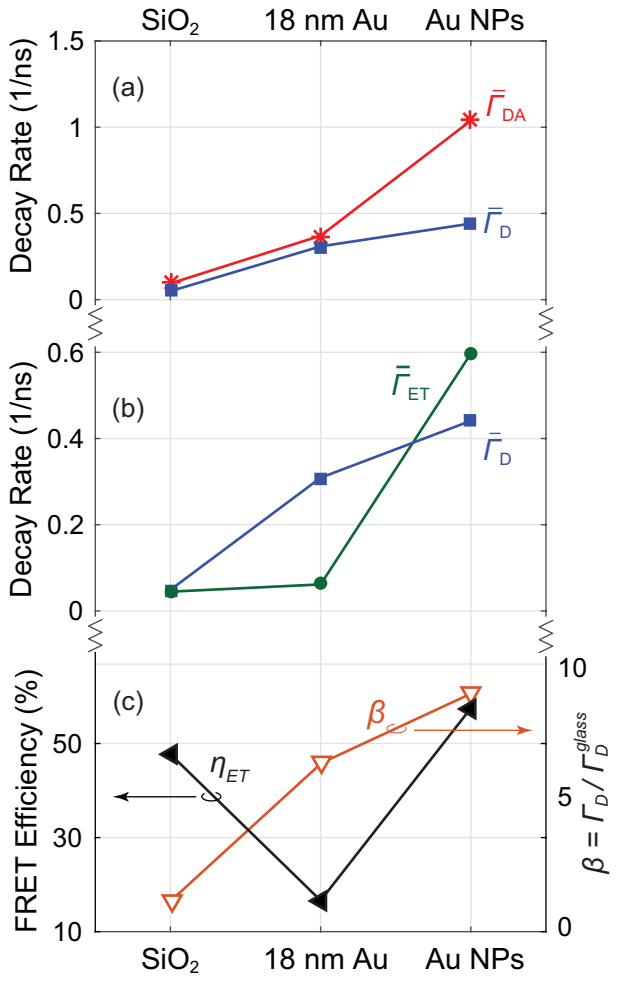

Fig. 5.7. (a) The effective donor decay rate $\bar{\Gamma}$ is plotted for the donor only (D) and donor with acceptor (DA) samples . (b) The effective FRET rate $\bar{\Gamma}_{ET} = \bar{\Gamma}_{DA} - \bar{\Gamma}_D$ is plotted alongside the effective donor only decay rate. (c) The FRET efficiency η_{ET} is plotted alongside the radiative decay rate enhancement β. For donors on the Au NP substrate, we observe a 13.3× increase in the effective FRET rate, outpacing the radiative decay rate enhancement of $\beta = 9$. As a result, the FRET efficiency, relative to glass has increased from 48% to 58%.

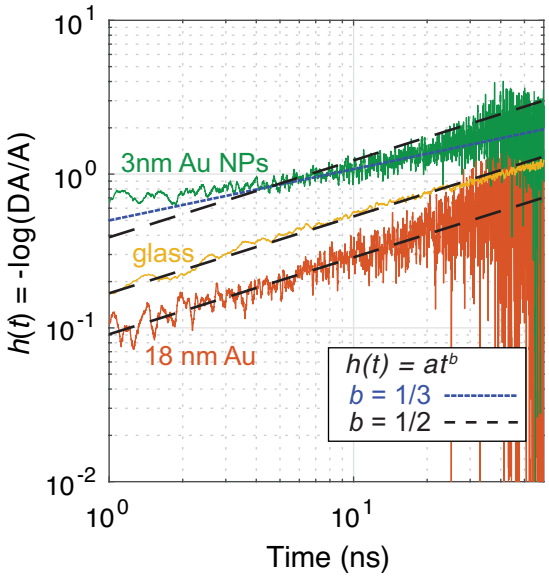

Fig. 5.8. The decay function $h(t) = -\log\left[I_{DA}(t)/I_D(t)\right]$ is shown for the three material systems. The dashed lines for the function at^b with $b = 1/2$ for 3D interactions and $b = 1/3$ for 2D interactions. On glass and 18 nm continuous Au, the 20 nm thick FRET mixtures are well approximated by a 3D ensemble with spherically symmetric dipole-dipole interaction potential. On the disordered Au NP substrate, however, the same thickness FRET mixture behaves as though in a 2D mixture. This indicates that the FRET radius has increased in the vicinity of the gold NP film or the dipole-dipole interaction potential is favoring interactions in the plane parallel to the substrate.

6. CONCLUSIONS AND FUTURE OUTLOOK

At the outset of this thesis work in 2010-2011, the main excitement surrounding metamaterials was their applications in super-resolution imaging and cloaking; the quantum and thermal aspects of these artificial media were just emerging. This thesis made important progress in the development of single photon sources and experimental verification of enhanced dipole-dipole interactions enabled by plasmonic metamaterials, and in particular hyperbolic metamaterials. We have made advances in nanofabrication of nanoscale metamaterials and ultrafast low-light level detection to verify the exotic classical and quantum optical properties of metamaterials. The two main contributions that we believe will have a long lasting impact in both fundamental science as well as in engineering applications are outlined below. Here, we also list the future directions of metamaterials and plasmonics research.

(1) we have provided the first experimental demonstration of the ability of hyperbolic metamaterials to extend the Coulombic near-field of dipole-dipole interactions to the far-field. This materials approach is non-resonant and fundamentally broadband, well suited for room-temperature solid-state dipole-dipole coupling, and therefore offers a paradigm shift in engineering long-range quantum interactions.

(2) We have utilized the broadband surface plasmon resonances supported by disordered gold nano-particle films to fundamentally enhance the Coulombic near-field dipole-dipole interactions in Forster Resonance Energy Transfer. In fact, the fluorescent emitter-emitter coupling strength exceeds the coupling of the individual emitters with the environment! This work then makes major progress to the long-standing goal of engineering emitter-emitter interactions (dipole-dipole coupling) beyond the coupling of the individual emitters with the photonic environment. Hitherto, other researchers had concluded that plasmonic resonances can only enhance or suppress dipole-dipole interactions by a factor of about 1.5. However, in our disordered gold

nanoparticle films, we observe an enhancement of dipole-dipole interaction strength by a factor of about 13! This work therefore stimulates further study of dipole-dipole coupling in the presence of disordered plasmonic films and also for the application of disordered plasmonic particle substrates for the application of bio-imaging.

This thesis work also made major experimental strides in ultrafast excitation and low light level detection techniques applied to nanofabricated metamaterials. On the one hand challenges were overcome for precise fabrication of thin film metamaterials as well as optical characterization using unique electromagnetic states such as Ferrel-Berreman modes. On the other hand ultrafast streak camera measurements as well as time- correlated single photon counting set-ups were built from the ground up, specifically to verify the super-Coulombic effect. This was a mammoth task to say the least but this thesis lays the foundation of long range dipole-dipole interactions at room temperature. This presents a new direction of research for the field which will hopefully pay dividends in scaling up nanoscale light sources and possibly enabling solid state room temperature quantum technologies. The experimental set-ups built during the thesis can now be advanced to the single photon detection regime with correlation set-ups.

The recent discovery and materials engineering refinement of natural hyperbolic media shows a promising direction of quantum optics in hyperbolic media. Van der Waals bonded meterials such as Hexagonal Boron Nitride, Bismuth Selenide/Telluride and Black phosphorus possess a natural hyperbolic dispersion in the near-infrared/optical and infrared spectral ranges [157–162]. In such materials, the curtailing of the hyperbolic mode dispersion is primarily due to intrinsic material losses and not the finite unit cell size[1]. Reduction in the intrinsic losses in these natural hyperbolic media and the design of appropriate quantum emitters in these frequency bands will no doubt result in a breakthroughs in room-temperature solid-state quantum optics and this

[1]Of course the finite unit cell of the atomic lattice will eventually curtail the complete divergence of the hyperbolic dispersion, however, this cut-off would be at spatial frequencies approximately 200× larger than current state of the art hyperbolic metamaterials.

prospect offers a rich field of exciting research in both fundamental science and in engineering for the foreseeable future.

Another interesting and brand-new prospect for quantum physics in hyperbolic media is in the application of entangled photon generation. Current entangled photon sources rely on spontaneous parametric down-conversion in $\chi^{(2)}$ crystals with uniaxial dielectric dispersion such as Beta Barium Borate (BBO) [12]. Although ultrabright sources of entangled photons have been generated and applied in a wide variety of quantum optics experiments, the inherently weak optical non-linearities and lack of strong spatial mode confinement in such crystals implies that the size of these entangled photon sources will always remain relatively large. Very recent work by the Atwater group at Caltech [163], as well as my own independent theoretical calculations (unpublished) shows that the designed non-linear response of plasmonic hyperbolic metamaterials may allow for a two-orders of magnitude enhancement in the brightness of entangled photon generation in devices with a truly nanoscale footprint! Moreover, the unique hyperbolic photonic mode dispersion allows the radiation pattern of entangled photons to be engineered and thus offers a paradigm shift in phase matching in optical parametric processes. We foresee that hyperbolic metamaterials may also find applications in chip-scale entangled photon generation.

REFERENCES

REFERENCES

[1] P. A. M. Dirac, "The Quantum Theory of the Emission and Absorption of Radiation," *Proceedings of the Royal Society of London A: Mathematical, Physical and Engineering Sciences*, vol. 114, no. 767, 1927.

[2] C. C. Gerry and P. L. Knight, *Introductory quantum optics*. Cambridge University Press, 2005.

[3] P. W. Milonni, *The quantum vacuum: an introduction to quantum electrodynamics*. Academic Press, 2013.

[4] L. Novotny and B. Hecht, *Principles of Nano-Optics*, 2nd ed. Cambridge University Press, 2012.

[5] E. M. Purcell, "B10. Spontaneous Emission Probabilities at Radio Frequencies," *Proceedings of the American Physical Society*, vol. 69, no. 11-12, p. 681, 1946.

[6] W. E. Lamb and R. C. Retherford, "Fine Structure of the Hydrogen Atom by a Microwave Method," *Physical Review*, vol. 72, no. 3, pp. 241–243, aug 1947.

[7] H. A. Bethe, "The Electromagnetic Shift of Energy Levels," *Physical Review*, vol. 72, no. 4, pp. 339–341, aug 1947.

[8] H. B. G. Casimir and D. Polder, "The Influence of Retardation on the London-van der Waals Forces," *Physical Review*, vol. 73, no. 4, pp. 360–372, feb 1948.

[9] T. Förster, "Zwischenmolekulare Energiewanderung und Fluoreszenz," *Annalen der Physik*, vol. 437, no. 1-2, pp. 55–75, 1948.

[10] J. P. Gordon, W. H. Louisell, and L. R. Walker, "Quantum Fluctuations and Noise in Parametric Processes. II," *Physical Review*, vol. 129, no. 1, pp. 481–485, jan 1963.

[11] W. H. Louisell, A. Yariv, and A. E. Siegman, "Quantum Fluctuations and Noise in Parametric Processes. I." *Physical Review*, vol. 124, no. 6, pp. 1646–1654, dec 1961.

[12] P. G. Kwiat, K. Mattle, H. Weinfurter, A. Zeilinger, A. V. Sergienko, and Y. Shih, "New High-Intensity Source of Polarization-Entangled Photon Pairs," *Physical Review Letters*, vol. 75, no. 24, pp. 4337–4341, dec 1995.

[13] C. Riek, D. V. Seletskiy, A. S. Moskalenko, J. F. Schmidt, P. Krauspe, S. Eckart, S. Eggert, G. Burkard, and A. Leitenstorfer, "Direct sampling of electric-field vacuum fluctuations," *Science*, 2015.

[14] C. Riek, P. Sulzer, M. Seeger, A. S. Moskalenko, G. Burkard, D. V. Seletskiy, and A. Leitenstorfer, "Subcycle quantum electrodynamics," *Nature*, vol. 541, no. 7637, pp. 376–379, jan 2017.

[15] D. L. Andrews, "Resonance energy transfer: theoretical foundations and developing applications," pp. 439–470, 2009.

[16] ——, "A unified theory of radiative and radiationless molecular energy transfer," *Chemical Physics*, vol. 135, no. 2, pp. 195–201, 1989.

[17] Z. Jacob, J. Y. Kim, G. V. Naik, A. Boltasseva, E. E. Narimanov, and V. M. Shalaev, "Engineering photonic density of states using metamaterials," *Applied Physics B*, vol. 100, no. 1, pp. 215–218, 2010.

[18] M. A. Noginov, H. Li, Y. A. Barnakov, D. Dryden, G. Nataraj, G. Zhu, C. E. Bonner, M. Mayy, Z. Jacob, and E. E. Narimanov, "Controlling spontaneous emission with metamaterials," *Optics Letters*, vol. 35, no. 11, p. 1863, 2010.

[19] W. D. Newman, C. L. Cortes, and Z. Jacob, "Enhanced and directional single-photon emission in hyperbolic metamaterials," *Journal of the Optical Society of America B*, vol. 30, no. 4, p. 766, mar 2013.

[20] B. Lounis and M. Orrit, "Single-photon sources," *Reports on Progress in Physics*, vol. 68, no. 5, pp. 1129–1179, 2005.

[21] T. M. Babinec, B. J. M. Hausmann, M. Khan, Y. Zhang, J. R. Maze, P. R. Hemmer, and M. Loncar, "A diamond nanowire single-photon source," *Nature Nanotechnology*, vol. 5, no. 3, pp. 195–199, 2010.

[22] J. T. Choy, B. J. M. Hausmann, T. M. Babinec, I. Bulu, M. Khan, P. Maletinsky, A. Yacoby, and M. Loncar, "Enhanced single-photon emission from a diamond-silver aperture." *Nature Photonics*, vol. 5, no. 12, pp. 738–743, 2011.

[23] K. G. Lee, X. W. Chen, H. Eghlidi, P. Kukura, R. Lettow, A. Renn, V. Sandoghdar, and S. Goetzinger, "A planar dielectric antenna for directional single-photon emission and near-unity collection efficiency," *Nature Photonics*, vol. 5, no. 3, pp. 166–169, 2011.

[24] R. Esteban, T. V. Teperik, and J. J. Greffet, "Optical patch antennas for single photon emission using surface plasmon resonances," *Physical Review Letters*, vol. 104, no. 2, p. 26802, 2010.

[25] D. E. Chang, A. S. Sørensen, P. R. Hemmer, and M. D. Lukin, "Quantum Optics with Surface Plasmons," *Physical Review Letters*, vol. 97, no. 5, p. 053002, 2006.

[26] D. Englund, B. Shields, K. Rivoire, F. Hatami, J. Vuckovic, H. Park, and M. D. Lukin, "Deterministic Coupling of a Single Nitrogen Vacancy Center to a Photonic Crystal Cavity," *Nano Letters*, vol. 10, no. 10, pp. 3922–3926, 2010.

[27] P. Grangier, B. Sanders, and J. Vuckovic, "Focus on Single Photons on Demand," *New Journal of Physics*, vol. 6, no. 1, jul 2004.

[28] I. Friedler, C. Sauvan, J. P. Hugonin, P. Lalanne, J. Claudon, and J. M. Gérard, "Solid-state single photon sources: the nanowire antenna," *Optics Express*, vol. 17, no. 4, p. 2095, 2009.

[29] A. F. Koenderink, "Plasmon Nanoparticle Array Waveguides for Single Photon and Single Plasmon Sources," *Nano Letters*, vol. 9, no. 12, pp. 4228–4233, 2009.

[30] D. Kleppner, "Inhibited Spontaneous Emission," *Physical Review Letters*, vol. 47, no. 4, pp. 233–236, jul 1981.

[31] G. Gabrielse and H. Dehmelt, "Observation of inhibited spontaneous emission," *Physical Review Letters*, vol. 55, no. 1, pp. 67–70, jul 1985.

[32] E. Yablonovitch, "Inhibited Spontaneous Emission in Solid-State Physics and Electronics," *Physical Review Letters*, vol. 58, no. 20, pp. 2059–2062, may 1987.

[33] R. G. Hulet, E. S. Hilfer, and D. Kleppner, "Inhibited Spontaneous Emission by a Rydberg Atom," *Physical Review Letters*, vol. 55, no. 20, pp. 2137–2140, nov 1985.

[34] C. Blum, N. Zijlstra, A. Lagendijk, M. Wubs, A. P. Mosk, V. Subramaniam, and W. L. Vos, "Nanophotonic Control of the Förster Resonance Energy Transfer Efficiency," *Physical Review Letters*, vol. 109, no. 20, p. 203601, 2012.

[35] A. F. Van Loo, A. Fedorov, K. Lalumière, B. C. Sanders, A. Blais, and A. Wallraff, "Photon-Mediated Interactions Between Distant Artificial Atoms," *Science*, vol. 342, no. 6165, pp. 1494–1496, 2013.

[36] A. Goban, C. L. Hung, J. D. Hood, S. P. Yu, J. A. Muniz, O. Painter, and H. J. Kimble, "Superradiance for Atoms Trapped along a Photonic Crystal Waveguide," *Physical Review Letters*, vol. 115, no. 6, p. 63601, aug 2015.

[37] M. Hübner, J. Kuhl, B. Grote, T. Stroucken, S. Haas, A. Knorr, S. W. Koch, G. Khitrova, and H. Gibbs, "Superradiant Coupling of Excitons in (In, Ga) As Multiple Quantum Wells," *Physica Status Solidi (b)*, vol. 206, no. 1, pp. 333–339, 1998.

[38] R. Röhlsberger, K. Schlage, B. Sahoo, S. Couet, and R. Rüffer, "Collective Lamb shift in single-photon superradiance," *Science*, vol. 328, no. 5983, pp. 1248–1251, 2010.

[39] P. Andrew and W. L. Barnes, "Forster Energy Transfer in an Optical Microcavity," *Science*, vol. 290, no. 5492, pp. 785–788, 2000.

[40] R. Landig, L. Hruby, N. Dogra, M. Landini, R. Mottl, T. Donner, and T. Esslinger, "Quantum phases from competing short- and long-range interactions in an optical lattice," *Nature*, vol. 532, no. 7600, pp. 476–479, 2016.

[41] A. Poddubny, I. Iorsh, P. Belov, and Y. Kivshar, "Hyperbolic metamaterials," *Nature Photonics*, vol. 7, no. 12, pp. 948–957, 2013.

[42] V. A. Podolskiy and E. E. Narimanov, "Strongly anisotropic waveguide as a nonmagnetic left-handed system," *Physical Review B*, vol. 71, no. 20, p. 201101, may 2005.

[43] Z. Jacob, L. V. Alekseyev, and E. Narimanov, "Optical Hyperlens: Far-field imaging beyond the diffraction limit," *Optics Express*, vol. 14, no. 18, p. 8247, 2006.

[44] Z. Liu, H. Lee, Y. Xiong, C. Sun, and X. Zhang, "Far-field optical hyperlens magnifying sub-diffraction-limited objects," *Science*, vol. 315, no. 5819, p. 1686, 2007.

[45] Z. Jacob and V. M. Shalaev, "Plasmonics Goes Quantum," *Science*, vol. 334, no. 6055, pp. 463–464, 2011.

[46] C. L. Cortes and Z. Jacob, "Super-Coulombic atomatom interactions in hyperbolic media," *Nature Communications*, vol. 8, no. 14144, 2017.

[47] G. W. Milton, R. C. McPhedran, and A. Sihvola, "The searchlight effect in hyperbolic materials," *Optics Express*, vol. 21, no. 12, pp. 14 926–14 942, 2013.

[48] R. A. Ferrell, "Predicted radiation of plasma oscillations in metal films," *Physical Review*, vol. 111, no. 5, pp. 1214–1222, 1958.

[49] D. W. Berreman, "Infrared absorption at longitudinal optic frequency in cubic crystal films." *Physical Review*, vol. 130, no. 6, pp. 2193–2198, 1963.

[50] T. Galfsky, H. N. S. Krishnamoorthy, W. Newman, E. E. Narimanov, Z. Jacob, and V. M. Menon, "Active hyperbolic metamaterials: enhanced spontaneous emission and light extraction," *Optica*, vol. 2, no. 1, p. 62, jan 2015.

[51] R. Starko-Bowes, J. Atkinson, W. Newman, H. Hu, T. Kallos, G. Palikaras, R. Fedosejevs, S. Pramanik, and Z. Jacob, "Optical characterization of epsilon-near-zero, epsilon-near-pole, and hyperbolic response in nanowire metamaterials," *Journal of the Optical Society of America B*, vol. 32, no. 10, pp. 2074–2080, 2015.

[52] A. V. Kabashin, P. Evans, S. Pastkovsky, W. Hendren, G. A. Wurtz, R. Atkinson, R. Pollard, V. A. Podolskiy, and A. V. Zayats, "Plasmonic nanorod metamaterials for biosensing," *Nature Materials*, vol. 8, no. 11, pp. 867–871, 2009.

[53] R. J. Pollard, A. Murphy, W. R. Hendren, P. R. Evans, R. Atkinson, G. A. Wurtz, A. V. Zayats, and V. A. Podolskiy, "Optical nonlocalities and additional waves in epsilon-near-zero metamaterials," *Physical Review Letters*, vol. 102, no. 12, p. 127405, 2009.

[54] G. A. Wurtz, R. Pollard, W. Hendren, G. P. Wiederrecht, D. J. Gosztola, V. A. Podolskiy, and A. V. Zayats, "Designed ultrafast optical nonlinearity in a plasmonic nanorod metamaterial enhanced by nonlocality," *Nature Nanotechnology*, vol. 6, no. 2, pp. 107–111, 2011.

[55] J. B. Pendry, "Negative refraction makes a perfect lens," *Physical Review Letters*, vol. 85, no. 18, pp. 3966–3969, oct 2000.

[56] X. Z. Nicholas Fang, Hyesog Lee, Cheng Sun, "SubDiffraction-Limited Optical Imaging with a Silver Superlens Nicholas," *Science*, vol. 308, no. 2005, pp. 534–537, 2005.

[57] J. B. Pendry, "Controlling Electromagnetic Fields," *Science*, vol. 312, no. 5781, pp. 1780–1782, 2006.

[58] N. I. Landy, S. Sajuyigbe, J. J. Mock, D. R. Smith, and W. J. Padilla, "Perfect metamaterial absorber," *Physical Review Letters*, vol. 100, no. 20, p. 207402, may 2008.

[59] W. Cai and V. Shalaev, *Optical metamaterials: Fundamentals and applications*. Spring-Verlag New York, 2010.

[60] V. G. Veselago, "The Electrodynamics of Substances with Simultaneously Negative Values Of epsilon and mu," *Soviet Physics Uspekhi*, vol. 10, no. 4, pp. 509–514, 1968.

[61] W. Cai, U. K. Chettiar, H.-K. Yuan, V. C. de Silva, A. V. Kildishev, V. P. Drachev, and V. M. Shalaev, "Metamagnetics with rainbow colors." *Optics express*, vol. 15, no. 6, pp. 3333–3341, 2007.

[62] N. Liu, H. Liu, S. Zhu, and H. Giessen, "Stereometamaterials," *Nature Photonics*, vol. 3, no. 3, pp. 157–162, mar 2009.

[63] E. Plum, X. X. Liu, V. A. Fedotov, Y. Chen, D. P. Tsai, and N. I. Zheludev, "Metamaterials: Optical activity without chirality," *Physical Review Letters*, vol. 102, no. 11, p. 113902, mar 2009.

[64] E. Plum, V. A. Fedotov, A. S. Schwanecke, N. I. Zheludev, and Y. Chen, "Giant optical gyrotropy due to electromagnetic coupling," *Applied Physics Letters*, vol. 90, no. 22, p. 223113, 2007.

[65] A. Alù, M. G. Silveirinha, A. Salandrino, and N. Engheta, "Epsilon-near-zero metamaterials and electromagnetic sources: Tailoring the radiation phase pattern," *Physical Review B*, vol. 75, no. 15, p. 155410, apr 2007.

[66] W. D. Newman, C. L. Cortes, J. Atkinson, S. Pramanik, R. G. Decorby, and Z. Jacob, "Ferrell-berreman modes in plasmonic epsilon-near-zero media," *ACS Photonics*, vol. 2, no. 1, pp. 2–7, 2015.

[67] X. Chen, B. I. Wu, J. A. Kong, and T. M. Grzegorczyk, "Retrieval of the effective constitutive parameters of bianisotropic metamaterials," *Physical Review E*, vol. 71, no. 4, p. 046610, apr 2005.

[68] J. Elser, V. A. Podolskiy, I. Salakhutdinov, and I. Avrutsky, "Nonlocal effects in effective-medium response of nanolayered metamaterials," *Applied Physics Letters*, vol. 90, no. 19, p. 191109, may 2007.

[69] X. Huang, Y. Lai, Z. H. Hang, H. Zheng, and C. T. Chan, "Dirac cones induced by accidental degeneracy in photonic crystals and zero-refractive-index materials." *Nature Materials*, vol. 10, no. 8, pp. 582–586, 2011.

[70] M. Silveirinha and N. Engheta, "Tunneling of Electromagnetic Energy through Subwavelength Channels and Bends using epsilon-Near-Zero Materials," *Physical Review Letters*, vol. 97, no. 15, p. 157403, oct 2006.

[71] A. Alù and N. Engheta, "Boosting Molecular Fluorescence with a Plasmonic Nanolauncher," *Physical Review Letters*, vol. 103, no. 4, p. 043902, jul 2009.

[72] E. J. R. Vesseur, T. Coenen, H. Caglayan, N. Engheta, and A. Polman, "Experimental Verification of n = 0 Structures for Visible Light," *Physical Review Letters*, vol. 110, no. 1, p. 013902, jan 2013.

[73] M. A. Kats, D. Sharma, J. Lin, P. Genevet, R. Blanchard, Z. Yang, M. M. Qazilbash, D. N. Basov, S. Ramanathan, and F. Capasso, "Ultra-thin perfect absorber employing a tunable phase change material," *Applied Physics Letters*, vol. 101, no. 22, p. 221101, nov 2012.

[74] L. V. Alekseyev, E. E. Narimanov, T. Tumkur, H. Li, Y. A. Barnakov, and M. A. Noginov, "Uniaxial epsilon-near-zero metamaterial for angular filtering and polarization control," *Applied Physics Letters*, vol. 97, no. 13, p. 131107, sep 2010.

[75] S. Molesky, C. J. Dewalt, and Z. Jacob, "High temperature epsilon-near-zero and epsilon-near-pole metamaterial emitters for thermophotovoltaics," *Optics Express*, vol. 21, no. S1, pp. A96–A110, 2013.

[76] D. Lee, M. F. Rubner, and R. E. Cohen, "All-Nanoparticle Thin-Film Coatings." *Nano Letters*, vol. 6, no. 10, pp. 2305–2312, 2006.

[77] N. Liu, T. Weiss, M. Mesch, L. Langguth, U. Eigenthaler, M. Hirscher, C. Sonnichsen, and H. Giessen, "Planar Metamaterial Analogue of Electromagnetically Induced Transparency for Plasmonic Sensing," *Nano Letters*, vol. 10, no. 4, pp. 1103–1107, apr 2010.

[78] A. Kubo, K. Onda, H. Petek, Z. Sun, Y. S. Jung, and H. K. Kim, "Femtosecond Imaging of Surface Plasmon Femtosecond Imaging of Surface Plasmon Dynamics in a Nanostructured Silver Film," *Nano Letters*, vol. 5, no. 6, pp. 1123–7, 2005.

[79] W. Wang, S. Wu, K. Reinhardt, Y. Lu, and S. Chen, "Broadband Light Absorption Enhancement in Thin-Film Silicon Solar Cells." *Nano Letters*, vol. 10, no. 6, pp. 2012–2018, 2010.

[80] M. Sukharev and T. Seideman, "Phase and Polarization Control as a Route to Plasmonic Nanodevices." *Nano Letters*, vol. 6, no. 4, pp. 715–719, 2006.

[81] R. Maas, J. Parsons, N. Engheta, and A. Polman, "Experimental realization of an epsilon-near-zero metamaterial at visible wavelengths." *Nature Photonics*, vol. 7, no. 11, pp. 907–912, 2013.

[82] A. Orlov, I. Iorsh, P. Belov, and Y. Kivshar, "Complex band structure of nanostructured metal-dielectric metamaterials," *Optics Express*, vol. 21, no. 2, p. 1593, jan 2013.

[83] A. A. Orlov, P. M. Voroshilov, P. A. Belov, and Y. S. Kivshar, "Engineered optical nonlocality in nanostructured metamaterials," *Physical Review B*, vol. 84, no. 4, p. 045424, jul 2011.

[84] A. V. Chebykin, A. A. Orlov, and P. A. Belov, "Validity range of model of effective medium for describing layered metal-dielectric nanostructured metamaterials." *Optics and Spectroscopy*, vol. 109, no. 6, pp. 938–950, 2010.

[85] A. V. Chebykin, A. A. Orlov, A. V. Vozianova, S. I. Maslovski, Y. S. Kivshar, and P. A. Belov, "Nonlocal effective medium model for multilayered metal-dielectric metamaterials," *Physical Review B*, vol. 84, no. 11, p. 115438, sep 2011.

[86] M. J. Bloemer and M. Scalora, "Transmissive properties of Ag/MgF2 photonic band gaps." *Applied Physics Letters*, vol. 72, no. 14, pp. 1676–1678, 1998.

[87] S. Vassant, A. Archambault, F. Marquier, F. Pardo, U. Gennser, A. Cavanna, J. L. Pelouard, and J. J. Greffet, "Epsilon-Near-Zero Mode for Active Optoelectronic Devices," *Physical Review Letters*, vol. 109, no. 23, p. 237401, dec 2012.

[88] S. Vassant, J.-P. Hugonin, F. Marquier, and J.-J. Greffet, "Berreman mode and epsilon near zero mode," *Optics Express*, vol. 20, no. 21, p. 23971, oct 2012.

[89] K. L. Kliewer and R. Fuchs, "Collective electronic motion in a metallic slab." *Physical Review*, vol. 153, no. 2, pp. 498–512, 1967.

[90] A. J. McAlister and E. A. Stern, "Plasma Resonance Absorption in Thin Metal Films," *Physical Review*, vol. 132, no. 4, pp. 1599–1602, nov 1963.

[91] J. Brambring and H. Raether, "Plasma radiation from thin silver foils excited by light." *Physical Review Letters*, vol. 15, no. 23, pp. 882–883, 1965.

[92] P. Tournois and V. Laude, "Negative group velocities in metal-film optical waveguides." *Optics Communications*, vol. 137, no. 1,2,3, pp. 41–45, 1997.

[93] I. Lindau and P. O. Nilsson, "Experimental verifiication of optically excited longitudinal plasmons." *Physica Scripta*, vol. 3, no. 2, pp. 87–92, 1971.

[94] C. Monat, B. Corcoran, M. Ebnali-Heidari, C. Grillet, B. J. Eggleton, T. P. White, L. O'Faolain, and T. F. Krauss, "Slow light enhancement of nonlinear effects in silicon engineered photonic crystal waveguides." *Optics Express*, vol. 17, no. 4, pp. 2944–2953, 2009.

[95] R. A. Ferrell and E. A. Stern, "Plasma Resonance in the Electrodynamics of Metal Films," *American Journal of Physics*, vol. 30, no. 11, pp. 810–812, nov 1962.

[96] M. A. Nielsen and I. L. Chuang, *Quantum computation and quantum information*. Cambridge University Press, 2010.

[97] E. Altewischer, E. M. P. Van, and J. P. Woerdman, "Plasmon-assisted transmission of entangled photons," *Nature*, vol. 418, no. 6895, pp. 304–306, 2002.

[98] A. Huck, S. Smolka, P. Lodahl, A. S. Sørensen, A. Boltasseva, J. Janousek, and U. L. Andersen, "Demonstration of Quadrature-Squeezed Surface Plasmons in a Gold Waveguide," *Physical Review Letters*, vol. 102, no. 24, p. 246802, jun 2009.

[99] G. Di Martino, Y. Sonnefraud, S. Kéna-Cohen, M. Tame, . K. Özdemir, M. S. Kim, and S. A. Maier, "Quantum statistics of surface plasmon polaritons in metallic stripe waveguides," *Nano Letters*, vol. 12, no. 5, pp. 2504–2508, 2012.

[100] Z. Jacob, "Quantum plasmonics," *MRS Bulletin*, vol. 37, no. 08, pp. 761–767, 2012.

[101] I. Aharonovich, A. D. Greentree, and S. Prawer, "Diamond photonics." *Nature Photonics*, vol. 5, no. 7, pp. 397–405, 2011.

[102] A. Huck, S. Kumar, A. Shakoor, and U. L. Andersen, "Controlled Coupling of a Single Nitrogen-Vacancy Center to a Silver Nanowire," *Physical Review Letters*, vol. 106, no. 9, p. 096801, feb 2011.

[103] K. Tanaka, E. Plum, J. Y. Ou, T. Uchino, and N. I. Zheludev, "Multifold enhancement of quantum dot luminescence in plasmonic metamaterials," *Physical Review Letters*, vol. 105, no. 22, p. 227403, 2010.

[104] G. W. Ford and W. H. Weber, "Electromagnetic interactions of molecules with metal surfaces," *Physics Reports*, vol. 113, no. 4, pp. 195–287, 1984.

[105] G. Sun, J. B. Khurgin, and R. A. Soref, "Practicable enhancement of spontaneous emission using surface plasmons," *Applied Physics Letters*, vol. 90, p. 111107, 2007.

[106] Y. Xiong, Z. Liu, C. Sun, and X. Zhang, "Two-Dimensional Imaging by Far-Field Superlens at Visible Wavelengths," *Nano Letters*, vol. 7, no. 11, pp. 3360–3365, 2007.

[107] D. R. Smith, D. Schurig, J. J. Mock, P. Kolinko, and P. Rye, "Partial focusing of radiation by a slab of indefinite media," *Applied Physics Letters*, vol. 84, no. 13, pp. 2244–2246, 2004.

[108] R. K. Fisher and R. W. Gould, "Resonance Cones in the Field Pattern of a Short Antenna in an Anisotropic Plasma," *Physical Review Letters*, vol. 22, no. 21, pp. 1093–1095, may 1969.

[109] L. B. Felsen and N. Marcuvitz, *Radiation and scattering of waves*. IEEE Press, 1994.

[110] K. Balmain, A. Luttgen, and P. Kremer, "Resonance cone formation, reflection, refraction, and focusing in a planar anisotropic metamaterial," *IEEE Antennas and Wireless Propagation Letters*, vol. 1, no. 1, pp. 146–149, 2002.

[111] I. Iorsh, A. Poddubny, A. Orlov, P. Belov, and Y. S. Kivshar, "Spontaneous emission enhancement in metal-dielectric metamaterials," *Physics Letters A*, vol. 376, no. 3, pp. 185–187, 2012.

[112] C. L. Cortes, W. Newman, S. Molesky, and Z. Jacob, "Quantum nanophotonics using hyperbolic metamaterials," *Journal of Optics*, vol. 14, no. 6, p. 63001, jun 2012.

[113] K. J. Russell, T.-L. Liu, S. Cui, and E. L. Hu, "Large spontaneous emission enhancement in plasmonic nanocavities," *Nature Photonics*, vol. 6, no. 7, pp. 459–462, 2012.

[114] Y. C. Jun, R. Pala, and M. L. Brongersma, "Strong Modification of Quantum Dot Spontaneous Emission via Gap Plasmon Coupling in Metal Nanoslits," *Journal of Physical Chemistry C*, vol. 114, no. 16, pp. 7269–7273, 2010.

[115] P. Yao, C. Van Vlack, A. Reza, M. Patterson, M. M. Dignam, and S. Hughes, "Ultrahigh Purcell factors and Lamb shifts in slow-light metamaterial waveguides," *Physical Review B*, vol. 80, no. 19, p. 195106, nov 2009.

[116] Q. Quan, I. Bulu, and M. Lončar, "Broadband waveguide QED system on a chip," *Physical Review A*, vol. 80, no. 1, p. 011810, jul 2009.

[117] P. B. Johnson and R. W. Christy, "Optical constants of the noble metals," *Physical Review B*, vol. 6, no. 12, pp. 4370–4379, 1972.

[118] X. Ni, Z. Liu, and A. V. Kildishev, "PhotonicsDB: Optical Constants."

[119] H. N. S. Krishnamoorthy, Z. Jacob, E. Narimanov, I. Kretzschmar, and V. M. Menon, "Topological Transitions in Metamaterials," *Science*, vol. 336, no. 6078, pp. 205–209, 2012.

[120] H. J. Lezec, A. Degiron, E. Devaux, R. A. Linke, L. Martin-Moreno, F. J. Garcia-Vidal, and T. W. Ebbesen, "Beaming light from a subwavelength aperture," *Science*, vol. 297, no. 5582, pp. 820–822, 2002.

[121] N. P. de Leon, B. J. Shields, C. L. Yu, D. E. Englund, A. V. Akimov, M. D. Lukin, and H. Park, "Tailoring Light-Matter Interaction with a Nanoscale Plasmon Resonator," *Physical Review Letters*, vol. 108, no. 22, p. 226803, may 2012.

[122] J.-S. Bouillard, S. Vilain, W. Dickson, G. A. Wurtz, and A. V. Zayats, "Broadband and broadangle SPP antennas based on plasmonic crystals with linear chirp," *Scientific Reports*, vol. 2, no. 1, p. 829, nov 2012.

[123] Q. Gan and F. J. Bartoli, "Surface dispersion engineering of planar plasmonic chirped grating for complete visible rainbow trapping," *Applied Physics Letters*, vol. 98, no. 25, p. 251103, jun 2011.

[124] W. Chen, M. D. Thoreson, S. Ishii, A. V. Kildishev, and V. M. Shalaev, "Ultra-thin ultra-smooth and low-loss silver films on a germanium wetting layer," *Optics Express*, vol. 18, no. 5, p. 5124, mar 2010.

[125] G.-I. Kweon and N. M. Lawandy, "Resonance Dipole-dipole Interaction in Electromagnetically Confined Geometries," *Journal of Modern Optics*, vol. 41, no. 2, pp. 311–323, feb 1994.

[126] J. S. Douglas, H. Habibian, C.-L. Hung, A. V. Gorshkov, H. J. Kimble, and D. E. Chang, "Quantum many-body models with cold atoms coupled to photonic crystals," *Nature Photonics*, vol. 9, no. 5, pp. 326–331, 2015.

[127] E. Shahmoon and G. Kurizki, "Nonradiative interaction and entanglement between distant atoms," *Physical Review A*, vol. 87, no. 3, p. 33831, 2013.

[128] R. Sokhoyan and H. A. Atwater, "Quantum optical properties of a dipole emitter coupled to an epsilon-near-zero nanoscale waveguide," *Optics Express*, vol. 21, no. 26, p. 32279, 2013.

[129] D. Martin-Cano, L. Martin-Moreno, F. J. Garcia-Vidal, and E. Moreno, "Resonance Energy Transfer and Superrradiance Mediated by Plasmonic Nanowaveguides," *Nano Letters*, vol. 10, no. 8, pp. 3129–3134, 2010.

[130] J. R. Lakowicz, *Principles of Fluorescence Spectroscopy*, 2nd ed. New York: Springer, 2004.

[131] S. Bidault, A. Devilez, P. Ghenuche, B. Stout, N. Bonod, and J. Wenger, "Competition between Förster Resonance Energy Transfer and Donor Photodynamics in Plasmonic Dimer Nanoantennas," *ACS Photonics*, vol. 3, no. 5, pp. 895–903, 2016.

[132] R. R. Chance, A. Prock, and R. Silbey, "Molecular fluorescence and energy transfer near interfaces," *Advances in Chemical Physics*, vol. 37, pp. 1–65, 1978.

[133] P. Andrew and W. L. Barnes, "Energy transfer across a metal film mediated by surface plasmon polaritons," *Science*, vol. 306, no. 5698, pp. 1002–1005, 2004.

[134] M. Scheibner, T. Schmidt, L. Worschech, A. Forchel, G. Bacher, T. Passow, and D. Hommel, "Superradiance of quantum dots," *Nature Physics*, vol. 3, no. 2, pp. 106–110, 2007.

[135] C. van Ditzhuijzen, A. Koenderink, J. Hernández, F. Robicheaux, L. Noordam, and H. van den Heuvell, "Spatially Resolved Observation of Dipole-Dipole Interaction between Rydberg Atoms," *Physical Review Letters*, vol. 100, no. 24, p. 243201, 2008.

[136] Z. Ficek and R. Tanaś, "Delayed sudden birth of entanglement," *Physical Review A*, vol. 77, no. 5, p. 54301, 2008.

[137] G. D. Scholes, "Quantum-coherent electronic energy transfer: Did nature think of it first?" *The Journal of Physical Chemistry Letters*, vol. 1, no. 1, pp. 2–8, 2010.

[138] S. Ravets, H. Labuhn, D. Barredo, L. Béguin, T. Lahaye, and A. Browaeys, "Coherent dipole-dipole coupling between two single rydberg atoms at an electrically-tuned forster resonance," *Nature Physics*, vol. 10, no. 12, pp. 914–917, 2014.

[139] P. C. Ray, Z. Fan, R. A. Crouch, S. S. Sinha, and A. Pramanik, "Nanoscopic optical rulers beyond the FRET distance limit: fundamentals and applications," *Chemical Society Reviews*, vol. 43, no. 17, pp. 6370–6404, 2014.

[140] S. A. Maier, *Plasmonics: Fundamentals and Applications*, 1st ed. Springer, 2007.

[141] T. Zhai, X. Zhang, Z. Pang, X. Su, H. Liu, S. Feng, and L. Wang, "Random Laser Based on Waveguided Plasmonic Gain Channels," *Nano Letters*, vol. 11, no. 10, pp. 4295–4298, oct 2011.

[142] T. Zhai, Z. Xu, S. Li, and X. Zhang, "Red-green-blue plasmonic random laser," *Optics Express*, vol. 25, no. 3, pp. 2100–2106, 2017.

[143] T. U. Tumkur, J. K. Kitur, C. E. Bonner, A. N. Poddubny, E. E. Narimanov, and M. A. Noginov, "Control of Förster energy transfer in the vicinity of metallic surfaces and hyperbolic metamaterials," *Faraday Discussions*, vol. 178, pp. 395–412, 2015.

[144] G. Mie, "Contributions to the optics of turbid media, particularly of colloidal metal solutions," *Annalen der Physik*, vol. 25, no. 3, pp. 377–445, 1908.

[145] M. A. Noginov, G. Zhu, A. M. Belgrave, R. Bakker, V. M. Shalaev, E. E. Narimanov, S. Stout, E. Herz, T. Suteewong, and U. Wiesner, "Demonstration of a spaser-based nanolaser," *Nature*, vol. 460, no. 7259, pp. 1110–1112, aug 2009.

[146] J.-M. Nam, J.-W. Oh, H. Lee, and Y. D. Suh, "Plasmonic Nanogap-Enhanced Raman Scattering with Nanoparticles," *Accounts of Chemical Research*, vol. 49, no. 12, pp. 2746–2755, dec 2016.

[147] T. Ellenbogen, K. Seo, and K. B. Crozier, "Chromatic plasmonic polarizers for active visible color filtering and polarimetry," *Nano Letters*, vol. 12, no. 2, pp. 1026–1031, 2012.

[148] S. J. Tan, L. Zhang, D. Zhu, X. M. Goh, Y. M. Wang, K. Kumar, C.-W. Qiu, and J. K. W. Yang, "Plasmonic color palettes for photorealistic printing with aluminum nanostructures," *Nano Letters*, vol. 14, no. 7, pp. 4023–4029, 2014.

[149] J. Zhang, Y. Fu, and J. R. Lakowicz, "Enhanced Förster Resonance Energy Transfer (FRET) on a Single Metal Particle," *The Journal of Physical Chemistry C*, vol. 111, no. 1, pp. 50–56, 2007.

[150] J. Zhang, Y. Fu, M. H. Chowdhury, and J. R. Lakowicz, "Enhanced Förster Resonance Energy Transfer on Single Metal Particle. 2. Dependence on DonorAcceptor Separation Distance, Particle Size, and Distance from Metal Surface," *The Journal of Physical Chemistry C*, vol. 111, no. 32, pp. 11 784–11 792, 2007.

[151] S. A. Campbell, *Fabrication Engineering at the Micro- and Nanoscale*. Oxford University Press, 2012.

[152] D. J. Bergman and D. Stroud, "Physical Properties of Macroscopically Inhomogeneous Media," H. EHRENREICH and D. B. T. S. S. P. TURNBULL, Eds. Academic Press, 1992, vol. 46, no. Supplement C, pp. 147–269.

[153] A. L. Efros and B. I. Shklovskii, "Critical Behaviour of Conductivity and Dielectric Constant near the Metal-Non-Metal Transition Threshold," *physica status solidi (b)*, vol. 76, no. 2, pp. 475–485, 1976.

[154] A. N. Poddubny, "Collective Forster energy transfer modified by a planar metallic mirror," *Physical Review B*, vol. 92, no. 15, p. 155418, 2015.

[155] A. K. Boddeti, R. Kumar, and S. Mujumdar, "Figures-of-merit of Anderson localization cavities in membrane-based periodic-on-average random templates," *Optics Communications*, vol. 397, no. April, pp. 39–43, 2017.

[156] L. Klushin and O. Tcherkasskaya, "Effects of molecular distribution on the fluorescence transfer: Exact results for slab geometry," *Journal of Chemical Physics*, vol. 119, no. 6, pp. 3421–3428, 2003.

[157] J. Qiao, X. Kong, Z.-X. Hu, F. Yang, and W. Ji, "High-mobility transport anisotropy and linear dichroism in few-layer black phosphorus," *Nature Communications*, vol. 5, p. 4475, jul 2014.

[158] H. O. H. Churchill and P. Jarillo-Herrero, "Two-dimensional crystals: Phosphorus joins the family," *Nature Nanotechnology*, vol. 9, no. 5, pp. 330–331, may 2014.

[159] M. Esslinger, R. Vogelgesang, N. Talebi, W. Khunsin, P. Gehring, S. de Zuani, B. Gompf, and K. Kern, "Tetradymites as Natural Hyperbolic Materials for the Near-Infrared to Visible," *ACS Photonics*, vol. 1, no. 12, pp. 1285–1289, dec 2014.

[160] D. N. Basov, M. M. Fogler, and F. J. G. de Abajo, "Polaritons in van der Waals materials," *Science*, vol. 354, no. 6309, p. aag1992, 2016.

[161] S. Dai, Q. Ma, M. K. Liu, T. Andersen, Z. Fei, M. D. Goldflam, M. Wagner, K. Watanabe, T. Taniguchi, and M. Thiemens, "Graphene on hexagonal boron nitride as a tunable hyperbolic metamaterial," *Nature Nanotechnology*, vol. 10, no. 8, pp. 682–686, 2015.

[162] S. Dai, Q. Ma, T. Andersen, A. S. Mcleod, Z. Fei, M. K. Liu, M. Wagner, K. Watanabe, T. Taniguchi, M. Thiemens, F. Keilmann, P. Jarillo-Herrero, M. M. Fogler, and D. N. Basov, "Subdiffractional focusing and guiding of polaritonic rays in a natural hyperbolic material," *Nature Communications*, vol. 6, p. 6963, apr 2015.

[163] A. Davoyan and H. Atwater, "Tailoring Spontaneous Parametric Downconversion in Hyperbolic Metamaterials," in *Conference on Lasers and Electro-Optics*, ser. OSA Technical Digest (online). San Jose, California: Optical Society of America, 2016, p. FW1B.2.

[164] H. Fujiwara, *Spectroscopic Ellipsometry*. Chichester, UK: John Wiley & Sons, Ltd, jan 2007.

[165] D. Garbuzov, V. Bulović, P. Burrows, and S. Forrest, "Photoluminescence efficiency and absorption of aluminum-tris-quinolate (Alq3) thin films," *Chemical Physics Letters*, vol. 249, no. 5-6, pp. 433–437, feb 1996.

[166] W. Becker, *Advanced Time-Correlated Single Photon Counting Techniques*. Springer, Berlin, Heidelberg, 2005, vol. 81.

[167] H. Raether, *Surface Plasmons on Smooth and Rough Surfaces and on Gratings*. Springer, Berlin, Heidelberg, 1988.

[168] G. R. Fowles, *Introduction to modern optics*. Dover Publications, 1989.

[169] E. Hecht, *Optics*, 4th ed. Pearson, 2014.

[170] P. G. Etchegoin, E. C. Le Ru, and M. Meyer, "An analytic model for the optical properties of gold," *The Journal of Chemical Physics*, vol. 125, no. 16, p. 164705, 2006.

[171] R. Boyd, *Nonlinear Optics*, 3rd ed. Burlington: Academic Press, 2008.

APPENDICES

A. FABRICATION, CHARACTERIZATION AND MEASUREMENTS OF EPSILON NEAR ZERO METAMATERIALS

A.1 Fabrication

Silver and silica multilayer films were deposited using electron beam evaporation on BK7 glass microscope slides. A 40 nm wetting layer of silica was deposited onto the substrate to help remove initial surface roughness. The silver and silica multilayers were then deposited and capped with a top 40 nm layer of silica to help prevent oxidation of the silver films. Film thicknesses were verified through `JEOL 6301F` scanning electron microscope micrographs. RMS surface roughness was measured with an `Alpha-Step IQ` contact profilometer and was estimated to be between 1-2 nm for all layers.

A.2 Determining Optical Constants

Optical constants of individual silica and silver films were determined via ellipsometry using a `JA Woollam VASE` ellipsometer and the inferred optical constants showed good agreement with literature [117, 124]. We modeled the dielectric permittivity function of silver as $\epsilon_{Ag} \approx \epsilon_{FC} + \epsilon_{bound}$, with ϵ_{FC} being the contribution from the free carriers and ϵ_{bound} being the contribution of bound or valence electrons. Free electron motion in the silver is treated with a Drude dispersion while interband

transition of bound electrons in the UV are modeled with five Lorentz osscillators as described by Chen et al [124, 164]:

$$\epsilon_{fc} \approx \epsilon_{drude} = 1 - \frac{\omega_p^2}{\omega^2 + i\omega/\tau} \tag{A.1}$$

$$\epsilon_{bound} \approx \epsilon_{bg} + \sum_{n=1}^{5} \epsilon_{lorentz} = \epsilon_{bg} + \sum_{n=1}^{5} \left(\frac{A_n \omega_n^2}{\omega_n^2 - \omega^2 - i\omega/\tau_n} \right). \tag{A.2}$$

ω_p is the plasma frequency of the metal, τ is the free electron scattering time, ω_n is the n^{th} interband transition frequency, τ_n is the dissipation time of the interband excitation, and A_n is the amplitude of the interband excitation. ϵ_{bg} represents a background dielectric constant from the metal's core-shell electrons. Figure A.1 shows the experimentally determined dielectric permittivity of a 100 nm thick silver foil on a glass microscope slide substrate.

The amorphous silica layers are modelled using Sellmeier's equation with an Urbach absorption tail. The real part of the refractive index is defined with Sellmeier's equation while the extinction coefficient is treated with a exponential absorption tail with an onset ≈ 330 nm. It is important to note that this model does not satisfy the Kramers-Kronig relation but does acurrately model the dielectric function of amorphous silica in the near-UV to infrared range. A more complete, physically reasonable description of the optical response of silica can be achieved with a Tauc-Lorentz model; see page 170 of [164].

A.3 Transmission Measurements

Optical and UV transmission measurements were taken using a `Perkin-Elmer Lambda900 IR-UV` spectrophotometer equipped with a UV polarizer ($\lambda = 300 - 400$ nm) and an IR polarizer ($\lambda = 400 - 800$ nm). Baseline measurements indicate that the precision of transmission measurements is $\pm 0.2 - \pm 0.4\%$. The precision of the Spectrophotometer is minimized by using longer detector intergration times and by allowing the source lamp to warm-up and stabilize for $\approx 30 - 60$ min.

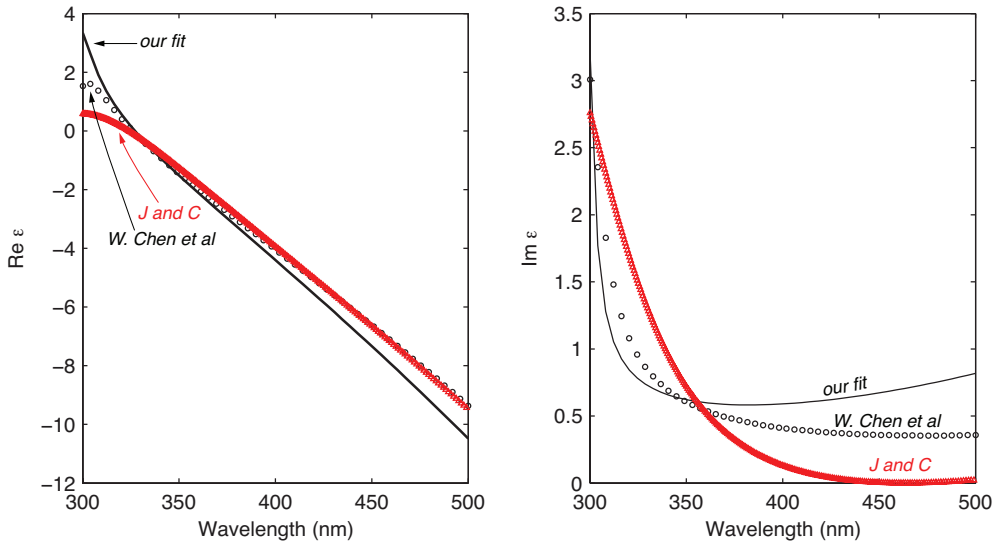

Fig. A.1. Dielectric permittivity for a 100 nm thick silver foil as determined by ellipsometry.

B. PHOTONIC BAND-STRUCTURE OF HYPERBOLIC METAMATERIALS

B.1 Dielectric Tensor for silver/silica multilayer superlattices

This section shows the real and imaginary (lossy) components of the effective medium, metamaterial dielectric permittivity tensor for the three silver/silica multilayer samples in our experiment. The dielectric permittivity tensor is computed using zeroth order Maxwell-Garnett effective medium theory and yields $\bar{\bar{\epsilon}}_{eff} = \mathrm{diag}[\epsilon_{||}, \epsilon_{||}, \epsilon_{\perp}]$ where $\epsilon_{||} = \rho\epsilon_m + (1-\rho)\epsilon_d$ is the dielectric permittivity for polarizations along the interfaces of the multilayer and $\epsilon_{\perp} = (\rho/\epsilon_m + (1-\rho)/\epsilon_d)^{-1}$ is the dielectric permittivity for polarizations perpendicular to the interfaces of the multilayer. ϵ_m is the silver permittivity and ϵ_d is the permittivity of the silica. ρ is the metal volume filling fraction.

Figure B.1 shows the full metamaterial dielectric permittivity tensor for multilayer samples with silver film thicknesses of 20 nm and silica film thicknesses of 20 nm ($\rho = 0.5$), 30 nm ($\rho = 0.4$), and 40 nm ($\rho = 0.33$). The individual permittivity tensor components of the silver/silica multilayer-based metamaterials exhibit nothing remarkable at the ENZ of the constituent silver films which occurs at a wavelength of $\lambda = 326$ nm. This reinforces the fact that complex propagation constant $k_{\perp}$ reveals underlying modal resonances of the metamaterial which can not be ascertained by examining the effective permittivity tensor alone.

B.2 Modal Analysis - Finding the poles of the reflection coefficient r_p

A mode supported by a particular structure can be characterized by a unique spectral frequency ω (or free space wavelength λ) and a spatial wavevector $\vec{k}$. These

modes are manifested as poles of the structure's response function, which for planar structures is the reflection (or transmission) coefficient. The reflection and transmission coefficients have poles at the same locations and are thus equal candidates for finding the modes. For a fixed wavelength λ the reflection coefficient of a planar structure can be completely specified by the transverse wavevector $k_{\|}$. The energy-momentum (energy-wave vector) dispersion of a mode is then described by a path in the frequency-wavevector space, and at every point along this path, the reflection coefficient has a pole or equivalently, the inverse of the reflection coefficient has a zero.

To determine the dispersion of modes supported by planar structures, we seek all the zeros (local minima) of the function $\alpha(k_{\|}) = 1/r_p(k_{\|})$ in the complex plane

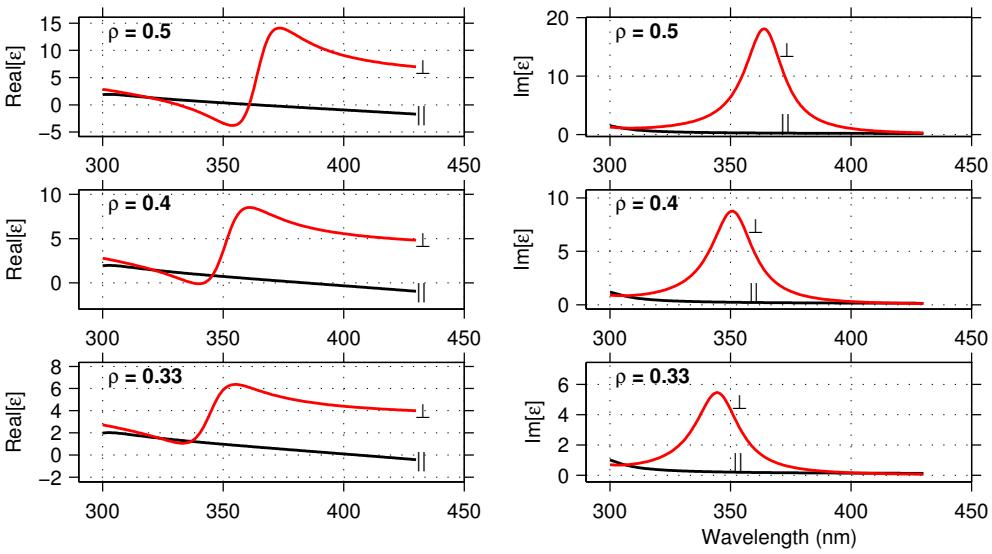

Fig. B.1. The real and imaginary part of the dielectric permittivity tensor for silver/silica superlattices is shown for various silver volume filling fractions. The ENZ in the parallel direction is red-shifted with decreasing silver filling fraction while the ENP in the perpendicular direction is blue-shifted with decreasing silver filling fraction. The dielectric tensor shows no remarkable features in the real or imaginary parts at the ENZ of the consituent silver ($\lambda \approx 326$ nm).

of $k_\parallel = k'_\parallel + ik''_\parallel$, and perform this search iteratively at a series of wavelengths λ. An optimized transfer matrix method is used to calculate the reflection coefficient, while the minimum of the function $\alpha(k_\parallel)$ is determined with the built-in MATLAB function `fminsearch`. This built-in MATLAB function utilizes an optimized local-minimum search algorithm known as the Nelder-Mead simplex direct search method. The algorithm is considered to have converged and the "pole" is found when the function value $\alpha(k_\parallel) < 10^{-4}$.

Figure B.2 illustrates the method used to determine all modes supported by a planar structure at a fixed wavelength. Depending on the location of the initial guess in the complex wavevector plane that is fed to the algorithm, the algorithm will converge on different poles. We then interatively sweep through the initial guesses to ensure convergence of all poles (modes) at a given wavelength. Physically reasonable "leaky modes" correspond to a complex transverse wavevectors $k_\parallel = k'_\parallel + ik''_\parallel$ such that the complex propagation constant $k_\perp = \sqrt{k_o^2 - k_\parallel^2}$ in the vacuum superstrate has $\mathrm{Re}[k_\perp] > 0$ and $\mathrm{Re}[k_\perp] + \mathrm{Im}[k_\perp] > 0$.

B.3 Ferrell-Berreman modes in thin- vs. thick-films

Figure B.3 shows the dispersion of the Ferrell-Berreman mode along with the dispersion of the long- and short-range surface plasmon polaritons that are supported by various thickness silver films. When the silver foil thickness is greater than a few skin depths of silver ($d_m \geq 100$ nm), the film supports two independent surface plasmons on either side of the foil which weakly interact with each other (see "100 nm"). As the film thickness decreases these modes interact and split into two distinct surface plasmons: the long- and short-range surface plasmons (see "10 nm"). For thick-films the Ferrell-Berreman mode (see inset) has a large negative group velocity, large imaginary part of its transverse wavevector $\mathrm{Im}[k_\parallel]$ and this mode couples poorly with free-space light. As the film thickness decrease, the Ferrell-Berreman modes becomes a slow-light mode and the imaginary part of its transverse wavevector $\mathrm{Im}[k_\parallel]$ is

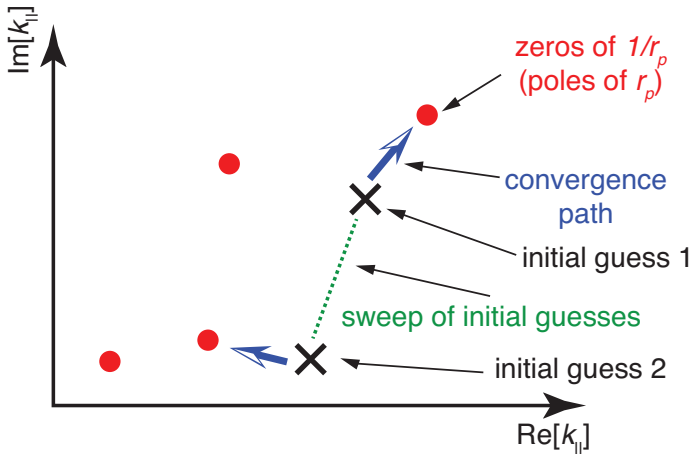

Fig. B.2. At a fixed wavelength, a structure can support many different modes characterized by a set of poles of the reflection coefficient r_p. These poles lie in the complex wavevector plane $k_{\|}$. We search for the zeros of the function $\alpha = 1/r_p(k_{\|})$ by systematically sweeping the initial guesses which are fed to the minimization algorithm `fminsearch` in MATLAB. The algorithm can converge on a different zero of $\alpha = 1/r_p(k_{\|})$, depending on the initial guess. The black points are the location of the poles in the complex $k_{\|}$-plane. The crosses are the initial guesses fed to the algorithm. The grey paths illustrate the pole to which the algorithm converges for a given initial guess.

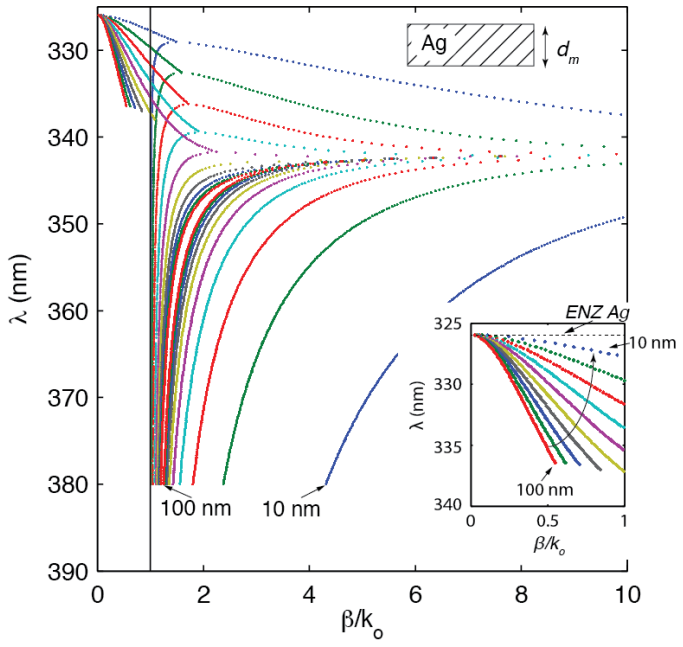

Fig. B.3. The evolution of the Ferrell-Berreman mode, the long-range SPP, and the short-range SPP for a thick silver foil to a thin silver foil. For thick films ($d_m \geq 100$ nm) the long-range SPP and short-range SPP are degenerate and as the foil thickness decreases the dispersion of these two modes "split" into disctintly different modes. For very thin films of silver, the Ferrell-Berreman mode has a very slow, negative group velocity that couples with free-space. For thicker films, the Ferrell-Berreman mode has a much larger negative group velocity and couples poorly with free-space light.

significantly reduced, thus leading to the Ferrell-Berreman mode interacting strongly with free-space light in the case of a very thin silver foil. In the effective medium, metamaterial limit the silver foils making up the metamaterial are considered to have vanishingly thin thicknesses.

C. EXPERIMENTAL VERIFICATION OF SUPER-COULOMBIC DIPOLE-DIPOLE INTERACTIONS

C.1 Experimental Determination of Average Decay Rates of Donors

In this section, we describe how we extract the effective FRET rate across metamaterials.

We utlize time-correlated single photon counting (TCSPC) to measure our fluorescence decay traces (see figure C.3) Microscopically, the fluorescence decay $I(t)$ that we detect with TCSPC originates from a discrete number of emitters. Each emitter can emit at most one photon per laser pump pulse. This is a good assumption since the excited state lifetimes of the emitters (100 ps - 200 ns) is much longer than the duration of the laser pump pulse in our experiments (25-40 fs). Therefore, if the laser pump pulse has triggered an emitter to make a transition to its excited state, there is a $> 99.98\%$ probability the emitter is still in the excited state by the time the laser pump pulse has propagated away.

In the continuum limit of arbitrarily long acquisition times (many many observed detector clicks), the i^{th} emitter, will emit a decaying single exponential after the pump laser has arrived (and gone) so that our detected signal from this i^{th} single emitter takes the form

$$I_i(t) = u(t - t_o)\mathrm{e}^{-\gamma_i(t-to)}, \tag{C.1}$$

where $u(t)$ is the unit step heaviside function, γ_i is the fluorescence decay rate of the i^{th} emitter, and t_o is the arrival time of the laser pump pulse at the emitter [130]. In these nanoscale geometries t_o can be taken as the same constant for all emitters since the transit time of the pulse through the sample ($\approx$ 1 fs) is much shorter than our instrument response time of the TCSPC apparatus ($\approx$35 ps).

In experiment, we simultaneously measure the fluorescence decay trace of many donors ($> 10,000$) at once, each of which will emit a unique decaying single exponential with decay rate γ_i. In this limit of many emitters, the fluorescence decay trace $I(t)$ in general will be multi-exponential and can be approximated as a Laplace Transform of a continuous distribution of decay rates, that is an integral of a distribution of decaying exponentials

$$I(t) = \int_0^\infty \mathrm{d}\gamma \; A(\gamma) u(t) \mathrm{e}^{-\gamma t} \tag{C.2}$$

where $A(\gamma)$ is the distribution of *decay rates* present in the signal $I(t)$ for $t > 0$. We have now set $t_o = 0$ for simplicity and without a loss of generality.

If the fluorescence decay trace $I(t)$ is normalized such that $I(t = 0^+) \equiv 1$, we necessarily apply the normalization condition

$$1 \equiv \int_0^\infty \mathrm{d}\gamma \; A(\gamma) \tag{C.3}$$

on the distribution of decay rates. With this normalization, the integral over all times of the decay trace yields

$$\int_{-\infty}^{\infty} \mathrm{d}t \; I(t) = \int_{-\infty}^{\infty} \mathrm{d}t \int_0^\infty \mathrm{d}\gamma \; A(\gamma) u(t) \mathrm{e}^{-\gamma t} \tag{C.4}$$

$$= \int_0^\infty \mathrm{d}\gamma \; \frac{1}{\gamma} A(\gamma). \tag{C.5}$$

We now note that the Harmonic mean of a decay rate distribution is rigorously defined as

$$\bar{\gamma} = \left(\frac{\int_0^\infty \mathrm{d}\gamma \; \frac{1}{\gamma} A(\gamma)}{\int_0^\infty \mathrm{d}\gamma \; A(\gamma)} \right) \left(\right. \tag{C.6}$$

Since we have $1 \equiv \int_0^\infty \mathrm{d}\gamma \; A(\gamma)$, then the integral

$$\int_0^\infty \mathrm{d}t \; I(t) = \bar{\gamma}^{-1}. \tag{C.7}$$

That is, by normalizing our measured decay traces I(t=0) = 1, we can estimate our average donor decay rates by integrating the observed decay trace and performing a single division.

To quantify the additional decay pathway of the donor molecules with the acceptor molecules present on the opposite of the metamaterial, we subtract the effective decay rate of the donor alone measurements with that of the donor with acceptors:

$$\Gamma_{\mathrm{FRET}} = \Gamma_{\mathrm{eff}}^{\mathrm{DA}} - \Gamma_{\mathrm{eff}}^{\mathrm{D}}. \tag{C.8}$$

Figure C.1 shows a set of measurements for the 100 nm multilayer metamaterial sample, from which we build up statistics of the average decay rate for the donor alone and donor with acceptor hybrid samples as shown in figure C.2.

In the Ag and metamaterial samples, a 3.5 nm SiO2 cap layer is used to prevent complete fluorescence quenching at the metal surface (see figure C.9). Due to slight instabilities in the ultrathin deposition of this SiO2, the exact thickness of the cap layer varies from deposition to deposition (3.3-4 nm). From the quartz crystal monitor, this variation is known for each run and this accounts for the variation in the exact magnitude of the effective decay rate for the donor and donor with acceptor samples. It is *important* to note that for a particular set of samples (e.g. donor alone and donor with acceptor for the "trilayer" metamaterial) the thickness of the capper layer is fixed and the computation of th

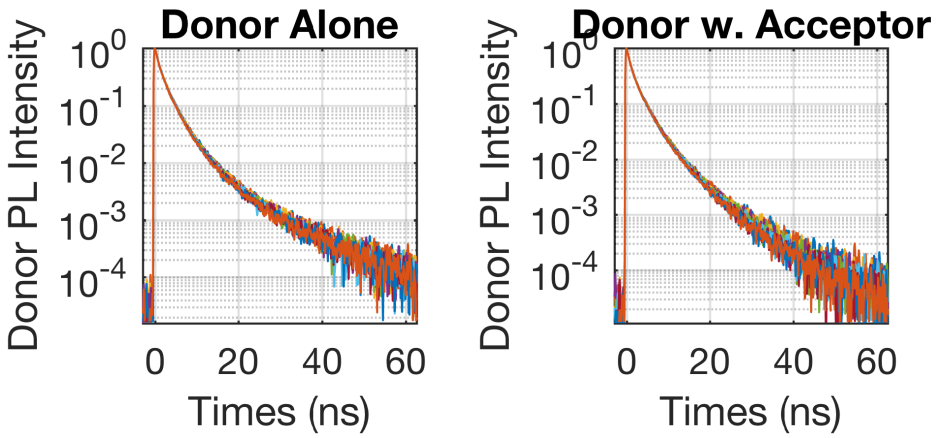

Fig. C.1. Nine normalized decay trace measurements at far separated locations on the metamaterial ($\Delta x \approx 10\mu$m) are shown for the donor alone sample (left) and the donor with acceptor, hybrid sample (right). Different colors present indicate the measurements at different locations.

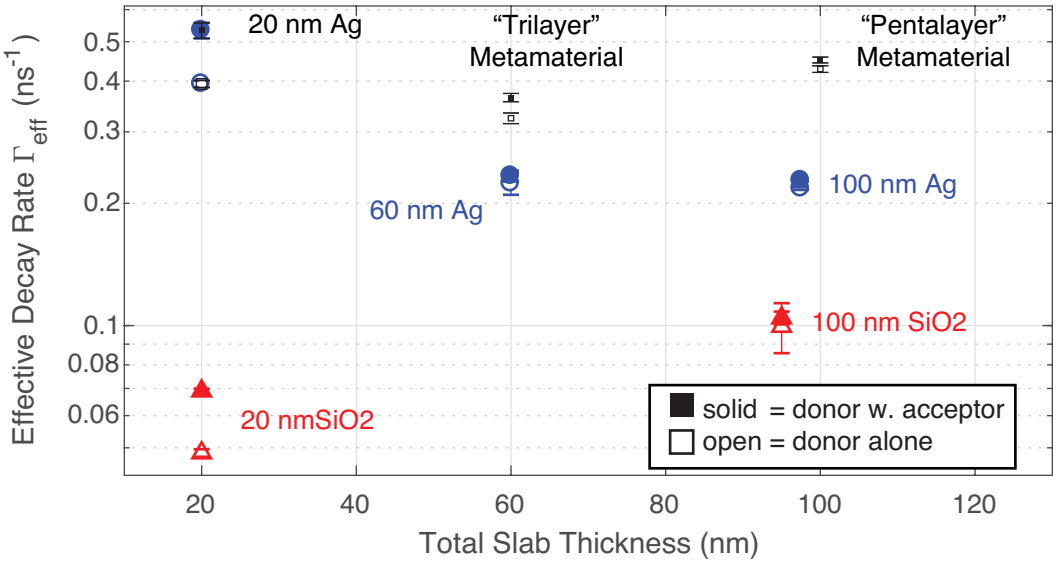

Fig. C.2. The effective decay rates of the donor alone and donor with acceptor samples observed in experiment are shown. The donor alone data are shown with hollow, open data markers while donor with acceptor data are shown with solid data markers.

C.1.1 Experimental Apparatus for acquiring Fluorescence Lifetimes

Figures C.3 and C.4 shows the schematic layout of the experiment to determine the fluorescent lifetime of the molecules in the experiment. We pump the samples from the *donor side* (reflection mode, figure C.4) with $\approx$ 40 fs, 400 nm laser pulses from an optical parametric amplifier (Spectra Physics NOPA 2H, 2016) which is in turn pumped by 1040 nm, 400 fs, 20 J laser pulses (Spectra Physics Spirit, 2016). The resulting fluorescence is collected by the same objective and sent through a variable filter wheel that can be used select different bands of emitted colors.

A flip mirror allows us to divert the fluorescent emission to an imaging spectrometer to monitor the total spectrum of emission and the uniformity of the emission intensity. To monitor the emission spectra, we utilize a 450 nm long pass filter in the filter wheel and tune the spectrometer spectral dispersion window to $\lambda = 550$ nm. To directly image and ensure the uniformity of the emission intensity, we turn off the spectral dispersion of the spectrometer (tune the spectrometer grating so that the zeroth order, specular reflection is incident on the CCD) and open the entrance slit to the spectrometer. Different bands of colors can then be imaged by selecting different narrow-band pass filters in the variable filter wheel.

When the flip mirror is removed, the emission passes through a spatial filter and is then focused onto a single photon avalanche diode (SPAD) whose "clicks" are referenced with the synchronized clock pulse of the pump laser. Statistics are then built up of the relative arrival times of the SPAD clicks (time correlated single photon counting, TCSPC). The approximate resolution (instrument response function) of our SPAD/TCSPC system is $\approx$ 35 ps, measured with an extremely attenuated 500 nm, 100 fs pulse output from the OPA (see Figure C.3). Donor fluorescence emission is isolated from that of acceptor fluorescence and any background with a narrow band-pass filter centered on the blue edge of the donor PL spectrum.

We use a three axis piezo electric translation stage, along with the imaging spectrograph to ensure we are acquiring lifetime data at a portion of the sample which

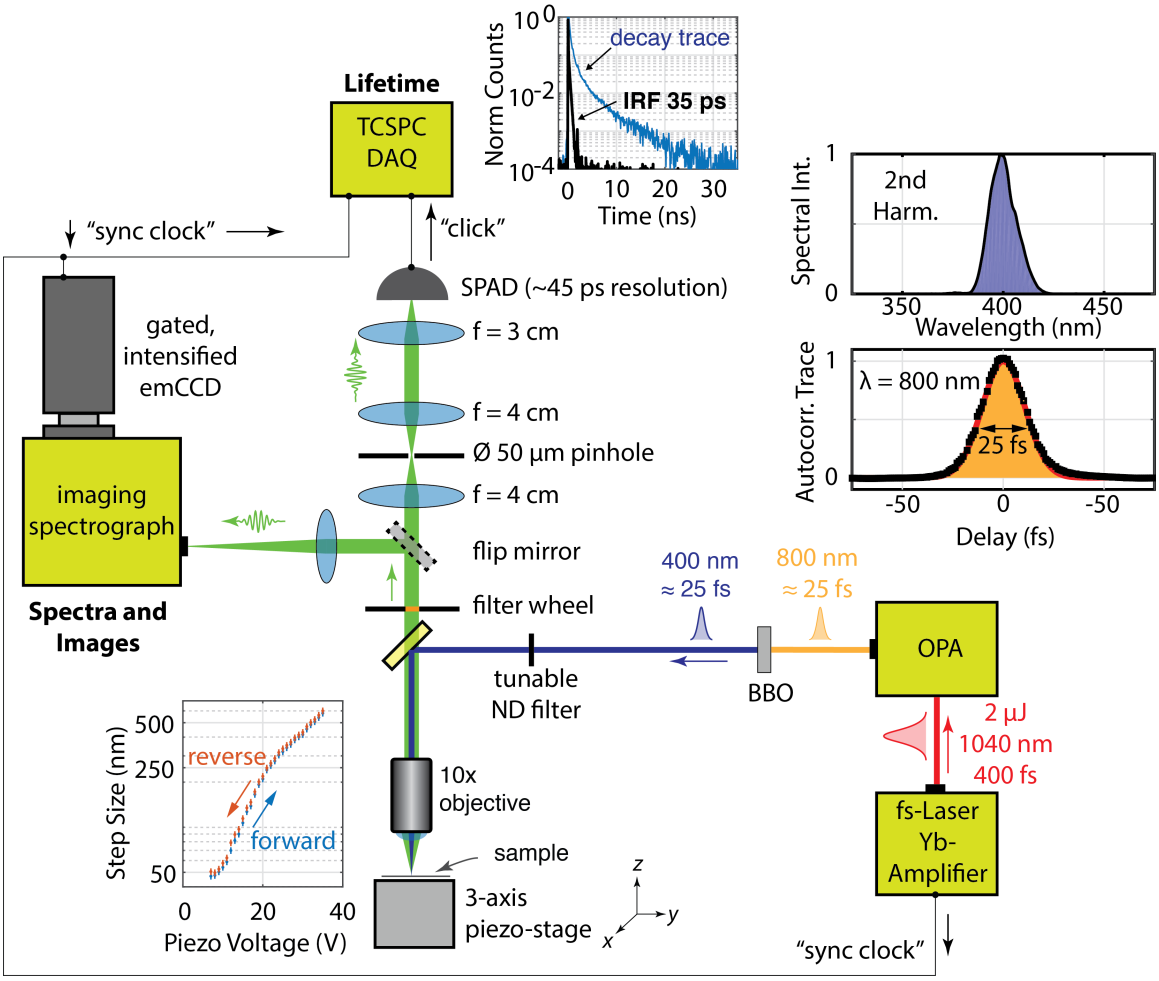

Fig. C.3. Experimental apparatus for obtaining time resolved fluorescence. The repetition rate of the pump laser is 100 KHz. The $\lambda = 400$ nm, 25 fs pulses arriving at the sample have pulse energies ranging from 0.01-100 nJ. Typical lifetime traces are acquired with pulse energies around 0.1 nJ.

has uniform fluorescent emission (no hot spots, scattering centers, nor areas of unusually bright emission). The calibration curve for the piezo electric translation stage is shown in Figure C.3.

The cross sectional area of the $\lambda = 400$ nm ultrafast optical excitation beam is $\approx 2\mu m^2$. For the same sample ($\approx$ 1"$\times$1" macroscopic size), individual data sets (20

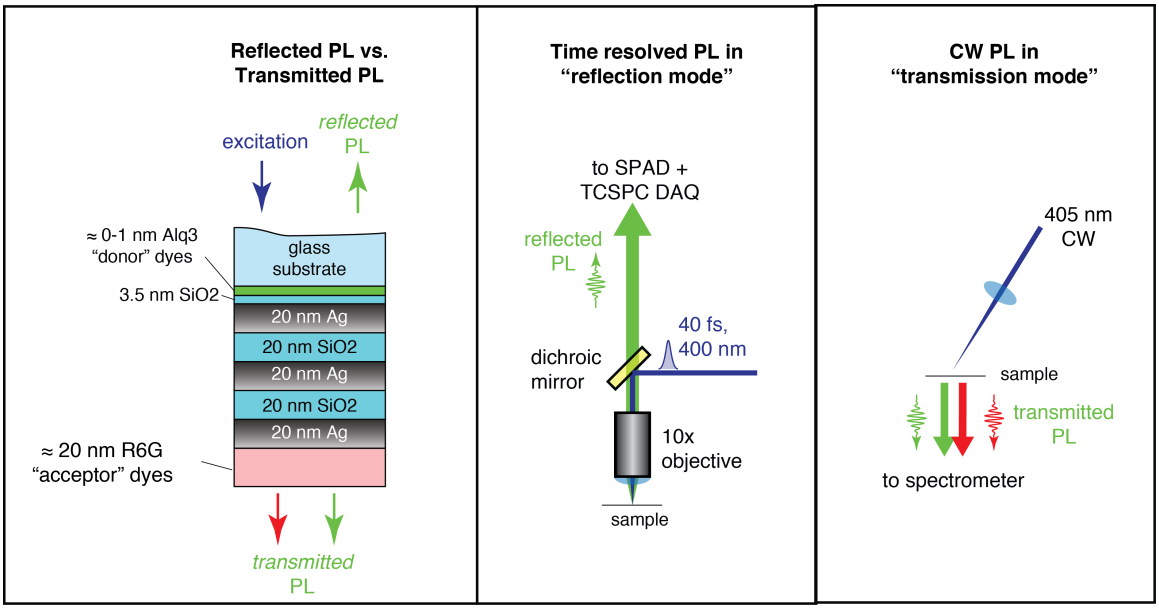

Fig. C.4. Reflected PL is used to monitor the donor fluorescence lifetime while the transmitted PL is used to monitor the acceptor fluorescent emission intensity.

or more points on a $\approx 10\mu m^2$ pitch square grid) are recorded at far separated areas of the sample ($\approx$ 4 mm). These individual data sets are then averaged as shown in the fluorescence decay traces shown in chapter 4, figure 4.3. The errors bars shown therein represent the uncertainty due to the spread in the measured individual decay traces. Note that the error bars contain (1) the shot noise of detection and, (2) the spread in measured data (standard deviation) due to long- (4 mm) and short-range (10 m) non-ideal uniformities of sample geometry and dye concentration.

Measurement uncertainty and the propagation of this uncertainty is carefully considered based on techniques and theory from An Introduction to Error Analysis, John Taylor, University Science Books (1997).

C.2 Isolation of Donor Emission from background fluorescence emission

Thin films of SiO_2 fluoresce in the green part of the visible at ns-time scales under UV light excitation. Since our pump is an ultrashort pulse centered around 400 nm (see figure C.3), we must ensure that any emission from the Ag/SiO_2 metamaterial structure itself, as well as any emission from undoped PMMA film, do not cloud our measurements on the donor emission kinetics. Figure C.5 shows (1) the background fluorescence emission that is present in our donor measurements of the metamaterial sample and, (2) the signal intensity for the donor only sample. We find that at the fluorescence peak of Alq3 ($\lambda \approx 520$ nm), the background flourescence is approximately 250x weaker than the Alq3 emission.

Figure C.6 shows the time dynamics of background emission from the metamaterial structure at a wavelength of $\lambda = 500$ nm. This background emission displays two distinct time scales. Over 75% of the emission decays in the first 500 ps after the ultrafast laser excitation, while the remaining fluorescence slowly decays at a time scale of ≈ 200 ns.

From this data, we definitively conclude that the nanofabricated metamaterial structure itself does not contribute to the observed donor emission kinetics of Figure 3 in the main manuscript greater than one part in two hundred fifty.

C.3 Steady State Energy Transfer Measurements

Steady state fluorescence measurements are taken in Transmittance mode (see figure C.4. This allows us to determine whether or not energy transfer (of any kind) is taking place across the samples. The experimental schematic is shown in C.7. The samples are pumped from the donor side by a 405 nm CW laser (Spectra Physics Excelsior). The fluorescent emission (both donor and acceptor emission) is collected from the acceptor side (the opposite side of the thin films). The steady state spectra of the fluorescence is then measured with a fiber coupled high sensitivity CCD miniature spectrometer (made by Ocean Optics).

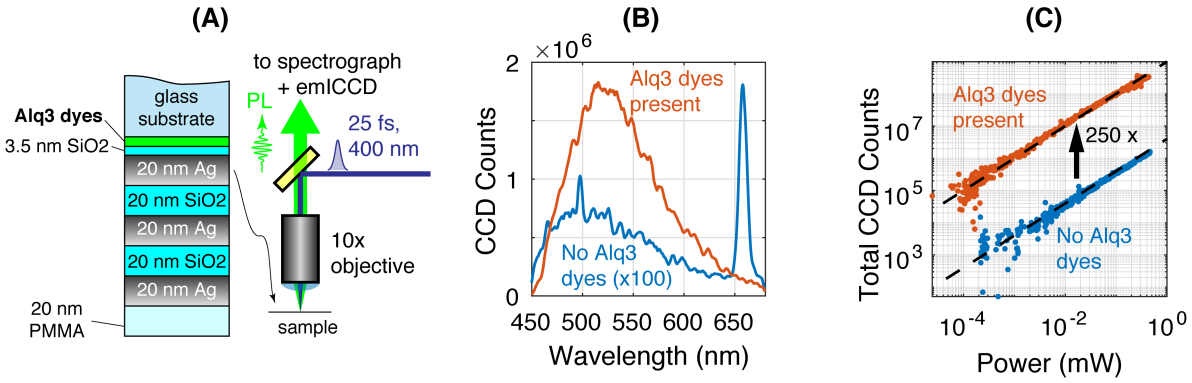

Fig. C.5. Background Fluorescence: (A) We pump the metamaterial structure with ultrashort 25 fs laser pulses centered at $\lambda = 400$ nm from the substrate side of the sample. The resulting fluorescence is collected in a confocal geometry with a 10x objective and sent to a spectrograph coupled with a high sensitivity gated CCD. (B) The metamaterial control sample with no Alq3 donor dyes present (the undoped PMMA film is still present) shows a broad fluorescence in the green and a sharp fluorescent peak around $\lambda = 660$ nm. This sharp fluorescence peak in the background signal is well out of the range of detection of our emission time dynamics measurements which are centered at $\lambda = 500$ nm. (C) Fluorescence intensity versus incident laser pump power is shown for the control sample (no dyes present) and the Alq3-doped (donor alone) metamaterial sample. We find that both fluorescence signals are in the linear regime (dashed lines) at our experimental bandwidth of $\lambda_{\text{center}} = 500$ nm $\Delta\lambda = 20$ nm. Furthermore, at all pump powers the background fluorescence (blue) is about 1/250x the intensity of the Alq3-doped metamaterial (red).

Control experiments were undertaken to test whether the background fluorescence emission of the undoped PMMA films and the nanofabricated Ag/SiO2 multilayer metamaterial structure itself were present in the observed donor or acceptor spectra (Figure 3 in main manuscript). We find that the background spectra are at least one order of magnitude weaker than the transmitted Alq3 donor emission, and the R6G acceptor emission. The spectra shown in Figure 3 of the main manuscript are then reliable measurements of the Alq3 donor and R6G acceptor spectra.

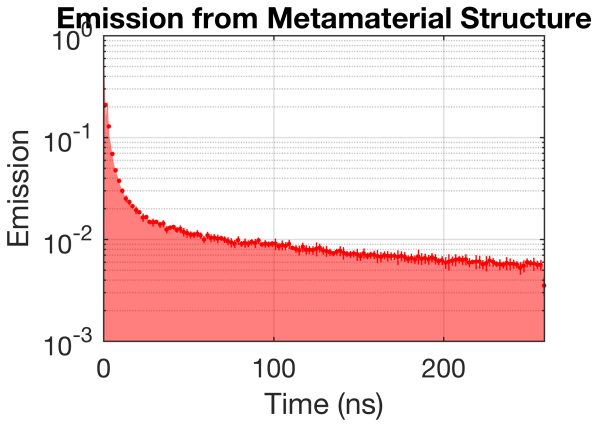

Fig. C.6. The time resolved background fluorescence emission of the multilayer metamaterial structure whose spectrum is shown in figure C.5. The metamaterial background emission at a wavelength of 500 nm (the wavelength of the decay traces shown in the figure 4.3 of chapter 4) is very rapid, with over 75% the emission coming in the first 500 ps after the laser pulse. There is also a slow component to the background fluorescence, decaying at a time scale of $\approx$ 200 ns.

C.4 Metamaterial Design and Forster Resonance Energy Transfer Pair Selection

Multilayer Metamaterial Design The hyperbolic medium is designed using a metal(Ag)-dielectric(SiO2) plasmonic super-lattice with layer thicknesses (20$\pm$2 nm), making the unit cell of the metamaterial much smaller than the central wavelength of donor emission at $\lambda = 525$ nm. This ensures condition ensures multilayer behaves like an effective medium. Using these equal SiO2/Ag layers thicknesses of 20 nm allows a hyperbolic dispersion across the entire spectral overlap region between Alq3 donors and R6G acceptors. Deviations from effective medium theory are expected for high spatial frequency light, however, spectroscopic ellipsometry measurements confirm that the effective dielectric permittivity tensor of the multilayer can be approximated by $\epsilon_x \approx -4.2 + 0.2i$, $\epsilon_z \approx 5.4 + 0.01i$ at $\lambda = 525$ nm [66]. This confirms the type II hyperbolic metamaterial behavior essential to create Super-coulombic interaction pathways between donor and acceptor molecules, while simultaneously suppressing

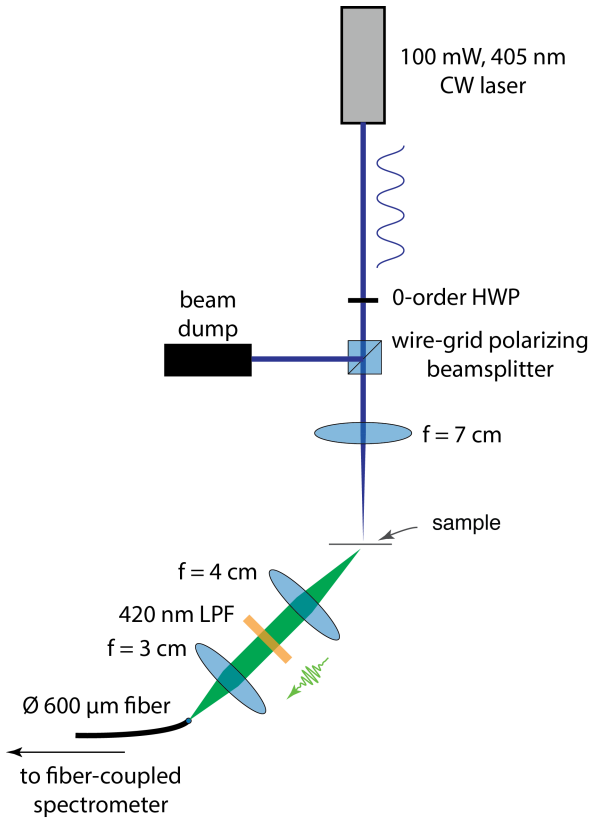

Fig. C.7. Experimental apparatus for measuring the steady state energy transfer *through* the dielectric, metal and metamaterial films is shown.

conventional radiative interactions as the propagating spatial modes in vacuum decay within the metamaterial (transmission $< 1\%$ at $\lambda = 525$ nm). In this multilayer metamaterial, the microscopic origin of super-Coulombic RDDI is the coupled charge oscillations of Bloch surface plasmon-polaritons supported by the thin silver films.

Donor and Acceptor For our acceptors we choose the organic laser dye R6G (purchased from Sigma-Aldrich Corp.). The fluorescence emission and absorption cross section of R6G are shown in figure C.8. For our donors we choose the organic fluorophore Alq3 (purchased from Sigma-Aldrich Corp.), whose fluorescence emission spectrum, peaking at $\lambda \approx 525$ nm is shown in figure C.8. Alq3 has a strong absorption at $\lambda = 400nm$, far removed from the absorption band of R6G, making it an ideal

FRET pair for R6G: the laser pump exciting the donors has a low probability of exciting R6G into its excited state.

FRET Radius Estimation The FRET radius is the donor-acceptor distance at which the FRET rate will be equal to the spontaneous emission rate of the donor. It can be calculated from the following equation, derived from first principles [4]:

$$R_o = \left[\frac{3c}{32\pi^4 n^4} \int_0^\infty f_D(\lambda)\sigma_A(\lambda)\lambda^2 \mathrm{d}\lambda \right]^{1/6}. \tag{C.9}$$

Here c is the speed of light, n is the refractive medium of the donor-acceptor host medium, $f_D(\lambda)$ is the donor emission spectrum and $\sigma_A(\lambda)$ is the acceptor absorption cross section. The normalization imposed on $f_D(\lambda)$ is

$$\mathrm{QE} = 2\pi c \int_0^\infty f_D(\lambda)/\lambda^2 \mathrm{d}\lambda \tag{C.10}$$

where QE is the internal quantum efficiency of the Alq3, taken from literature to be around 0.35 [165].

Using the quantitative emission and absorption properties present in figure C.8, along with the quantum yield of Alq3 of ≈ 0.35, we find the FRET radius to be $R_o \approx 5.1 \pm 0.1$ nm.

C.5 Metamaterial Fabrication and Material Characterization

C.5.1 Fabrication

Silver and silica multilayer films were deposited on BK7 glass microscope slides using a multi-source electron beam evaporation vacuum chamber. Film thicknesses and deposition rates were calibrated through `JEOL 6301F` scanning electron microscope micrographs and through ellipsometry. In situ measurements of deposition rates and hence thicknesses were monitored during deposition with a quartz crystal oscillator. Electron beam evaporation was performed at a vacuum pressure of $P \approx 9 \times 10^{-7}$

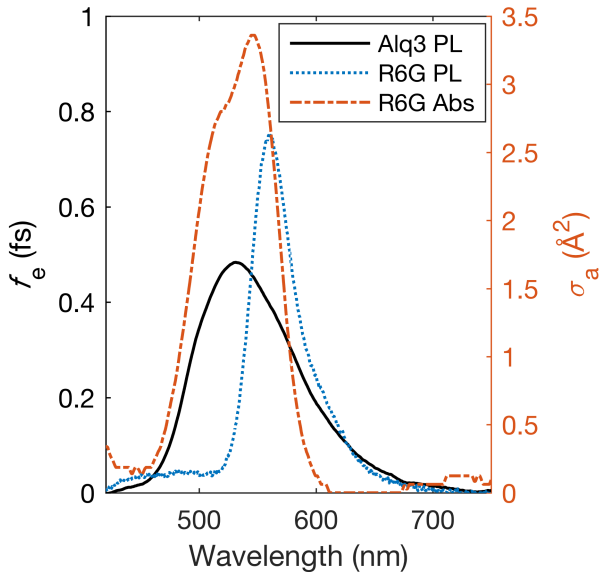

Fig. C.8. Photoluminescence emission and absorption cross section spectra of Alq3 and R6G dyes. Alq3 having a PL quantum efficiency of $\approx$ 35% is spin-casted as a monolayer while R6G is spin-casted as 20 nm films in PMMA 495.

Torr. The substrates were ≈ 50 cm from the evaporation sources. Prior to any thin-film deposition, BK7 glass Substrates were cleaned via a triple ultrasonic cleaning in solvents in the following order: toluene, acetone, isopropyl alcohol, methanol. Silicon substrates (for ellipsometry and SEM measurements) were cleaned in a piranha etch (three parts sulphuric acid to one part H_2O_2) prior to deposition.

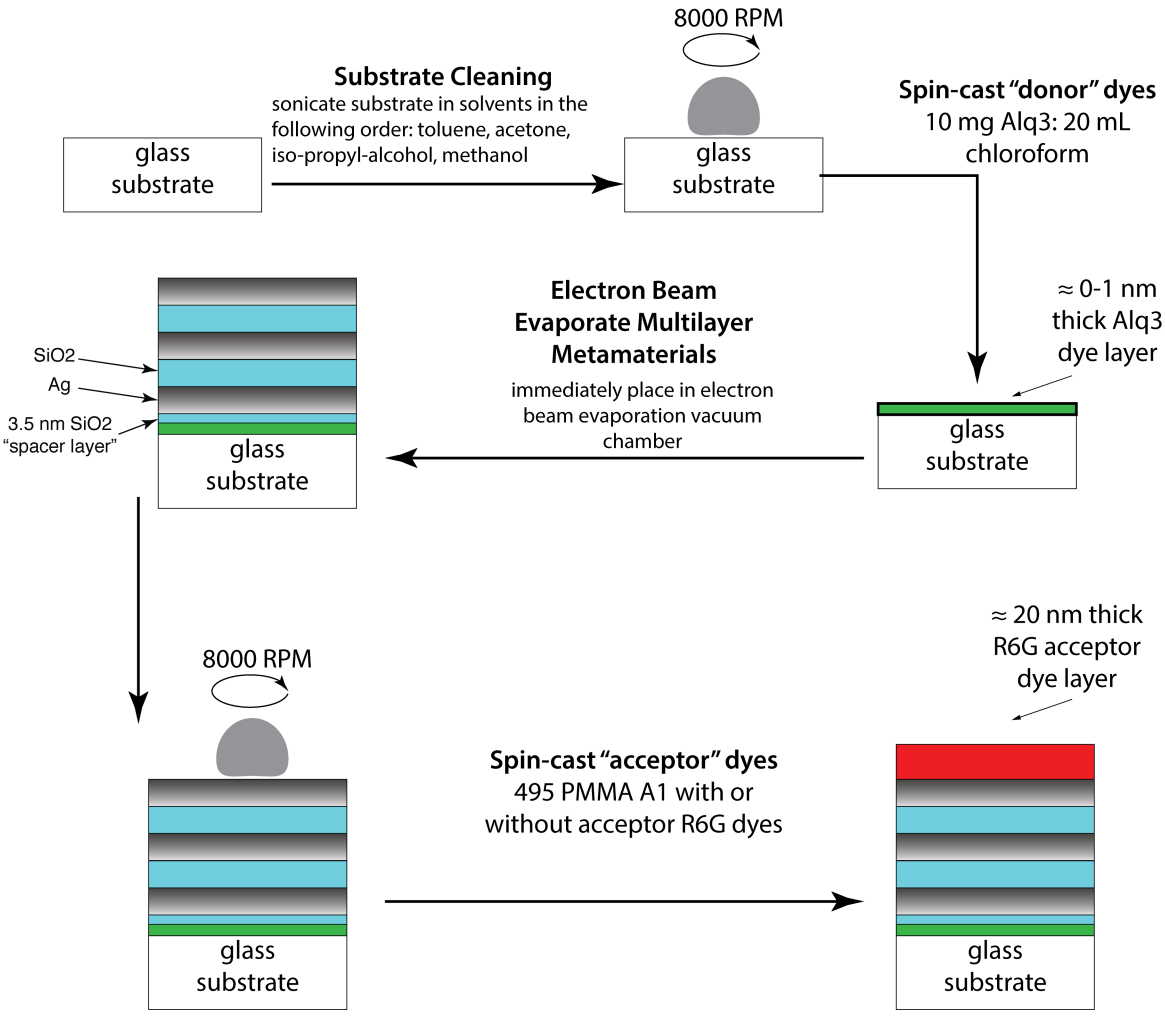

Fig. C.9. Fabrication process flow for multilayer metamaterials displaying super-Coulombic interactions.

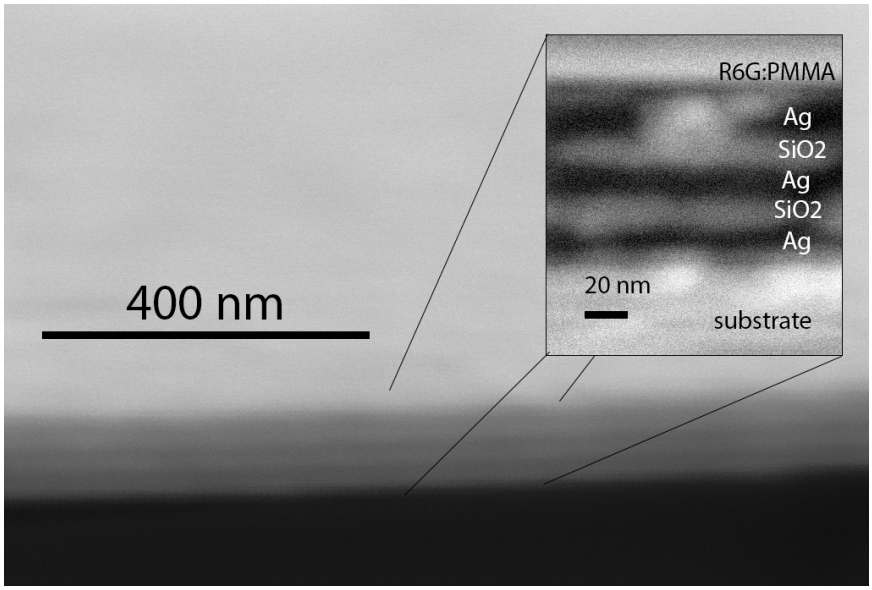

Fig. C.10. A SEM micrograph of the nanofabricated HMM structure is shown. It is difficult to obtain high contrast in the samples with R6G:PMMA present, as low electron fluxes are required to prevent the organic PMMA film from disintegrating and taking over the image.

C.5.2 Determining Optical Constants

Optical constants of the constituents making up our multilayers exhibiting super-Coulombic dipole-dipole interactions, namely Ag and SiO_2 were extracted as described in the Appendix A.2.

C.5.3 Fluorescent Dye Film Fabrication

Donor, Alq3 films Very thin, 0-1 nm thick films of Alq3 molecules (donor in experiment) are fabricated by spin-casting a solution composed of 5 mg Alq3 in 15 mL of chloroform. A few drops of this solution are placed in the center of the substrate. The substrate is then spun at 8000 RPM. The centrifugal force causes the solution to rapidly accelerate towards the edge of the substrate and the solution is transformed from a droplet to a flattened shape. Most of the original solution is lost as it flung from the substrate, while the remaining solution has a large surface

area to volume ratio and the volatile chloroform solvent begins to rapidly evaporate. The rapidity of this evaporation is further increased by an exhaust fan removing the gaseous chloroform in the vicinity of the substrate, and thus reducing the chloroform partial pressure. At the end of the 60 s spin cycle, only the Alq3 dyes remain, spread out stochastically with a surface concentration depending on the original dye solution concentration, the spin speed and the volatility of the chloroform solvent.

Acceptor, R6G films PMMA is a polymer based glass (i.e. plastic) that acts as a very good dielectric host matrix for fluorescent particles (e.g. dyes and quantum dots). The procedure to make nanoscale films of R6G-doped PMMA films is as follows. R6G and PMMA are dissolved in a solution anisole and methanol. A few drops of the R6G:PMMA solutions placed roughly in the center of a substrate and the substrate is spun at high angular velocity ($\approx 8000 RPM$). Due to the centrifugal force felt by the liquid, the drops tend to *thin out*. At a certain thickness, the surface tension forces of the thin pancake of solution balance (or close to) the centrifugal force. If the solution is held at this condition for some time, the solvents dissolving the PMMA (and dyes) begin to evaporate and the former solution transforms into, more or less, a solid, rigid film or PMMA:R6G. After the spinning procedure is finished, the substrate and the PMMA film are baked (annealed) at 180 ^{o}C, a temperature higher than the boiling temperature of the solvents. This serves two purposes: (1) boil off any remaining solvents and (2) *reflow* the PMMA film. (1), above, is critical to achieve repeatable results for any remaining high vacuum thin-film deposition, while (2) is useful to increase the flatness and uniformity of the PMMA film. Pre-anneal and post-anneal measurements of the R6G:PMMA fluorescence emission intensity (the R6G:PMMA is pumped by a CW $\lambda = 532$ nm laser) confirm that the annealing process does not degrade or significantly alter the R6G dyes.

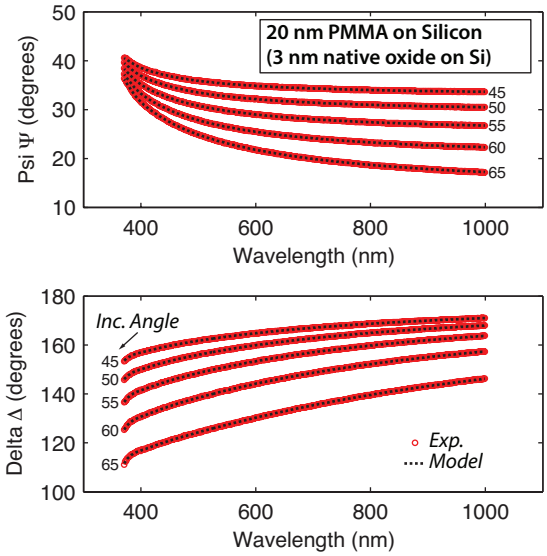

Fig. C.11. Spectroscopic ellipsometry measurements and modeling for the PMMA film results in a highly reliable estimate of the dielectric permittivity and film thickness ($t_{\mathrm{PMMA}} \approx 20 \pm 1.5$ nm).

C.5.4 Determination of dye film thicknesses and the dye concentrations

Acceptor, PMMA:R6G films We determine the thickness and optical wavelength scale uniformity of the R6G:PMMA films using ellipsometry of films deposited on a silicon wafer. First, we refine the dielectric permittivity function for undoped PMMA films as shown in figure C.11. A Cauchy model with a UV absorption band edge is utilized for PMMA, where local thickness measurements yield a ± 0.5 nm uncertainty. The variation of PMMA thickness across the entire sample leads to a thickness uncertainty of ± 1.5 nm.

Second, we then spin-cast R6G doped PMMA films, as described above. Using ellipsometry, we determine the thickness of this film utilizing the undoped PMMA model, fitting the spectroscopic ellipsometry data for wavelengths longer than the absorption band of the R6G ($\lambda > 600$ nm). For our R6G:PMMA solutions, we estimate our final acceptor R6G:PMMA films to have a thickness of 20 ± 1.5 nm.

To determine the R6G dye concentration in the vicinity of the metamaterial, we ulilize thin-films of R6G:PMMA spin-casted on glass substrates where we model the transmittance T through a film with the Beer-Lambert law

$$-\log_{10} T = \sigma \iint\!\!\!\!\!\!\int \mathrm{d}z \; c(z), \tag{C.11}$$

where σ is the absorption cross section of the dye and $c(z)$ is the dye concentration profile of the film (remember the films are uniform in thickness to $\pm 7\%$, so there is a translation invariance in the xy-plane). In this case the transmittance is $T = P/P_o$, where P is the power transmitted through the glass substrate and the thin film of R6G:PMMA, while P_o is the power transmitted through an equal thickness film of undoped PMMA on glass. We assume that the concentration profile is uniform within the film so that the dye concentration is c within the film and zero elsewhere. It then follows that the dye concentration can be estimated from the relation

$$c = \frac{-\log T}{L\sigma}, \tag{C.12}$$

where L is the film thickness. The absorption cross section of R6G in PMMA is approximately 3.36 $\mathring{A}^2$, the film thickness is $L = 20 \pm 1.5$ nm, and the negative logarithm of the transmittance is measured to be as $\log T = 0.05 \pm 0.01$. We then estimate the acceptor R6G concentration in the vicinity of the metamaterial as

$$C = 0.074 \pm 0.012 \text{ particles } /\text{nm}^3 = 7.4 \times 10^{21} \pm 1.2 \times 10^{21} \text{ particles } /\text{cm}^3. \tag{C.13}$$

These calculations agree closely with the Stoichiometric calculation of $c = 0.070 \pm 0.05$ particles $/\text{nm}^3$, based on the initial molar concentrations of the R6G dye and PMMA in the initial spin-casting solution.

C.5.5 Roughness measurements via Atomic Force Microscopy

Atomic Force Microscopy (Bruker: Dimension Edge) was performed on the the fabricated Ag/SiO_2 metamaterials, and the individual constituent materials respectively. Figure C.12 shows AFM measurements and the inferred surface roughness for

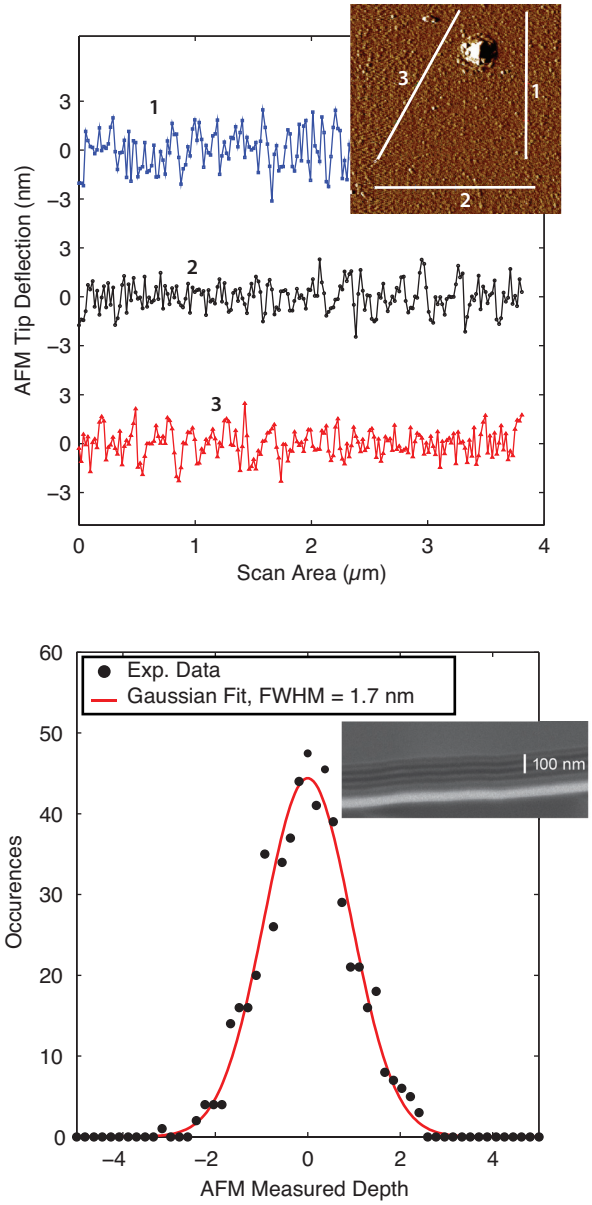

Fig. C.12. (a) AFM line scans of Ag/SiO2 multilayer deposited on a glass microscope slide (top and bottom layer silver). The inset shows an overview of the surface topography measured via the AFM scan. (b) The AFM depth histogram of all the line scans from panel (a) reveals an RMS surface roughness of $\approx$ 1.7 nm. The inset shows a SEM micrograph of a five period Ag/SiO2 multilayer on a glass substrate.

the top layer of a five-period Ag/SiO_2 metamaterial deposited on a glass substrate. From these measurements we estimate the RMS surface roughness of our multilayer metamaterial to be $R_{HMM} \approx 1.7$ nm. Similar measurements were performed are bare Ag and bare SiO_2 films. The RMS surface roughness of a bare (50 nm thick) Ag film on glass microscope slide was estimated to be $R_{Ag} \approx 2.5$ nm, slightly larger than that of the metamaterial. The RMS surface roughness of a bare (100 nm thick) SiO_2 film on a glass microscope slide was estimated to be $R_{SiO2} \approx 1.3$ nm.

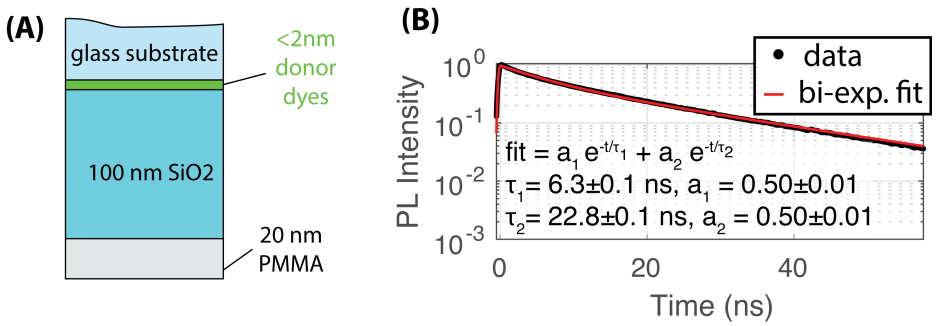

Fig. C.13. (A) Schematic of the fabricated sample used to extract the fluorescence lifetimes of ultrathin layers of Alq3 donor dyes used for theory simulations of more complex metamaterial nanostructures. (B) Ultrathin Alq3 donor dyes embedded within glass exhibit a dynamic fluorescence bi-exponential decay.

C.5.6 Spectrum of energy transfer and role of SPPs: Propagation Lengths of SPPs

In our experiment, we observe Alq3 donor emission from the opposite side of a 100 nm silver film (Figure C.17(A)). Interestingly, we observe that when acceptors are introduced on the opposite side of the 100 nm Ag film, the donor emission intensity previously observed is significantly quenched[1] (Figure C.17(B)). This is easily explained by noting that absorption of propagating donor emitted SPPs by R6G is

[1]see figure 4.3 in chapter 4.

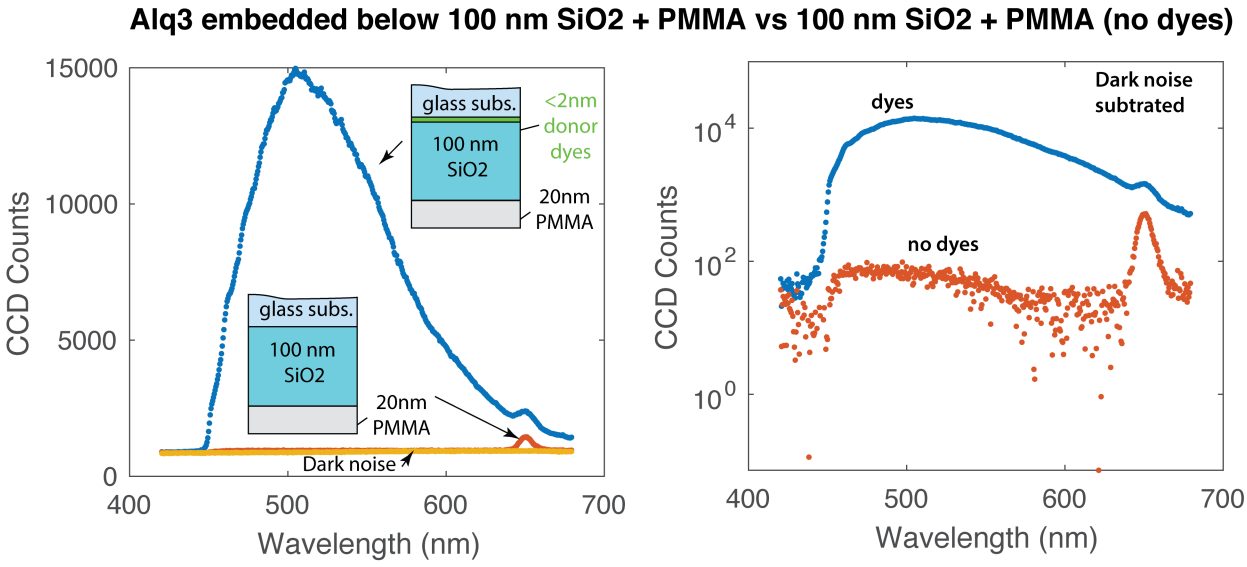

Fig. C.14. Alq3 Fluorescence Signal vs Background Fluorescence under pulsed illumination. Under the same pulsed laser pump conditions as the lifetime data of Alq3 embedded within 100 nm glass shown above, we find that the 100 nm SiO2 + 20 nm PMMA structure itself do not significantly contribute to our Alq3 dye signal better than one part in one hundred.

much more probable than scattering to free space. This section of the appendix explains this observation.

At the emission wavelengths of the donor (Alq3) the silver is optically thick (i.e. negligible transmittance of free-space propagating light). Thus we conclude that we observe scattered propagating surface plasmons. The Alq3 donor emitters relax, emitting energy into a SPPs which are weakly coupled to the opposite side of the 100 nm Ag film. These SPP propagates along the Ag/PMMA interface for some distance before it is (a) scattered to free space by surface roughness or (b) absorbed by Drude-type losses within the Ag (Figure C.17(A)).

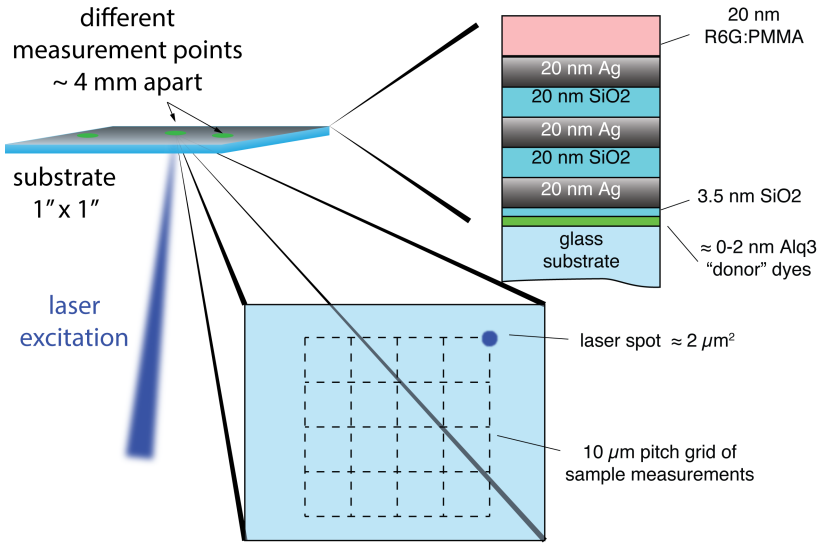

Fig. C.15. Size scales of nanofabrication and optical interrogation in relation to the physical size of the sample

The propagation length of the SPP along the interface is finite due to Ohmic, Drude-type losses within silver. It can be computed analytically by utlilizing the dispersion relation of the SPP at a metal/dielectric interface:

$$k_x = k_o \sqrt{\frac{\epsilon_m \epsilon_d}{\epsilon_m + \epsilon_d}}. \tag{C.14}$$

Here, k_x is the propagation wavevector along the metal/dielectric interface, ϵ_m is the permittivity of the metal (silver), ϵ_d is the permittivity of the dielectric (PMMA), and $k_o = \omega/c$ is the freespace wavevector. The propagation length is then computed as

$$L_{ohmic} = \frac{1}{2} \frac{1}{\mathrm{Im}[k_x]}. \tag{C.15}$$

The competing decay channel for the SPPs in this case is surface roughness scattering to free space (radiation of SPPs from surface roughness). The propagation

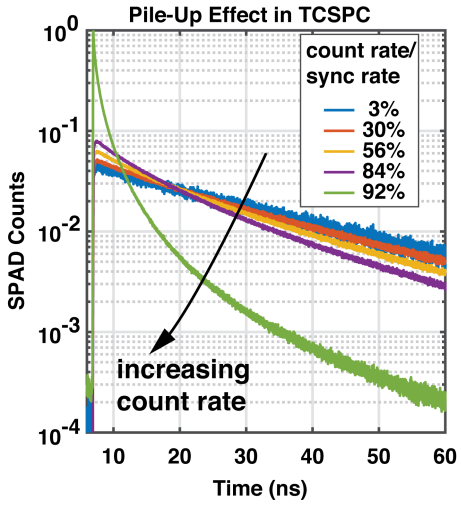

Fig. C.16. If the count rate of the SPAD detector exceeds 1% of the laser pump repetition rate, artifacts due to Poissonian emission from many fluorescence emitters causes significant artifacts in the decay trace. See ref [166] for further details of this unique experimental artifacts in TCSPC experiments.

length of SPPs on a rough surface can be estimated using the perturbative approach taken in Heinz Raether's book on surface plasmons (see equation 2.57 in [167]):

$$L_{rad} = \frac{3}{4}\frac{|\mathrm{Re}[\epsilon_m]|^{1/2}}{k_o^5}\frac{1}{\sigma^2\delta^2} \tag{C.16}$$

Here, δ is the RMS surface roughness of the silver while σ is the correlation of noise between seperate regions of the metal/dieletric interface. Using our AFM measurements, we estimate $\delta \approx 2.5$ nm and $\sigma \approx 30$ nm.

Figure C.18 shows the estimated propagation lengths of a surface plasmon propagating along a silver/PMMA interface. The black curve shows the propagation length for losses due to Drude damping (equation C.15) and the blue curve shows the propagation length for losses due scattering to freespace (radiation losses, equation C.16). The total propagation length is $1/L_{tot} = 1/L_{ohmic} + 1/L_{rad}$. It should be noted that $L_{ohmic} << L_{rad}$ so that internal, Ohmic damping is the dominant damping mechanism of surface plasmons. However, in experiment we do indeed detect the scattered plasmons in the form of visible PL.

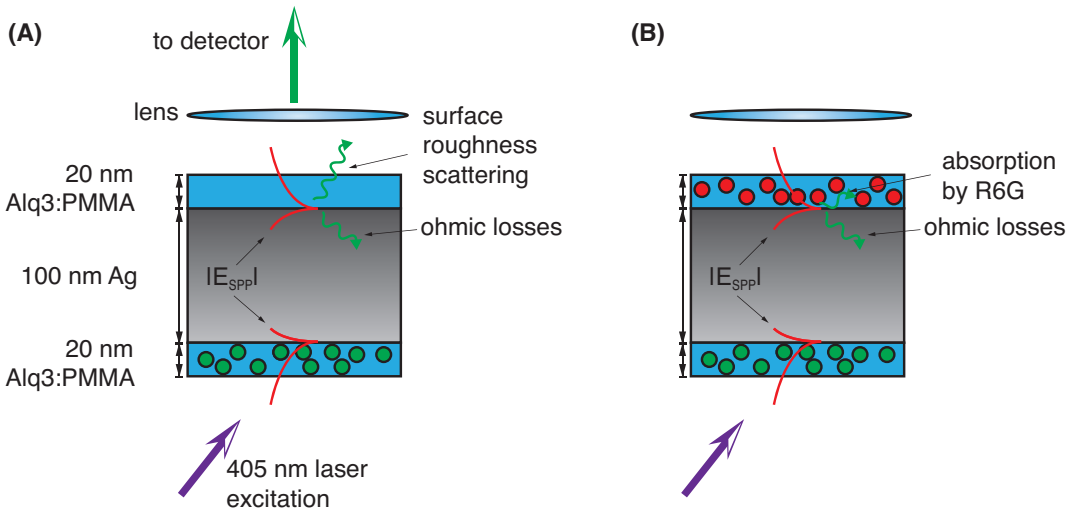

Fig. C.17. (A) The Alq3 donor emitters relax, emitting energy into a SPPs which are weakly coupled to the opposite side of the 100 nm Ag film.These SPP propagates along the Ag/PMMA interface for some distance before it is (1) scattered to free space by surface roughness or (2) absorbed by Drude-type losses within the Ag. (B) When the top PMMA layer is doped with acceptors (R6G), there is an additional decay channel for the propagating SPPs – namely, SPP absorption by acceptors. The damping of SPPs via R6G absorption is much more probable than scattering by surface roughness and we therefore observe a "quenched" intensity of Alq3 emission relative to (A).

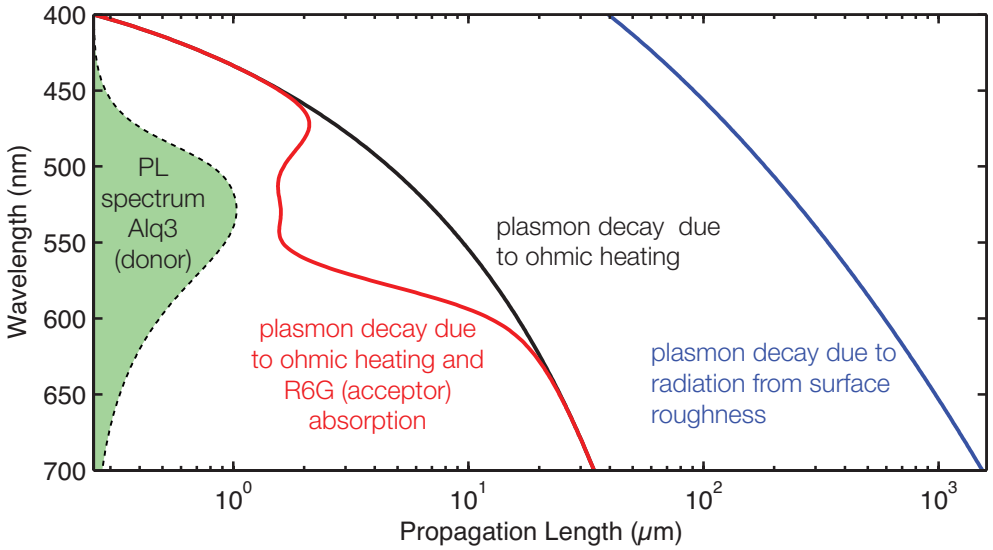

Fig. C.18. Propagation length of SPPs propagating along silver/PMMA interface. The blue curve shows the propagation length resulting from SPPs scattering to free-space via surface roughness of the silver. The black surve shows the propagation length resulting from damping due internal Ohmic losses of the silver. The dashed red curve shows the propagation length for SPPs propagating along a silver/PMMA with the PMMA doped with R6G. The presence of the R6G dopants significantly reduces the propagation length in the absorption band of the R6G.

However, when the top PMMA layer is doped with acceptors (R6G), there is an additional decay channel for the propagating SPPs – namely, SPP absorption by acceptors. The PMMA:R6G film has an absorption resonance at the transition frequency of the R6G molecule. That is, the dielectric permittivity of the PMMA layer now has an appreciable imaginary component at the transition frequency of the R6G molecules.

Utilizing ellipsometry, we can measure the complex dielectric permittivity of the PMMA:R6G film. We estimate $\epsilon_{R6G} \approx \epsilon_{PMMA} + i0.05$ within the absorption band of the R6G (in calcuations we use the exact shape of the absorption specta). When this, now complex, permittivity is substitued into equations C.14 and C.15, we can estimate the propagation length of SPPs along the silver/PMMA:R6G interface $L_{ohmic+R6G}$ (dashed red curve, Figure C.18). Relative to SPPs propagating along a silver/undoped PMMA interface, the propagation length of the SPPs is significantly shorter in the absorption band of the R6G.

In the experiment shown in Figure C.17(A), we measure an intensity I of out-scattered plasmons (with the Alq3 spectrum)

$$I = \eta P_{rad} I_o, \tag{C.17}$$

where I_o is some initial energy of surface plasmons, η is the optical collection efficiency, and P_{rad} is the probability of a plasmon being scattered relative to all other damping mechanisms. It is expressed in terms of propagation lengths as

$$P_{rad} = \frac{1/L_{rad}}{1/L_{tot}} = \frac{1/L_{rad}}{1/L_{rad} + 1/L_{ohmic}}. \tag{C.18}$$

In the experiment shown in Figure C.17(B), acceptors are present on the opposite side and we measure an intensity (with the Alq3 spectra) $I' = \eta P'_{rad} I_o$, with

$$P'_{rad} = \frac{1/L_{rad}}{1/L_{tot'}} = \frac{1/L_{rad}}{1/L_{rad} + 1/L_{ohmic+R6G}}. \tag{C.19}$$

To qualitatively explain our experimental observations, the key quantity of interest here is the relative observed intensity of scattered donor-emitted SPPs. This is

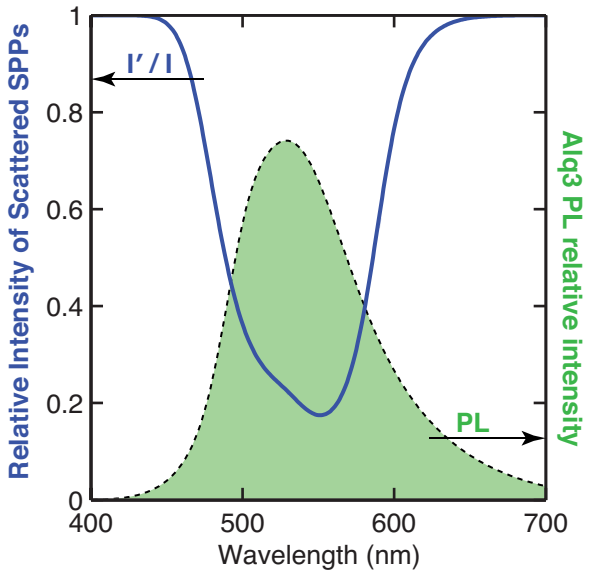

Fig. C.19. The observed intensity of scattered donor Alq3 emitted SPPs is reduced by 70-80% when acceptors are present on the opposite side of the 100 nm Ag film.

calculated as $I'/I = P'_{rad}/P_{rad}$. Notice that since the collection efficiency and initial plasmon intensity remains constant between the two experiments, then only the ratio of scattering probability dictates the observed relative intensities. Using our calculations from Figure C.18, we estimate that the observed intensity of scattered donor Alq3 emitted SPPs is reduced by 70-80% when acceptors are present on the opposite side of the 100 nm Ag layer. This agrees well with experiment where we observe a significant quenching of Alq3 emission (see figure 4.3 in chapter 4.)

D. FABRICATION AND CHARACTERIZATION OF SELF-ASSEMBLED, DISORDERED GOLD NANOPARTICLE FILMS

D.1 Donor vs Acceptor Fluorescence Emission in FRET

When FRET occurs, the donor fluorescent emitters in a donor-acceptor mix experience an additional decay channel from FRET and the donor fluorescence decay is more rapid. This is shown in the donor emission kinetics in figure D.1. In the main text, we utilize this property to distinctively identify and quantity FRET on the gold NP substrates.

Another distinct identifier of FRET is the emission kinetics of the acceptor fluorescent emitters. If the normal decay of the acceptors is much more rapid than the donors, then during FRET the acceptor fluorescence decay will be slowed and begin to approach the donor decay. This is due to the fact that the FRET process yielding excitation of the acceptors is now the rate limiting factor in the acceptor fluorescence decay (see section D.6 below). This unique feature is shown in the acceptor emission kinetics in figure D.1. This observation provides further proof of FRET on top of our gold NP films.

D.2 Analytic Model of Dye concentrations in doped PMMA films

D.2.1 Introduction

Fluorescent dyes embedded within PMMA are often spin-cast as thin-films on top of resonant or plasmonic nanostructures. In experiments involving many-body interactions between dyes and nanostructures, the local number concentration of the dyes strongly affects the strength of interactions observed. It is therefore paramount

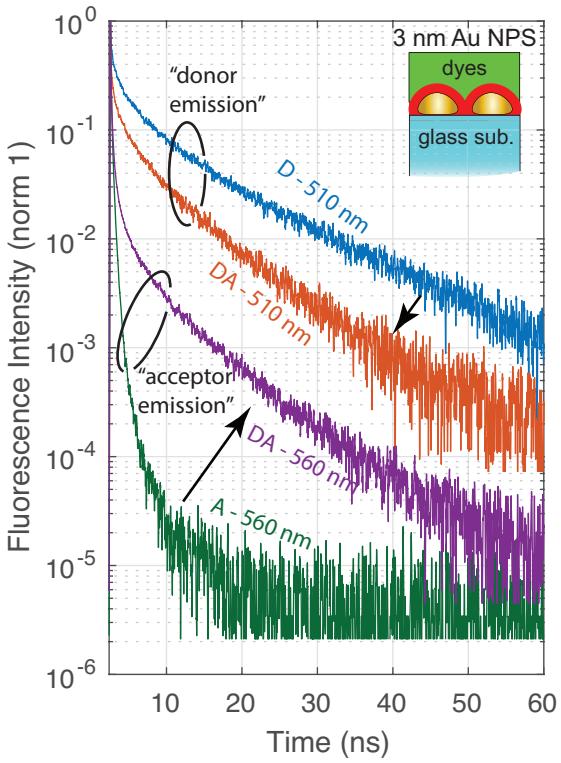

Fig. D.1. We measure the donor and acceptor emission kinetics separately using bandpass filters centered at 510 nm (donor emission) and 560 nm (acceptor emission). Shown is the corresponding decay traces for donor alone (D), acceptor alone (A), and donors mixed with acceptors (DA) above our gold NP films. We observe the well known quenching of the donor emission kinetics due to FRET in the mixed samples (D→DA at 510 nm, blue, red). In addition, we notice the acceptor emission is significantly less rapid in the presence of FRET (A→DA at 560 nm, green, purple). This is a distinct signature of FRET.

to accurately estimate the fluorescent dye density in the vicinity of nanostructures in order to accurately model experimental observations. In this short section, we work from first principles using simple relations to estimate the dye density in dye-doped spin-cast PMMA films. We find that under normal conditions the dyes occupy only about 1-2% of the total film volume and we can regard the film as a PMMA *matrix* doped with dye particles. Typical dye concentrations within the film are estimated to be on the order of $1 - 5 \times 10^{19}$ particles/cm^3.

D.2.2 General Theory

We start out with two separate solutions, namely, (1) a dye solvent mixture and (2) a PMMA solvent mixture.

1. The initial concentration of the of the dye solvent mixture is $c_{do} = m_d/V_s$, where m_d is the mass of dye dissolved in the volume V_s of solvent.
2. The initial concentration of the PMMA solvent mixture is calculated from its concentration by mass in the solvent which is provided by the manufacturer. Typically, the PMMA solution will be named PMMA 495 A2, where 495 refers to molecular mass 495,000 g/mol and A2 refers to the PMMA concentration by mass in the solvent anisole, in this case 2%. Since the PMMA is dissolved in the anisole, the mass density in the solvent can be calcuated as $c_{po} = x\rho_{\text{anisole}}/(1-x)$, where x is the percent by mass of the PMMA in the solvent anisole, and ρ_{anisole} is the bulk mass density of anisole.

As an example, we now mix (1) the dye solutions with (2) the PMMA solution and, pure anisole (also called ZEP A) in the proportions 1:2:2 [1]. It then follows directly that in this new solution, the dye concentration and PMMA concentrations are

$$c_d = c_{do} \times 1/5 \tag{D.1}$$

$$c_p = c_{po} \times 2/5. \tag{D.2}$$

[1]This ratio of 1:2:2 chloroform:PMMA 495 A2: anisole has been shown to consistently yield 20 nm films if spin-cast at 8000 RPM with a 3 s ramp time.

This solution is now spin-cast into a film; the solvents evaporate (or are boiled/baked off by a post-spin annealing process), leaving the dye in a solid PMMA film. We now make a big assumption:

The mass ratios of the dye particles to PMMA molecules is the same in the final spin-cast film (no solvents), as it is in solution (with solvents).

This is stated mathematically as

$$\left[\frac{m_d}{m_p}\right]_{\text{film}} = \left[\frac{m_d}{m_p}\right]_{\text{sol}} = \frac{c_d}{c_p} \equiv \eta, \tag{D.3}$$

where we have defined the unitless mass ratio $\eta \equiv c_d/c_p$, specified by the initial dye and PMMA concentrations within the spinning solution. Now suppose we have a film of volume V. We must have

$$V = m_p/\rho_p + m_d/\rho_d, \tag{D.4}$$

where m_p and m_d are the total mass of PMMA molecules and dye particles in the film, and ρ_p and ρ_d is the bulk mass density of the PMMA and dyes respectively. Using this relation we find that mass densities of each species within the film to be

$$m_d/V = \frac{\eta\rho_d\rho_p}{\rho_d + \eta\rho_p}, \tag{D.5}$$

$$m_p/V = \frac{\rho_d\rho_p}{\rho_d + \eta\rho_p}. \tag{D.6}$$

This can be easily converted into number of particles per volume using the Stoicheometric relation $m/N = M/N_a$ where m is a given mass, N is the number of particles, M is the molar mass and N_a is Avogadro's number. This leads to the following expression for the number density of dye particles n_d and PMMA molecules n_p:

$$n_d = \frac{N_a}{M_d}\frac{\eta\rho_d\rho_p}{\rho_d + \eta\rho_p} \tag{D.7}$$

$$n_p = \frac{N_a}{M_p}\frac{\rho_d\rho_p}{\rho_d + \eta\rho_p}. \tag{D.8}$$

Another key quantity is the volume filling fraction both the PMMA molecules and dye particles respectively. In the final film, the volume of PMMA is $V_p = m_p/\rho_p$ and

the volume of dyes is $V_d = m_d/\rho_d$. We are interested in the relative volumes occupied by each species, namely $\tilde{V}_p = V_p/V$ and $\tilde{V}_d = V_d/V$. Using $V = V_d + V_p$ along with our definitions of V_p, V_d and η, we find the volume filling fraction of each species to be

$$\tilde{V}_d = \frac{\eta\rho_p}{\rho_d + \eta\rho_p} \tag{D.9}$$

$$\tilde{V}_p = \frac{\rho_d}{\rho_d + \eta\rho_p}. \tag{D.10}$$

Example: Calculate Molecules / mL

Suppose we dissolve 20 mg of Alq3 dyes in 30 mL of chlofororm. We then have $c_{do} = 0.67$ mg/mL. We then mix this dye solution with the PMMA 495 A2 and anisole in the proportions 1:2:2. The dye concentration in the final solution has the dye concentration diluted as $c_d = 1/5 \times c_{do} = 0.13$ mg/mL.

The initial PMMA 495 concentration in the PMMA A2 495 mixture is calculated from its mass concentration by percent x as $c_{po} = x\rho_{\text{anisole}}/(1-x)$. For PMMA A2 495, we have $x = 0.02$. The density of anisole is $\rho_{\text{anisole}} = 0.995$ g/mL. Combining this data we find $c_{po} = 20$ mg/mL. As above, the dye solution is mixed with this PMMA solution and anisole in the proportions 1:2:2, so that the PMMA is diluted by a factor 2/5 leading to a final PMMA concentration of $c_p = 8.1$ mg/mL.

We then calculate the unitless mass filling factor to be $\eta = c_d/c_p = 0.016$. Using η, $M_p = 495,000$ g/mol, $M_d = 459$ g/mol, Avogadro's number $N_a = 6.02 \times 10^{23}$, $\rho_p \approx 1.2$ g/mL, $\rho_d \approx 1.3$ g/mL, and equations D.7 and D.8 above, we find

$$n_p \approx 1.4 \times 10^{18} \text{ PMMA molecules/mL} \tag{D.11}$$

$$n_d \approx 2.5 \times 10^{19} \text{ Alq3 molecules/mL}. \tag{D.12}$$

The relative volumes occupied by each species is calculated using equations D.9 and D.10:

$$\tilde{V}_d \approx 1.5\% \tag{D.13}$$

$$\tilde{V}_p \approx 98.5\%. \tag{D.14}$$

We see that the majority of the film is composed of PMMA molecules and we can indeed regard the film as a PMMA *matrix* doped with Alq3 particles.

D.2.3 Future Work: Dye-Dopant Confinement in Thin-Films

Above, we have made the assumption that the ratio of the mass concentrations of PMMA to dye dopants is the same in solution as it is in the film:

$$[c_d/c_p]_{\text{film}} \equiv [c_d/c_p]_{\text{solution}} .$$

This may be a good assumption for bulk films where the film thickness Z is much larger than the average separation distance between dopant dyes, $Z \gg 1/\left(n_d\right)^{1/3}$. In this case the concentration profile of the dopant dyes can still be regarded as a 3D-distribution. However, if the film thickness is smaller than the average separation distance,

$$Z \leq 1/\left(n_d\right)^{1/3} , \tag{D.15}$$

then confinement effects and the exact microscopic behavior of the massive PMMA molecule chains will play a major role in the actual concentration profile and furthermore, for $Z \ll 1/\left(n_d\right)^{1/3}$, the bulk dopant concentration n_d will become a 2D surface concentration σ_d.

At present, I do not have an exact theory to model the transition of the bulk 3D dopant concentration to the 2D surface dopant concentration, that is the true concentration density function $f(Z, n_d)$ where $\sigma_d = \lim_{Z\to 0} f(Z, n_d)$ and $n_d = \lim_{Z\to\infty} f(Z, n_d)$. This function can be extracted empirically from experiment using ellipsometry and spectral absorption measurements. The basic procedure is as follows: (1) accurately measure the absorbance resonance strength of dye-doped PMMA films of different thickness using a spectrophotometer; (2) accurately determine the film thickness Z by performing spectroscopic ellipsometry of the dye:PMMA film and modeling the data at spectral frequencies away from any of the dopant absorption resonances, typically in the $\lambda \approx 700 - 1200$ nm range. (3) apply the Beer-Lambert law [168, 169]

along with the assumption that the absorption cross section of the dopant-dye is on the order of 1-3 nm^2. This will yield an estimate of the average dopant-dye concentration within the film that is accurate to a factor of $\times 1 - 3$ since within the Beer-Lambert law, the absorption cross section enters linearly. This accuracy may be high enough to determine if the dye-dopant ultra-thin film (2D) concentration is significantly deviating from the bulk (3D) dye-dopant concentration.

D.3 Fabrication of Disordered Gold NP Films

The process flow for the fabrication of self-assembled gold nanoparticle films on glass is summarized in figure D.2 and the text descriptions therein.

D.4 Optical Characterization of Disordered Gold NP Films

Figure D.3(a) shows a macroscopic image of the pre- and post-annealed films. The unannealed gold film appears a dark-grey indicating no sharp spectral response. Upon annealing the gold nanoparticle film acquires a distinct red color indicating the presense of a LSP resonance. We utilize an ultrathin dielectric coating to tune the LSP spectral response of the annealed gold nanoparticle films as described below. Figure D.3(b) shows a simple summary of this fabrication procedure.

Figure D.3(c) shows the normal incidence extinction spectrum ($-\log_{10} T$ where T is the specular transmittance) for the unannealed and annealed 3 nm Au films. As expected, we note that the annealed Au film displays a well defined extinction peak whereas the unannealed island-like film displays a broad spectral extinction with no marked resonance. These observations provide evidence of the presence of a well defined plasmonic resonance in the annealed film while in the unnanealed film the complex island morphology results in the islands resonating in a broad spectral range [124, 140].

Another key observation shown in figure D.3(c) is the marked effect that the substrate cleaning method has on the plasmonic resonances. The initial island for-

1. Cleaning Substrates

(a) Clean the substrates via piranha etch for 10-15 minutes.
(b) Thoroughly wash substrates with water and blow dry with pure nitrogen.

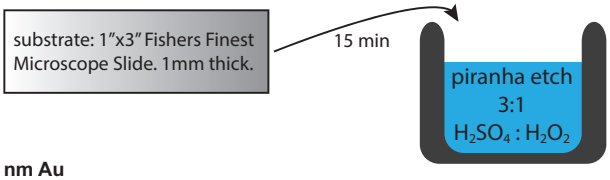

2. Sputter 3 nm Au

Au film will be discontinuous. The quartz crystal monitor (deposition rate monitor) reads a mass M. The deposition rate monitor assumes the film is continuous and then estimates the deposited thickness as t = M/(Aρ), where t is the thickness, A is the area of the crystal and ρ is the density of the deposited material. Sputtering at 60 W and 15 mTorr, 3 nm takes about 21 s.

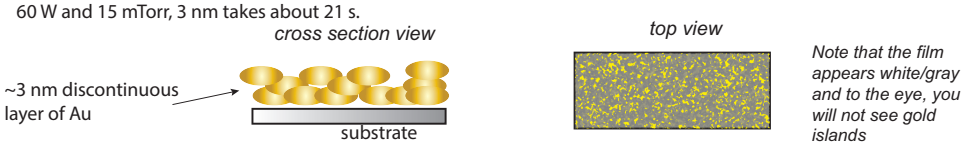

3. Anneal sample in N_2

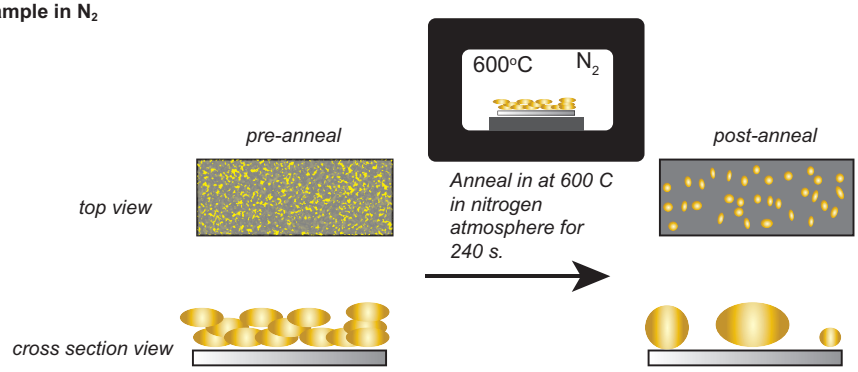

4. Conformal ALD Al_2O_3 Coating

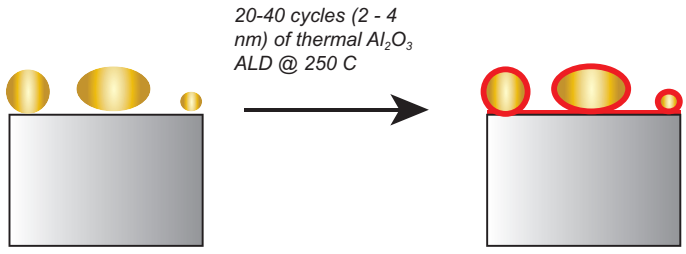

Fig. D.2. The process flow for the fabrication of self-assembled gold nanoparticle films is shown.

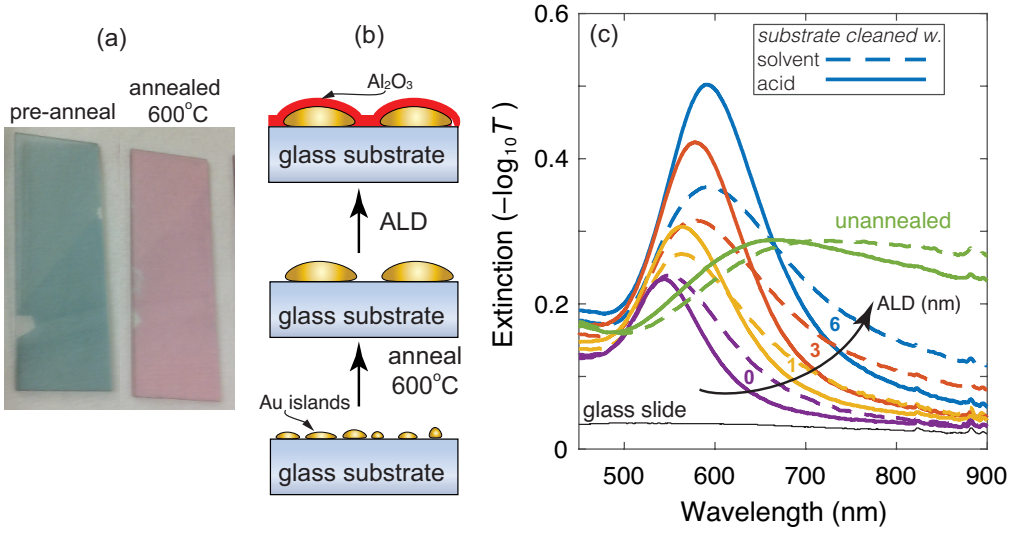

Fig. D.3. (a) A macroscopic image of a pre- and post-annealed 3 nm gold film on glass is shown. The samples are illuminated via standard fluorescent room lights. (b) A simple schematic of the fabrication procedure is shown. The post-annealed self-assembled gold nanoparticle films are coated with Al_2O_3 via atomic layer deposition (ALD).(c) The localized surface plasmon resonance spectral location red-shifts and the quality factor increases upon coating with the high index Al_2O_3 dielectric. Prior to gold deposition, cleaning with acid as opposed to organic solvents results in higher quality plasmonic resonances. The unannealed 3 nm Au film supports no well defined resonances regardless of the initial substrate cleaning method.

mation of thin metal films will of course be very sensitive to the deep nanoscale surface chemistry between Au and the glass substrate. We observe that cleaning the substrate prior to gold deposition with piranha etch (3:1 sulphuric acid: hydrogen peroxide) as opposed to organic solvents (toluene, acetone, methanol) always results in higher quality factor plasmonic resonances in the self assembled gold nanoparticle films. This potentially stems from two non-mutually exclusive causes: (1) The piranha etch simply leaves a cleaner surface and there is less wide spread organic debris on the surface preventing gold growth. (2) The piranha solution etches the glass substrate surface, reducing nanoscopic roughness and yielding more efficient gold island and nanoparticle formation. These causes have not been explored fully and will be studied in future work.

To confirm that we are indeed observing a LSP resonance and not a chemical change of the glass substrate or gold particles, we must be able to predict the spectral response of the ensemble of gold NPs. We model the extinction spectra of the annealed gold nanoparticle film with Mie scattering theory [140, 144]. Figure D.4 shows the relatively good agreement of the Mie scattering theory with experimental observations, confirming that we are observing a LSP resonance. We assume the gold NPs are spherical and that they do not mutually interact (couple); the dielectric permittivity of gold used in the model was extracted via ellipsometry on a 18 nm thick continuous Au film and agreed well with refs. [117, 170]. In the modeling, the experimentally extracted ensemble of gold nanoparticle sizes and densities (figure D.4 inset) must be included to accurately predict the spectral location, width and strength of the LSP extinction resonance. We model the effect of the 4 nm ALD Al_2O_3 layer as though the gold NPs are embedded in a bulk space of Al_2O_3. The dielectric permitivitty of Al_2O_3 was taken from NanoHub [118].

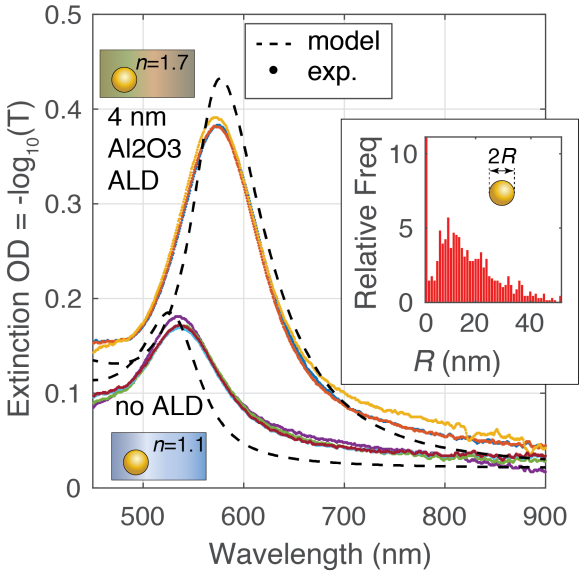

Fig. D.4. Mie scattering theory is used to model the the observed optical response of the gold nanoparticle films. The model can easily account for the addition of dielectric spacer layers deposited on the gold NPs. To accurately predict experimental observations the ensemble of NP sizes must be included in the model (see inset).

D.5 Ellipsometry of Disordered Gold NP Ensembles

We use spectroscopic ellipsometry to verify that the surface morphology of the nanoparticle film does not result in major changes to the dye:PMMA film thickness relative to the same spincast recipe on blank glass. In this process, the optical response of the gold-nanoparticle layer is treated as an effective Lorentz oscillator. We find that the Lorentz oscillator model accurately predicts the optical response of the gold NP films. To accurately determine each layer thickness, a specific order of ellipsometric analysis of control samples must be followed to limit the total number of free fitting parameters. Figure D.5 describes the details of the spectroscopic ellipsometry analysis while figure D.6 shows the key results from the model.

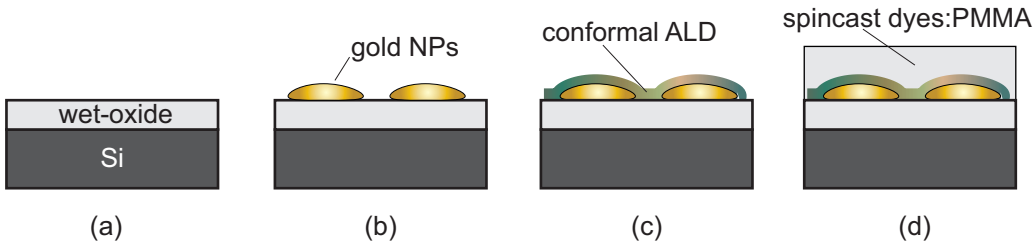

Fig. D.5. *Ordering of spectroscopic ellipsometry for gold nanoparticle films.* Note, for spectroscopic analysis, the gold films were deposited on the wet-oxide of a silicon wafer and not a glass slide. (a) The thickness of wet-oxide on the silicon wafer is extracted first. (b) The gold nano particle film is treated as an effective homogeneous medium of finite thicknes. The effective dielectric function of the gold naoparticle film is modeled using a Lorentz oscilator to account for the plasmon resonance. (c) The affects of the conformal ALD coating is modeled in two ways. First, the spectral location of the Lorentz oscillator from (b) must be allowed to red-shift due to the red-shifting plasmon resonance. Second, the ALD film must be added directly into the film stack. (d) The affects of the top PMMA film are modeled similar to that of the ALD film. First, the Lorentz oscillator resonance of the effective gold NP dielectric function must be allowed to red-shift. Secondly, the PMMA film is added directly into the film stack. If the PMMA is doped with fluorescent particles, then the film stack should be modeled away from the fluorescent particles absorption resonances to avoid adding another Lorentz oscillator to the model. It is critical to note, that going from (a)-(d), the model parameters such as thicknesses and dielectric functions from the previous step remain fixed, except where noted above.

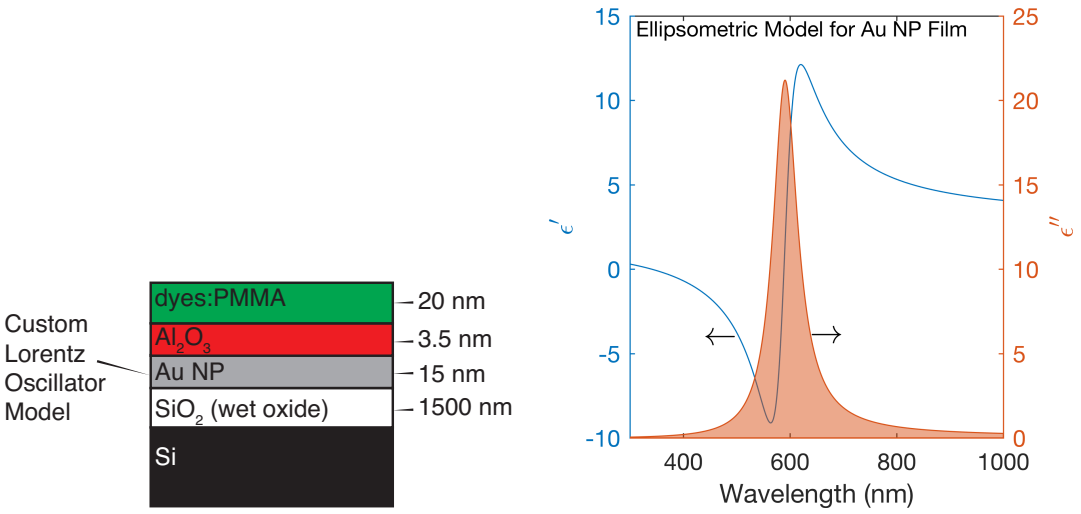

(a) (b)

Fig. D.6. (a) A schematic is shown of the final spectroscopic model used to determine the top PMMA thickness. (b) Shown is the effective permittivity of the gold NP film is modeled with a Lortentz Extracted effective dielectric permittivity.

D.6 Monte-Carlo FDTD Methods for Solving Emission Kinetics of many-body FRET

The time dynamics of FRET within an random distribution of N donors and M acceptors is governed by a set of $M + N$ coupled non-linear differential equations (assuming that donor:donor interactions are negligible, i.e. super- and sub-radiance is ignored). The excited state population of each donor is coupled to the ground state population of each and every acceptor, while the ground state population of each acceptor is coupled to the excited state population of each and every donor. The set of differential rate equations and the procedure to solve these equations described here is general and can thus be extended to predict time dynamics of FRET in arbitrarily complex environments. This section lays out the physical origin of the coupled differential equations and describes an FDTD method for solving these coupled differential equations. A Monte Carlo method is used to model realistic experimental, ensemble conditions.

D.6.1 One fluorescent emitter species near a nanophotonic structure

We start this discussion with equations that govern the expected emission kinetics of a single fluorescent emitter species in a non-homogeneous environment (i.e. nanophotonic structure). In vacuum or bulk (infinite dimension) dielectric, each donor is assumed to be identical and can be characterized by an intrinsic quantum yield η and an excited state relaxation rate of γ_o. When these emitters are placed near a photonic environment, the Local Density of Optical States (LDOS) changes and thus the radiative part of the excited state relaxation rate is reduced or enhanced depending on whether the LDOS has decreased or increased [104, 112]. Each and every emitter will have a slightly different position and dipole orientation relative to the photonic structure and each emitter will therefore have a slightly different LDOS.

The probability that the i^{th} donor is in the excited state at a given time t is denoted by $n_i(t)$ and is described by the linear differential equation

$$\frac{\mathrm{d}n_i}{\mathrm{d}t} = -\left[(1-\eta)\gamma_o + \eta\beta^i\gamma_o\right] n_i, \tag{D.16}$$

where β^i is the enhancement or reduction factor of the excited state relaxation rate of the i^{th} donor [19, 104, 112]. The non-radiative relaxation rate $(1-\eta)\gamma_o$ is assumed to be unaffected by the local environment. If we assume that at time $t = 0$ all the emitters are in the excited state ($n_i(t=0) = 1$) then each emitter spontaneously relaxes via single exponential decay

$$n_i(t) = \mathrm{e}^{-\gamma^i t} \tag{D.17}$$

with the exponential decay constant

$$\gamma^i = \left[(1-\eta) + \eta\beta^i\right] \times \gamma_o. \tag{D.18}$$

An observable quantity is spontaneously emitted photons (or confined modes that scatter to freespace), therefore we expect to observe a spontaneous emission intensity that is an ensemble of all the N emitters:

$$I(t) \sim \sum_{i=1}^{N} C_i \times \frac{\eta\beta^i\gamma_o}{\gamma^i} \times n_i(t) = \sum_{i=1}^{N} C_i \times \frac{\eta\beta^i\gamma_o}{\gamma^i} \times \mathrm{e}^{-\gamma^i t}. \tag{D.19}$$

C_i is the probability of detection of a photon emitted from the i^{th} emitter. This empirical term has been introduced to account for the fact that not all spontaneously emitted photons have an equal chance of observation. This is due to the fact that some emitters preferentially emit into rigorously dark modes (i.e. plasmons, waveguide modes, lossy surface waves). In the ideal case, these dark modes are not observable using conventional far-field microscopy techniques; however, due to scattering from surface roughness or other such local defects, some of these dark modes are scattered and collected by the microscope/ detector. Methods for estimating C_i for planar metallic structures are outlined in appendix C.5.6. This is the main focus of Chapter 3 in this thesis.

Critically, equation D.19 shows fundamentally that due to the ensemble of locations of emitters relative to the inhomogeneous photonic structure, a non-trivial multi-exponential photoluminescence decay will be observed. For $t >> 0$, $I(t) \sim \mathrm{e}^{-\gamma_{min}t}$, where $\gamma_{min} = \min[\gamma^i]$; that is, for long times, the emitters with slowest relaxation rate γ^i will be observable as a decaying single exponential. These observations are supported by the *donor only* decay traces observed the experiments of chapters 4 and 5.

D.6.2 FRET near a nanophotonic structure

We now explore the emission kinetics of two emitter species near a nanophotonic structure in the context of Förster Resonance Energy Transfer (FRET): that is, the emission kinetics of donors and acceptors. A very different emission physics relative to a single emitter species is observed due to the spatially dependent coupling of donors to acceptors. Even in a homogeneous environment where the donors alone (or acceptors alone) normally emit more or less the same single exponential decay, a donor with acceptor ensemble fundamentally yields a multi-exponential decay [130]. The emission kinetics can also be strongly affected by acceptor concentration. This section outlines a general method for calculating and quantifying FRET using emission kinetics of donor-acceptor ensembles near arbitrarily complex nanophotonic structures.

One potential ensemble with two donors and two acceptors is shown in Figure D.7. Using a QED/Green function method, the FRET rate between the i^{th} donor and the j^{th} acceptor can be estimated aa $\Gamma_{ET}^{i,j}$. However, for a donor to transfer it's dipole excitation energy to an acceptor, the donor must be in the excited state and the acceptor must be in the ground state. This critical requirement leads to the coupled relaxation rate equations

$$\frac{\mathrm{d}n_i}{\mathrm{d}t} = -\gamma_d^i n_i - n_i \sum_{j=1}^{M} \Gamma_{ET}^{i,j} p_j \tag{D.20}$$

$$\frac{\mathrm{d}p_j}{\mathrm{d}t} = +\gamma_a^j (1 - p_j) - p_j \sum_{i=1}^{N} \Gamma_{ET}^{i,j} n_i \tag{D.21}$$

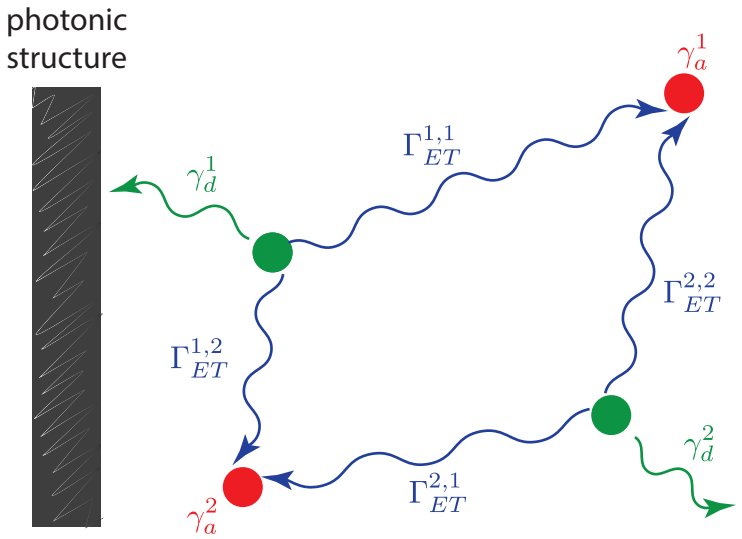

Fig. D.7. Key constants and physics for an example coupled FRET system with 2 donors and 2 acceptors.

Here p_j is the probability that the j^{th} acceptor is in the ground state, and γ_q^k is the spontaneous emission rate of the k^{th} emitter of species q (see equation D.18). The excited state of donor i is *depleted* by spontaneous emission and FRET while the ground state of the acceptor j is depleted via FRET and *replenished* via spontaneous emission of its excited state.

These $M+N$ coupled non-linear differential equations governing the excited and ground state populations can not be solved analytically (to the best of our knowledge) but must be solved numerically; here we employ an FDTD method. To model experimental conditions of many donors and acceptors distributed randomly within a dielectric medium, we employ the following procedure:

- a Monte-Carlo method is used to generate random positions of M acceptors and N donors $\boldsymbol{r}_q^{\,k} = [x_k, y_k, z_k]$
- Using a QED/Green function method the FRET rates are calculated for each of the $M+N$ possible donor:acceptor pairs $\Gamma_{ET}^{i,j} = \Gamma_{ET}(\boldsymbol{r}_d^{\,i}, \boldsymbol{r}_a^{\,j}, \omega_d)$. At this point, the spontaneous emission rate of each emitter is also calculated.
- An numerical (FDTD) method is then used to compute the time evolution of n_i and p_j using the initial conditions of $n_i(t=0) = 1$ and $p_j(t=0) = 0$.
- The observed photoluminesnce decay of the N donor molecules is $I(t) \approx \sum_{i=1}^{N} \frac{\mathrm{d}n_i(t)}{\mathrm{d}t}$

It should be emphasized that the Monte-Carlo numerical method of solving the coupled rate equations for ensemble FRET can be applied to arbitrarily complex photonic environments, as long as the electromagnetic Green Tensor $\boldsymbol{G}(\boldsymbol{r}, \boldsymbol{r\prime}, \omega)$ can be calculated. The method described here can also capture concentration effects.

D.7 Laser Ablation and Melting of gold NPs

In the FRET experiments on gold NPs, it is critical that the laser pump for the fluorescent donor-acceptor dyes is at a low enough fluence so as not to melt or rearrange the NPs. We pump the dyes with 400 nm, 30-50 fs laser pulses from an OPA. Gold has interband transitions at this wavelength and thus strong absorption

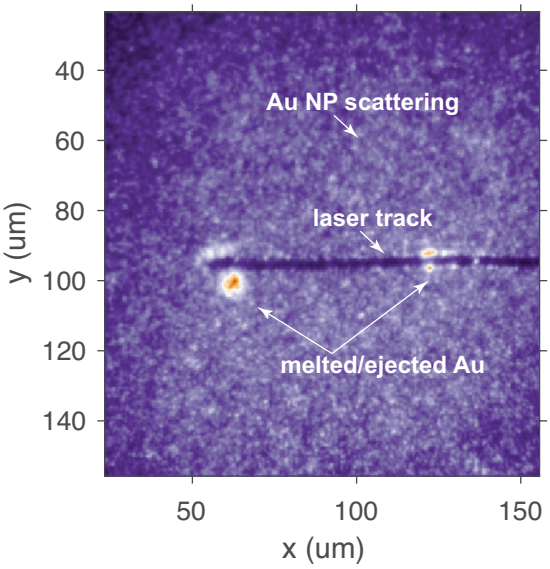

Fig. D.8. Dark-field scattering microscopy reveals laser induced melting and ablation of the gold NP substrate.

and heat when pumped with 400 nm light. In FRET experiments we typically pump the gold NP / dyes sample with about 60 pJ pulses at 100 KHz repetition rate.

Figure D.8 shows a white-light, dark-field scattering image of the gold NP substrate. Before this image was taken, we translated the sample while pumping it in the confocal geometry with 5-10 nJ pulses at 100 KHz, $\lambda = 400$ nm. We observe castrophic laser induced ablation and melting of the gold NP films. Time resolved studies reveal that under continuous 100 KHz 400 nm laser pumping, this melting occurs on sub-100 ms time scales.

D.8 Dark-Field and Fluorescence Microscope Calibration

We calibrate our fluorescence and dark-field microscopes with a commercial calibration slide. We image the scattering from the metal calibration tick marks on a glass slide via dark-field white light scattering microscopy as shown in our optical setup shown in figure 5.3 of chapter 5. In such an dark-field, scattering image, the contrast of the tick marks is reversed as described schematically in figure D.9.

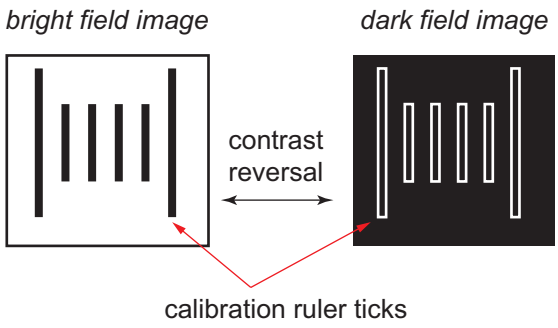

Fig. D.9. The contrast of dark-field images is reversed relative to bright field image

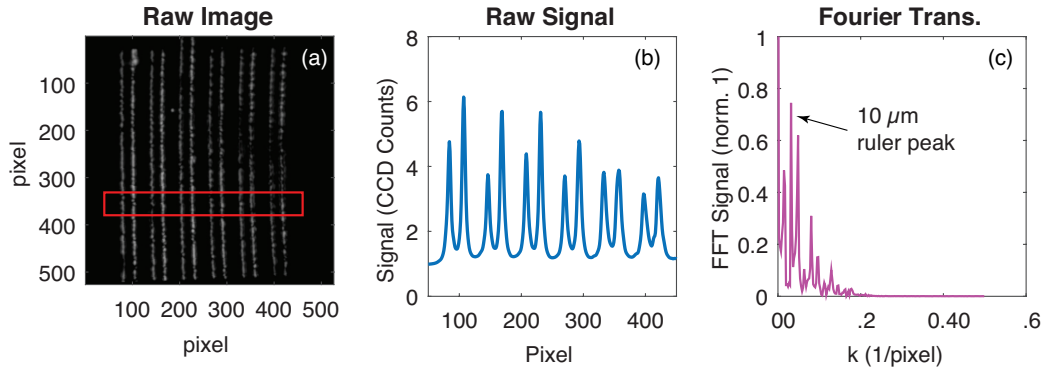

Fig. D.10. (a) Raw dark-field image of calibration ruler. (b) CCD counts are binned/ summed in the vertical direction to get a 1D signal versus the horizontal direction. (c) The FFT of this 1D signal reveals the spatial frequency of the ruler tick marks.

Figure D.10(a) shows the dark-field image of the calibration ruler, imaged with 50x microscope objective. We sum the counts in the vertical direction to obtain a clean 1D signal as plotted in figure D.10(b). We utilize fast Fourier transforms (FFT) to extract the spatial period of the tick marks. This spatial period multiplied by the 10 μm period of the ruler, yields the calibration constant for the objective, namely, the number of micrometers per pixel on the CCD. It is assumed that the microscope is more or less symmetric and this calibration holds for the vertical direction as well.

To test this calibration constant we perform a simple test. We shift the 1D calibrated signal by exactly 10 μm and observe that the shifted signal overlaps almost perfectly with the previous signal (figure D.11).

The above calibration technique worked well for the 10x, 20x and 50x objectives but worked poorly for the 100x objective, which contained too few calibration ruler tick marks for an accurate FFT. In this case, the calibration ruler scattering peaks in the 1D signal were directly fit with gaussian shapes, and their center locations were used to extract the calibration constant (as shown D.12).

Table D.1 summarizes the calibration results while figure D.13 shows the calibrated images of the calibration ruler tick marks for each microscope objective magnification.

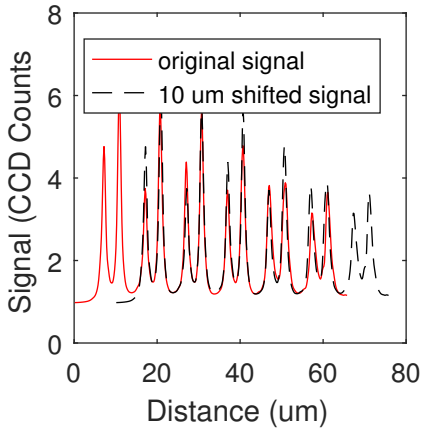

Fig. D.11. Simple calibration test.

Table D.1.
Microscope calibration constants are summarized.

Objective	10x	20x	50x	100x
Field of View (μm)	321	155	64	31
μm/pixel	0.8	0.39	0.16	0.077
Method	FFT	FFT	FFT	Peaks

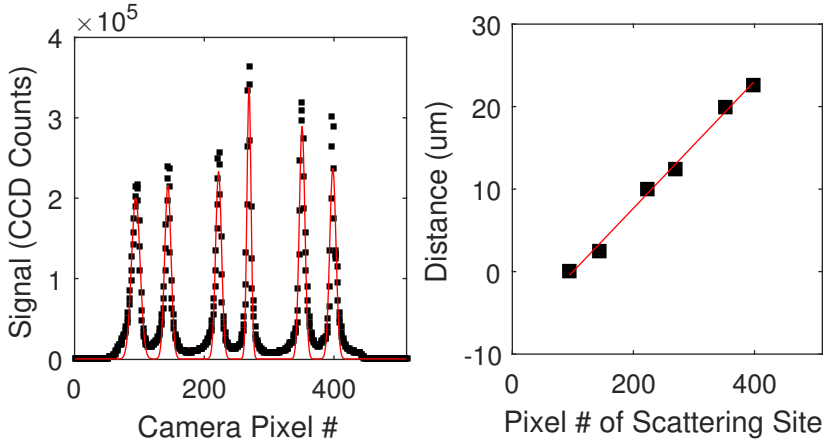

(a) Raw Signal with fitted peaks (b) Peak locations

Fig. D.12. Calibration of 100x objective.

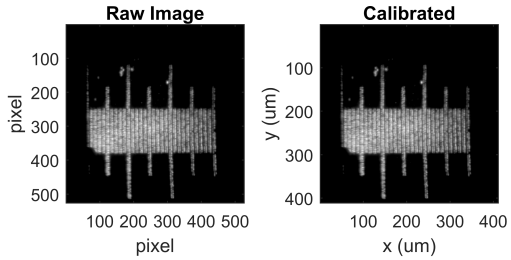

(a) 10x

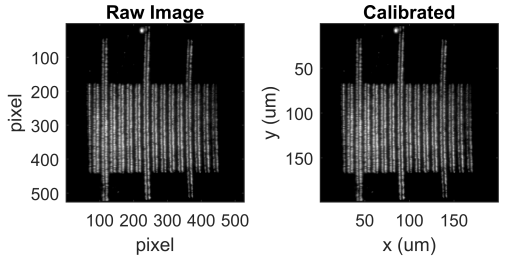

(b) 20x

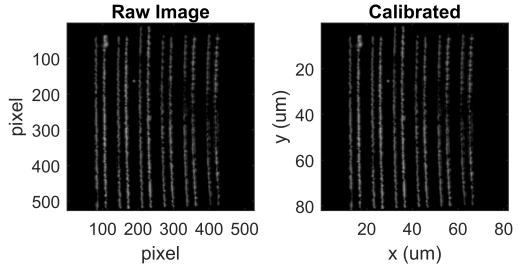

(c) 50x

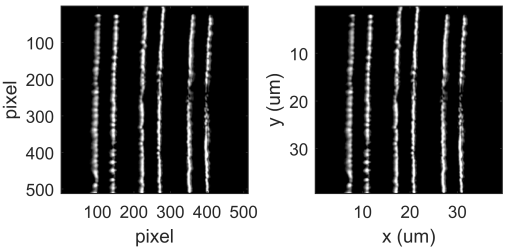

(d) 100x

Fig. D.13. Using a commerical calibration slide, the magnification, field of view, and abberations of the microscope can be calibrated. (a-c) The 10x, 20x and 50x objectives were calibrated with a Fast-Fourier-Transform method, while (d) the 100x objective was calbirated with a peak-finding and fitting procedure as described in within the main body.

E. KEY LIGHT-SOURCE SPECIFICATIONS

E.0.1 Pulsed White Light

The pulsed white light is spectrum is shown in figure E.1. We generate this light source via supercontinuum generation in a undoped YAG crystal [171]. The time duration of the pulsed white light has not been measured as of yet.

E.0.2 Narrowband Pulsed Light: Optical Parametric amplifiers

The tuning curves for our two separate OPAs are shown in figure E.2. Power measurements were made with a photodiode-based power meter. Spectral measurements

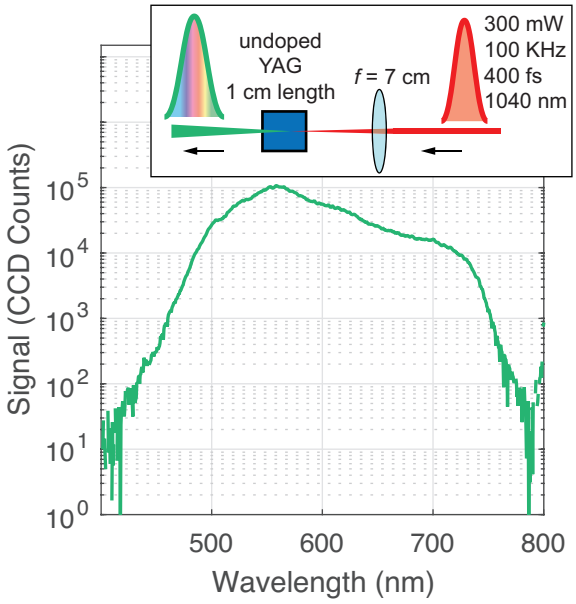

Fig. E.1. The spectrum for the pulsed white light supercontinuum is shown. Residual 1040 nm laser pump from the back port of the optical parametric amplifier is used to pump an undoped YAG crystal.

were made with a hand-held spectrometer. The pulse duration was measured via an autocorrelator.

The OPAs are pumped with a 400 fs, 23.5 μJ, 1040 nm laser pulses. Part of this signal is split to generate white light in a YAG crystal, seeding the OPA, while the remainder of the 1040 nm light is sent to a second (2H) or third (3H) harmonic generating crstal (BBO, or two BBOs). The second and third harmonic pump the actual parametric mixing process with the white light.

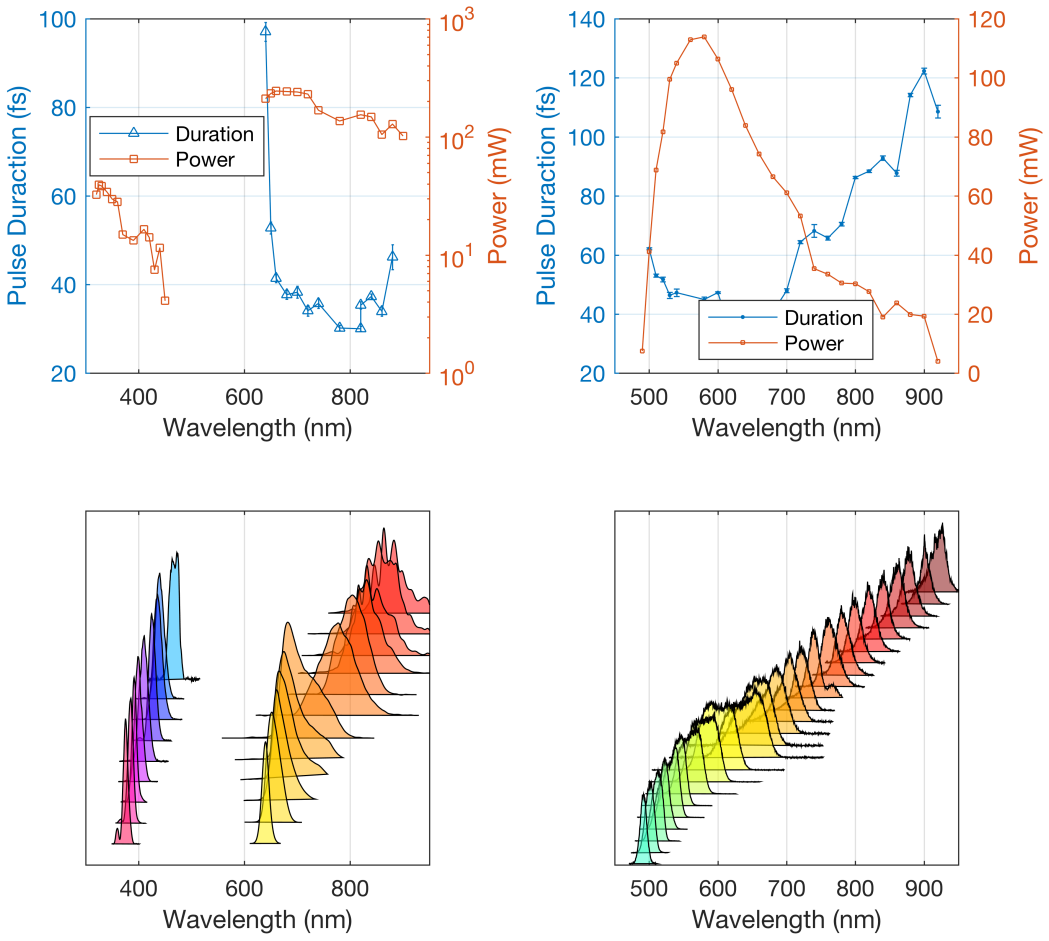

(a) NOPA 2H

(b) NOPA 3H

Fig. E.2. The tuning curves for the optical parametric amplifiers is shown. The NOPA 2H is pumped by the second harmonic of a pulsed 1040 nm laser and the NOPA 3H is pumped by the third harmonic of a pulsed 1040 nm laser. Both OPAs are seeded by a white light supercontinuum generated via pumping an undoped YAG crystal.

VITA

VITA

Ward Newman graduated with a Bachelors of Applied Science in Engineering Physics, Nanoengineering from the University of Alberta in 2011. Mr. Newman then entered the PhD program at the University of Alberta, Dept. of Electrical and Computer Engineering, and studied Experimental Quantum Nanophotonics there with his supervisor Prof. Zubin Jacob until Prof. Jacob's acceptance of a professorship at Purdue University in late 2015. Mr. Newman then transferred to Purdue University to complete his PhD in the College of Electrical and Computer Engineering, starting January 2016. Mr. Newman is presently a PhD candidate at Purdue University studying experimental Quantum Nanophotonics in the Birck Nanotechnology Center.

Mr. Newman was the recipient of the Alexander Graham Bell PhD scholarship from the Canadian National Science and Engineering Research Council in 2012, and the SPIE John Kiel Scholarship in 2014; in 2015, he was named as *One to watch in photonics* by the magazine Photonics Spectra. Mr. Newman plans to join the Intel Portland Technology Development Group following his graduation in the Fall of 2017.